

Spring 2004

# Beam spin asymmetry measurements in deeply virtual Compton scattering

Gagik Gavalian

*University of New Hampshire, Durham*

Follow this and additional works at: <https://scholars.unh.edu/dissertation>

---

## Recommended Citation

Gavalian, Gagik, "Beam spin asymmetry measurements in deeply virtual Compton scattering" (2004). *Doctoral Dissertations*. 205.  
<https://scholars.unh.edu/dissertation/205>

This Dissertation is brought to you for free and open access by the Student Scholarship at University of New Hampshire Scholars' Repository. It has been accepted for inclusion in Doctoral Dissertations by an authorized administrator of University of New Hampshire Scholars' Repository. For more information, please contact [nicole.hentz@unh.edu](mailto:nicole.hentz@unh.edu).

BEAM SPIN ASYMMETRY MEASUREMENTS IN DEEPLY VIRTUAL  
COMPTON SCATTERING

BY

Gagik Gavalian

B.S., Yerevan State University, 1995

M.S., Yerevan State University, 1996

DISSERTATION

Submitted to the University of New Hampshire  
in partial fulfillment of  
the requirements for the degree of

Doctor of Philosophy

in

Physics

May 2004

UMI Number: 3132786

### INFORMATION TO USERS

The quality of this reproduction is dependent upon the quality of the copy submitted. Broken or indistinct print, colored or poor quality illustrations and photographs, print bleed-through, substandard margins, and improper alignment can adversely affect reproduction.

In the unlikely event that the author did not send a complete manuscript and there are missing pages, these will be noted. Also, if unauthorized copyright material had to be removed, a note will indicate the deletion.

**UMI**<sup>®</sup>

---

UMI Microform 3132786

Copyright 2004 by ProQuest Information and Learning Company.

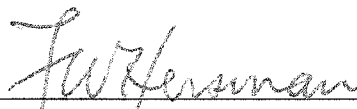
All rights reserved. This microform edition is protected against unauthorized copying under Title 17, United States Code.

ProQuest Information and Learning Company  
300 North Zeeb Road  
P.O. Box 1346  
Ann Arbor, MI 48106-1346

This dissertation has been examined and approved.



Director, M. Holtrop  
Assistant Professor



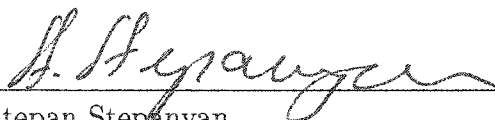
F.W. Hersman  
Professor of Physics



Silas Beane  
Assistant Professor



Karsten Pohl  
Assistant Professor



Stepan Stepanyan  
Staff Scientist (JLAB)

January 30, 2004  
Date

# Dedication

This work is dedicated to my father Dr. Valeri Gavalian and to my family.

# Acknowledgments

I thank my advisors in University of New Hampshire Prof. Bill Hersman and Prof. Maurik Holtrop for constant leadership, encouragement and support throughout my graduate school years. I want to express my gratitude to my colleague and co-advisor Stepan Stepanyan for providing invaluable help and guidance throughout my thesis work and any project I worked on. I want thank also my advisor Kim Egiyan for helping me through my graduate research at YerPhI and JLAB, and also the entire Lab. 126 personal - Samvel, Gegham, Youri, Raphael, for providing help and good working environment at YarPhI. I also would like to thank Harout Avakian, Latifa Elouadrihiri, Inna Aznaurian and Hovanes Egiyan for helpful discussions which greatly facilitated my work. Thanks the entire Hall-B personal, whose dedicated efforts in building, maintaining and running such a sophisticated detector as CLAS, made this work possible.

Thanks to the entire Armenian community of Newport News for support and help during my staying in Virginia. And also I would like to thank my friends - Hovanes, Hovik, Aram, Hrayir, Joe, Nerses, Lei, Rakhsha, Ulrike - for all the help and support.

# Table of Contents

Dedication . . . . .	iii
Acknowledgments . . . . .	iv
Abstract . . . . .	xxii
<b>1 PHYSICS MOTIVATION</b>	<b>1</b>
1.1 Introduction . . . . .	1
1.2 Deep Inelastic Scattering . . . . .	2
1.3 Generalized Parton Distributions . . . . .	5
1.3.1 Notations . . . . .	7
1.4 GPD Formalism . . . . .	8
1.4.1 Phenomenology of the GPDs . . . . .	8
1.4.2 Spatial Image of the Nucleon . . . . .	12
1.4.3 Parametrization of the GPDs . . . . .	14
1.4.4 Twist-3 GPDs . . . . .	18
1.5 Deeply Virtual Compton Scattering . . . . .	20
1.5.1 Previous Measurements . . . . .	25
<b>2 EXPERIMENTAL SETUP</b>	<b>30</b>

TABLE OF CONTENTS

vi

2.1	Accelerator . . . . .	30
2.2	CLAS Detector . . . . .	31
2.2.1	Drift Chambers . . . . .	33
2.2.2	Čerenkov Counters . . . . .	35
2.2.3	Scintillation Counters . . . . .	37
2.2.4	Forward Electromagnetic Calorimeter . . . . .	38
2.3	Liquid Hydrogen Target . . . . .	41
2.4	Trigger System and Data Acquisition . . . . .	42
<b>3</b>	<b>DATA CALIBRATION AND PROCESSING</b>	<b>45</b>
3.1	Data Processing . . . . .	45
3.2	TOF Calibration . . . . .	48
3.2.1	Pedestal and TDC calibration . . . . .	48
3.2.2	Time Walk Correction . . . . .	50
3.2.3	Left-Right PMT Alignment . . . . .	50
3.2.4	Energy Calibration . . . . .	51
3.2.5	RF and Paddle-to-Paddle calibration . . . . .	53
3.2.6	Crude Tuning . . . . .	56
3.2.7	Alignment of TOF system to the RF-signal . . . . .	58
3.2.8	Calibration Results . . . . .	59
3.3	Drift Chamber Calibration . . . . .	60
3.3.1	Drift Chamber Nomenclature . . . . .	62
3.3.2	Function Parametrization . . . . .	64
3.4	Electromagnetic Calorimeter Time Calibration . . . . .	66

TABLE OF CONTENTS

vii

3.5	Čerenkov Detector Calibration . . . . .	68
3.5.1	Cosmic Ray calibrations . . . . .	69
3.5.2	Electron Beam Calibration . . . . .	70
4	DATA ANALYSIS . . . . .	72
4.1	The E1D Run Period . . . . .	72
4.1.1	Data Reconstruction . . . . .	72
4.2	Particle Identification . . . . .	77
4.2.1	Electron ID . . . . .	77
4.2.2	Proton ID . . . . .	82
4.2.3	Photon ID . . . . .	86
4.3	Particle Momentum Corrections . . . . .	88
4.3.1	Electron momentum corrections . . . . .	88
4.3.2	Proton momentum corrections . . . . .	90
4.3.3	Second method of corrections . . . . .	91
4.3.4	Selection of Final States . . . . .	94
4.3.5	Fit procedure . . . . .	94
4.3.6	Check of Corrections . . . . .	96
5	DVCS ANALYSIS . . . . .	98
5.1	Kinematics . . . . .	98
5.2	Missing Mass Technique . . . . .	99
5.2.1	Fit to the $M_x^2$ distributions . . . . .	102
6	SYSTEMATIC STUDIES OF THE ANALYSIS METHOD . . . . .	105
6.1	Studies With Experimental Data . . . . .	105

6.2	Tests With GSIM . . . . .	109
6.3	Studies of asymmetries with missing mass cuts . . . . .	114
6.4	Conclusions . . . . .	117
7	RESULTS AND CONCLUSIONS . . . . .	119
7.1	Results . . . . .	119
7.2	Estimate of Systematic Error . . . . .	123
7.3	SUMMARY . . . . .	125
8	APPENDIX . . . . .	128
8.1	MOMENTUM CORRECTIONS . . . . .	128
8.1.1	Electron Momentum Correction Constants . . . . .	128
8.1.2	Proton Momentum Correction Constants . . . . .	129
8.1.3	$\pi^+$ momentum calculation for $ep \rightarrow e\pi^+n$ final state . . . . .	131
8.1.4	Momentum Correction Constants for II Method . . . . .	133
8.2	FIT RESULTS . . . . .	134
8.2.1	Extracted number of photons . . . . .	134
8.2.2	Fit Figures . . . . .	136
8.2.3	Obtained asymmetries . . . . .	143

# List of Tables

1.1	Fourier coefficients $c_i^I$ and $s_i^I$ of the interference term. . . . .	25
1.2	Parameters sets for models of H- and E- type GPDs. . . . .	26
4.1	The eld run summary. . . . .	73
6.1	Results of the fit to the mixed distributions with constant mixing ratio. . .	110
6.2	Results of the fit to the mixed distributions with constant number of $\pi^0$ s. .	110
7.1	Summary of obtained Beam Spin Asymmetries. Here $\alpha$ and $\beta$ are the first and second moment of the asymmetry amplitude fitted with function $A_{LU} =$ $\alpha \sin(\phi) + \beta \sin(2\phi)$ . . . . .	122
7.2	Summary of obtained Beam Spin Asymmetries. Here $\alpha$ and $\beta$ are the first and second moment of the asymmetry amplitude fitted with function $A_{LU} =$ $\alpha \sin(\phi) + \beta \sin(2\phi)$ . . . . .	123
8.1	The momentum correction parameters derived using the second method of corrections described in the text. There are 16 parameters per sector (96 in total). . . . .	133

# List of Figures

1-1	a) handbag diagram for the forward Compton amplitude $\gamma^*p \rightarrow \gamma^*p$ , whose imaginary part gives the DIS cross section. b) Handbag diagram for DVCS in the region $\xi < x < 1$ . . . . .	6
1-2	Model calculation of GPD $H(x, \xi, t)$ as a function of $x$ and $\xi$ at $t = 0$ . . . . .	10
1-3	The $u$ -quark phase-space charge distribution at different values of the Feynman momentum for non-factorizable ansatz of generalized parton distributions. The vertical and horizontal axis correspond to $z$ and $ \vec{r}_\perp $ , respectively, measured in femtometers. The [dashed] contours separate regions of positive [darker areas] and negative [lighter areas] densities. Below each contour plot the shape of three-dimensional isodensity contours are presented. . . . .	12
1-4	Handbag diagrams for DVCS and Bethe-Heitler processes. . . . .	20

1-5	The kinematics of leptonproduction in the rest frame of the target. The $z$ -direction is chosen counter-along the three momentum of the incoming virtual photon. The lepton three-momenta form the lepton scattering plane, while the recoil proton and outgoing real photon define the hadron scattering plane. In this reference system the azimuthal angle of the scattered lepton is $\phi_l = 0$ , while the azimuthal angle between the lepton plane and the recoiled proton momentum is $\phi_N = \phi$ . When the hadron is transversely polarized (in the reference frame) $S \perp = (0, \cos\Phi, \sin\Phi, 0)$ , the angle between the polarization vector and the scattered hadron is denoted as $\phi = \Phi - \phi_N$ . . . . .	21
1-6	The beam-spin asymmetry as function of azimuthal angle measured at HERMES a) in reaction $e^+p \rightarrow e^+p\gamma$ with initial beam energy $27.6\text{GeV}$ kinematical. (b) BSA from CLAS in $ep \rightarrow ep\gamma$ at $E = 4.25\text{GeV}$ . . . . .	28
2-1	CEBAF Accelerator. In the right upper corner blowup shows cross section of five recirculating arcs in the tunnel. In the right lower corner the cross section of a cryomodule. In the upper left corner the linac cryomodules cross section is shown. . . . .	31
2-2	Three dimensional view of CLAS detector. . . . .	32
2-3	CLAS toroidal magnet. . . . .	33
2-4	Layout of super-layers in Region 3. The sense wires are located in the center of each cell, while the field wires are located in the vertices of the hexagons. The shadowed hexagons represent the cells containing the sense wires which produced a signal for a representative track. . . . .	34
2-5	Arrangement of the CC optical modules of one sector. . . . .	36

2-6	One optical module of CLAS Čerenkov counter, showing the detector components and the hypothetical light paths from electrons. Čerenkov light from electrons reflected twice from the mirrors into the Winston Cone (WC), surrounded by the magnetic shield (MS). The Winston cones are used to collect the light onto the surface of the Photo-multipliers (PMT). . . . .	37
2-7	TOF system for one sector. The length, the width and the readout configurations are different for different paddles. . . . .	38
2-8	CLAS Forward Electromagnetic Calorimeter exploded view of one of the sectors. . . . .	39
2-9	Electromagnetic Calorimeter readout scheme. PMT - photomultiplier, LG - Light Guide, FOBIN - Fiber Optic Bundle Inner, FOBOU - Fiber Optic Bundle Outer, SC - Scintillators, Pb - 2.2 mm Lead Sheets, IP - Inner Plane (Composed of two 1.905 mm Stainless Steel Face Sheets and 72.2 mm Foam Core Plate) . . . . .	40
2-10	Engineering drawings (CAD) of CLAS cryogenic target cell on (the left) and GSIM image of the target used in simulations. . . . .	41

- 2-11 CLAS Data Acquisition System schematic view. The signals from the detector go to the ROCs and pretriggers. The pretriggers initiate the readout from the particular detector system as well as provide an input for the Level-1 trigger. In case of present trigger the data signals are read out, digitized and transferred to a process called Event Builder (EB) running on the main computer clon10 and are temporarily stored in the Data Distribution (DD) ring in shared memory. A process called the Event Recorder (ER) writes data from the DD ring onto disks from where they are transferred to the tape silo. Some of the events from the DD ring on clon10 are transferred to a different computer clon00 to be used as an input stream for monitoring programs. . . . . 44
- 3-1 An example of an event reconstructed by RECSIS. The in-bending track on the top half of the detector corresponds to an electron that triggered the event, the out-bending track in the lower half corresponds to a positively charged particle. . . . . 46
- 3-2 Typical distribution of TDC time (channels) versus pulse height (ADC channels). The fitted function  $f_w$  (parametrization of  $f_w$  is given by Eq.(3.6)) used in time-walk corrections Eq.(3.5). . . . . 49
- 3-3 Energy deposited in the TOF scintillators by hadrons versus hadron momentum after MIP calibration is done. Pion and proton bands are clearly distinguishable. . . . . 52

3-4	Illustration of the beam RF-structure: a) $\Delta\tau$ distribution with properly calibrated TDCs, b) $\Delta\tau$ distribution when the $c_1$ parameter of the TDC of the RF-signal is mis-calibrated by less than 1%, c) R-distribution (described in Eq.(3.15)) for a single scintillator channel, fit to a Gaussian. . . . .	54
3-5	Two dimensional plot of $R$ versus $t_{rf}$ distribution for a) uncalibrated RF-signal and b) calibrated RF-signal. . . . .	55
3-6	Distribution of number of events versus $\delta t_{vtx}$ defined in Eq.(3.16) for two different counters. On a) the maximum number of events is detected with $\delta t_{vtx} = 2.0039$ ns time shift. b) the maximum number of events is detected with $\delta t_{vtx} = 0.0$ ns. . . . .	57
3-7	The TOF Calibration Results. a) the velocity of positively charged particles versus momentum is plotted. The kaon band is artificially enhanced by pre-selecting events from data sample with a loose kaon cut. b) Mass spectrum of hadrons calculated from TOF for an empty target run at $E_0 = 4$ GeV is plotted. Clearly visible peaks correspond to pions, kaons, protons, deuterons and tritons respectively. . . . .	60
3-8	Mass squared distribution for backward flying particles with momentum $P < 0.25$ GeV: a) without any sector cut, b) electron and the other particle are required to be in the same sector. . . . .	61
3-9	Schematic View of CLAS Drift Chambers. This view represents a slice through the drift chambers at target position. The schematic shows how regions and super-layers are placed and named. . . . .	63

3-10	Scatter plot of DOCA versus the corrected drift time for a) R3 axial wires showing the track local-angle dependence, and b) R2 axial wires showing the magnetic-field dependence where the local angle ranges between $23^\circ$ and $25^\circ$ . The overlaid curves represent the fitted time-to-distance function. . . . .	65
3-11	The time resolution of the CLAS Electromagnetic Calorimeter. $\Delta t$ defined in Eq.(3.28) is plotted for one sector after EC calibrations. . . . .	67
3-12	Calibration of Single photo-electron amplitude. . . . .	69
3-13	Example of PMT with large noise function fitted with Gaussian function and a background of form $f(x) = a \cdot e^{-bx}$ . . . . .	70
3-14	Mean value of T0 as function of PMT number. The time is corrected for track length. . . . .	71
4-1	Calibration stability a) RF timing calibration for eld run period. The fitted mean value and sigma are plotted. b) DC resolution for 6 super-layers. . . .	73
4-2	Reconstructed particles per run file, a) electrons per trigger, b) reconstructed protons (red dots, $\sim 0.4$ per trigger) and photons (blue dots, $\sim 0.85$ per trigger) . . . . .	74
4-3	Beam charge asymmetry calculated according to Eq.(4.1) versus run number (a), and the beam charge asymmetry distribution for entire run period (b). . . . .	75
4-4	The electron hit coordinates are plotted for U,V and W planes from left to right. The cuts were used to eliminate evens too close to the edge of Calorimeter ( $U > 15$ , $V < 370$ and $W < 405$ ). . . . .	77

4-5	(a) EC fiducial cuts. The effect of the applied cuts is shown. The dark area corresponds to all electrons reconstructed by RECSIS, and the lighter area electrons that passed the cut.(b) The number of Photo-Electrons in the CC detector versus energy deposited in the EC. A cut was applied to the number of Photo-Electrons ( $n_{phe} > 25$ ) to eliminate pions. . . . .	78
4-6	The EC deposited energy normalized to momentum versus momentum of the particle, (a) for all electron candidates, (b) after CC+EC cuts. (c) the $EC_{tot}/P$ distribution showing effects of the cuts. . . . .	79
4-7	Electromagnetic shower distribution in the EC for electron candidates. (a) the deposited energy in the inner versus outer part of EC before cuts and (b) after applied cuts on CC+EC. . . . .	80
4-8	$Q^2$ and $W$ distributions before and after cuts, a) $Q^2$ for electron candidates with id=11, b) $Q^2$ for electron candidates with id=0, c) $W$ spectra for electron candidates with id=11. . . . .	81
4-9	Proton identification with measured $\beta$ of positive particles (a) $\beta$ versus momentum of positively charged particle, the red band is RECSIS identified protons. (b) the mass distribution of positively charged particles (light area) and RECSIS identified protons (dark area). . . . .	82
4-10	The $\Delta t$ distribution calculated as shown in Eq.(4.2) (a) $\Delta t$ versus momentum of positive particle, the red lines show the cut used for proton selection. (b) the $\Delta t$ distribution, the shaded area represents proton cut. . . . .	83
4-11	a) $dE/dx$ for all positive particles, b) $dE/dx$ for positive particles after cutting on $\Delta t$ . . . . .	84

4-12 Proton selection, SEB identified protons compared with protons identified using $\Delta t$ cut. The “gray” area is the mass of all positively charged particles, the darker area is the protons identified by RECSIS using cut on momentum versus $\beta$ distribution, and the lighter area are protons selected using cut on $\Delta t$ . . . . .	85
4-13 The $ep$ missing mass square distribution for $ep \rightarrow ep\gamma\gamma$ is plotted versus $2\gamma$ invariant mass. On the right the negative particles beta is plotted ( <i>dashed line</i> ) and neutral particles that pass invariant mass cut ( <i>solid line</i> ) . . . . .	86
4-14 The neutral particle EC deposited energy (a) before invariant mass cuts and (b) after cuts. . . . .	87
4-15 Radiative elastic events selection. a) $epX$ missing momentum transverse component, b) $ep$ scattering plane ( $ \phi_e - \phi_p $ ) angle before ( <i>dashed line</i> ) and after <i>solid line</i> the cuts. . . . .	89
4-16 $ep \rightarrow e\pi^+n$ reaction selection, (a) the missing mass of detected $e'\pi^+$ , (b) $\pi^+$ kinematical coverage. . . . .	91
4-17 Fit to the calculated over reconstructed $\pi^+$ momentum for different $\theta_{\pi^+}$ bins (one sector). . . . .	92
4-18 Pion event selection. (a) invariant mass of $2\gamma$ in reaction $ep \rightarrow e'p\gamma\gamma$ versus $e'p$ missing mass, (b) $e'p$ missing mass square distribution after cut on invariant mass ( $0.08 < M_x^2 < 0.17$ ) . . . . .	93
4-19 Event selection for MINUIT momentum corrections, a) the cut for radiative elastic events, b) cut for the pion events . . . . .	94

4-20	Radiative elastic events. $ep$ missing mass $\phi_e$ dependence for all sectors. Red squares are uncorrected, blue diamonds are corrected using method I and green triangles are corrected using method II. . . . .	95
4-21	The mean and sigma of the radiative elastic peak as a function of electron sector in CLAS. The mean (a) and sigma (b) for each sector are plotted before corrections, and after corrections with two different methods described in this chapter. . . . .	96
4-22	The mean and sigma of the $\pi^0$ peak as a function of electron sector in CLAS. $\pi^0$ events are selected from $ep \rightarrow ep\gamma\gamma$ events with cut on $2\gamma$ invariant mass around pion mass. The mean (a) and sigma (b) for each sector are plotted before corrections, and after corrections with two different methods described in this chapter. . . . .	97
5-1	The kinematical coverage of the eld data set. (a) the $Q^2$ versus $x_B$ distribution is shown with $Q^2$ bin divisions. (b) $Q^2$ versus $t$ distribution is shown, the boxes indicate the kinematical bins used for these analysis. . . . .	99
5-2	$ep$ missing mass for $ep \rightarrow epX$ for low $W$ region (a) and for high $W$ region (b).100	
5-3	Extraction of $G_\gamma$ (on the left) and $G_{\pi^0}$ (on the right) Gaussian function parameters are done by fitting corresponding final states with Gaussian plus polynomial function. . . . .	101
5-4	Example of fits for one $\phi_{qp}$ bin. a) the background fitted to the distribution end points, b) fit to positive helicity events to extract number of $\gamma$ and $\pi^0$ under missing mass peak, c) fit to negative helicity. . . . .	102

5-5	(a) number of reconstructed events in each $\phi_{qp}$ bin for positive and negative helicity. (b) asymmetry for $\langle Q^2 \rangle = 1.2944 \text{ GeV}^2$ , $\langle x_B \rangle = 0.176578$ and $\langle -t \rangle = 0.240303 \text{ GeV}$ with Eq.(5.4), obtained $A_{LU} = 0.188 \pm 0.036$ . . . . .	103
6-1	(a) fit to the end points of missing mass distribution for background extraction (b) Fit to missing mass with two Gaussian functions plus background to extract number of $\gamma$ 's and $\pi^0$ under missing mass peak. . . . .	106
6-2	Fits to identified $ep\gamma$ (a) and $ep\pi^0$ (b) final states to determine the mean and sigmas for $G_\gamma$ and $G_{\pi^0}$ . . . . .	107
6-3	Ratios of reconstructed to thrown events for single photon and pion events, a) for constant $N_\gamma/N_{\pi^0}$ ratio, b) for constant number of events in the mixed distribution. . . . .	108
6-4	Simulated data kinematics compared with data. . . . .	111
6-5	Missing mass squared distribution for negative (left) and positive (right) helicities fitted with two Gaussian plus background for on $\phi_{qp}, Q^2$ bin. The black points represent mixed distribution and the fit to it. . . . .	112
6-6	Reconstruction of single photon and single pion final states with double Gaussian fit. (a) the ratio of the reconstructed number of single photon events to the number of thrown events for positive ( <i>red circle</i> ) and negative ( <i>blue cross</i> ) helicities, and the ratio of negative to positive reconstruction efficiencies. (b) same ratios for number of reconstructed pions. . . . .	112
6-7	Extracted beam spin asymmetries for DVCS and $\pi^0$ compared with asymmetry obtained by using missing mass fitting method. The obtained asymmetry is shifted from thrown for $\sim 3\%$ . . . . .	113

6-8	Diagram explaining cuts used on missing mass to calculate the asymmetry. The arrows show the cut on missing mass. The missing mass distribution is drawn, the <i>solid line</i> corresponds to the photon and <i>dashed line</i> to pion. . . . .	114
6-9	Asymmetry extracted using missing mass cut with fixed low limit. The points are placed at the high limit cut. . . . .	115
6-10	Asymmetry extracted using missing mass cut with fixed bin size in missing mass squared. The points are placed in the middle of the bin. . . . .	116
7-1	Fit to the number of photon final states in each $\phi_{qp}$ bin for bin centering. The two halves of azimuthal distributions are fitted separately. . . . .	120
7-2	Asymmetry as a function of azimuthal angle fitted with Eq.(7.4) to extract $\sin\phi$ moment for three $Q^2$ bins. . . . .	121
7-3	Asymmetry as a function of azimuthal angle fitted with Eq.(7.4) to extract $\sin\phi$ moment for three $t$ bins for integrated $Q^2$ ( $1.4 < Q^2 < 2.5$ ( $GeV^2$ )). . . . .	122
7-4	The $Q^2$ (on the left) and $t$ (on the right) dependence of DVCS asymmetries. The “cross” symbol is the asymmetry measured by CLAS with 4.2 $GeV$ data. . . . .	123
7-5	The mean and sigma value distribution for photon and pion peaks for one kinematical bin. . . . .	124
7-6	Systematic error estimation. The fits to the missing mass squared distributions were performed for using mean and sigma values for photon and pion peaks varied within the error of their determination. . . . .	125
8-1	The fits to $M_x^2$ for $1.0 < Q^2 < 1.4$ (negative helicity). . . . .	137
8-2	The fits to $M_x^2$ for $1.0 < Q^2 < 1.4$ (positive helicity). . . . .	138
8-3	The fits to $M_x^2$ for $1.4 < Q^2 < 1.9$ (negative helicity). . . . .	139

8-4	The fits to $M_x^2$ for $1.0 < Q^2 < 1.4$ (positive helicity). . . . .	140
8-5	The fits to $M_x^2$ for $1.9 < Q^2 < 2.8$ (negative helicity). . . . .	141
8-6	The fits to $M_x^2$ for $1.9 < Q^2 < 2.8$ (positive helicity). . . . .	142
8-7	Fit to the azimuthal asymmetry for $1.0 < Q^2 < 1.35 \text{ GeV}^2$ for integrated $0.1 < t < 0.4 \text{ GeV}$ . . . . .	143
8-8	Fit to the azimuthal asymmetry for $1.35 < Q^2 < 1.7 \text{ GeV}^2$ for integrated $0.1 < t < 0.4 \text{ GeV}$ . . . . .	144
8-9	Fit to the azimuthal asymmetry for $1.7 < Q^2 < 2.8 \text{ GeV}^2$ for integrated $0.1 < t < 0.4 \text{ GeV}$ . . . . .	144
8-10	Fit to the azimuthal asymmetry for $0.1 < -t < 0.25 \text{ GeV}$ for integrated $1.4 < Q^2 < 2.5 \text{ GeV}^2$ . . . . .	145
8-11	Fit to the azimuthal asymmetry for $0.25 < -t < 0.35 \text{ GeV}$ for integrated $1.4 < Q^2 < 2.5 \text{ GeV}^2$ . . . . .	145
8-12	Fit to the azimuthal asymmetry for $0.35 < -t < 0.6 \text{ GeV}$ for integrated $1.4 < Q^2 < 2.5 \text{ GeV}^2$ . . . . .	146

# ABSTRACT

## BEAM SPIN ASYMMETRY MEASUREMENTS IN DEEPLY VIRTUAL COMPTON SCATTERING

by

Gagik Gavalian  
University of New Hampshire, May, 2004

Beam Spin Asymmetry (BSA) is studied in the Deeply Virtual Compton Scattering (DVCS) using CLAS detector at Jefferson Lab and longitudinally polarized electron beam with 4.8 GeV energy. This asymmetry is directly proportional to the imaginary part of the scattering amplitude, which relates it to the Generalized Parton distribution functions. Reaction  $ep \rightarrow epX$  is studied. A fit to the line shape of the missing mass squared distribution of  $(ep)$  is used to extract the number of single photon final states in each kinematical bin for both helicities of the beam and for the helicity sum. DVCS beam spin asymmetry is measured in several bins of  $Q^2$  and  $t$ . The  $Q^2$  and the  $t$ -dependences of the  $\sin\phi$  moment of the asymmetry is extracted for the first time.

# CHAPTER 1

## PHYSICS MOTIVATION

### 1.1 Introduction

One of the fundamental topics of modern high energy physics is the understanding of the nucleon structure. Studies with leptonic beams in the deep inelastic scattering region (DIS) have led to the discovery of the quark-gluon structure of the nucleon. It was found that quarks carry about half of the nucleon momentum, and about 25% of the nucleon spin.

Recent developments in the theory have opened new perspectives for studying nucleon structure. Such studies can be made in hard exclusive leptonproduction experiments. A formalism developed by Ji [1], Radushkin [2] and Muller [3] for the QCD description of hard exclusive processes introduces Generalized Parton Distributions, GPDs (or Skewed Parton Distributions), that contain information on the correlations between quarks and on transverse and angular momentum distributions.

A large program for studying GPDs is proposed for the CLAS detector at Jefferson Laboratory in Newport News (VA). Although more favorable kinematical conditions for these studies will be reached at high energies, there are measurements that can be done at

lower energies.

One of the key experiments for studying GPDs is Deeply Virtual Compton Scattering (DVCS). The Bjorken scaling regime in DVCS can be reached at  $Q^2 \sim 3(\text{GeV}/c)^2$ , and even at lower  $Q^2$  ( $\sim 1(\text{GeV}/c)^2$ ) the corrections to the leading order diagram are manageable.

This opens up an opportunity for studying DVCS at JLAB with already available electron beams. At these energies DVCS can be studied through Beam Spin Asymmetry (BSA) measurements.

In this work the Beam Spin Asymmetries are measured in the reaction  $\vec{e}p \rightarrow ep\gamma$ , with 4.8 GeV longitudinally polarized electrons in the  $Q^2$  range (1.0 – 2.5 GeV<sup>2</sup>), and  $t$  (0.1 – 0.6 GeV).

## 1.2 Deep Inelastic Scattering

In 1911, Rutherford used  $\alpha$  particles to resolve the structure of gold atoms by measuring the angles of the scattered particles. The cross section formula that Rutherford did empirically establish in the non-relativistic case was:

$$\frac{d\sigma}{d\Omega} = \frac{\alpha^2}{4(p\beta)^2 \sin^4(\theta/2)} \quad (1.1)$$

where  $\alpha$  is a fine structure constant,  $\beta$  is the velocity of the projectile,  $p$  is the momentum of the projectile and  $\theta$  is the scattering angle in the laboratory frame (where target is fixed). The Eq.(1.1) is written for the  $ep$  scattering, where both the target and the projectile have charge equal 1. The low energetic  $\alpha$  particles can be assumed to be point-like compared to gold atoms. To study the structure of the nucleon one has to use point-like particles as projectiles, such as leptons. When using projectiles with spin-1/2, the Rutherford formula

for scattering has to be corrected, which was done by Mott [4] in 1932:

$$\left(\frac{d\sigma}{d\Omega}\right)_{Mott} = \left(\frac{d\sigma}{d\Omega}\right) \cdot \frac{\cos^2(\theta/2)}{1 + \frac{2E}{M}\sin^2(\theta/2)} \quad (1.2)$$

where  $\cos^2(\theta/2)$  and  $(1 + \frac{2E}{M}\sin^2(\theta/2))^{-1}$  arise from the spin-1/2 of the electron and the target, respectively.  $M$  is the target mass and  $E$  is the initial energy of the electron. By the uncertainty principle, the larger  $q^2$  is the better the resolution with which the target is being probe. In 1950, Rosenbluth [5] proposed to involve the proton electric and magnetic form factors characterizing the deviations from a point-like behavior of the proton. Assuming the proton to have spin 1/2, the Rosenbluth expression for elastic  $ep$  scattering gave:

$$\left(\frac{d\sigma}{d\Omega}\right)_{ep \rightarrow ep} = \left(\frac{d\sigma}{d\Omega}\right)_{Mott} \left(\frac{G_E^2 + \tau G_M^2}{1 + \tau} \cos^2(\theta/2) + 2\tau G_M^2 \sin^2(\theta/2)\right) \quad (1.3)$$

where  $\tau = -q^2/4M^2$ , and  $G_E$  and  $G_M$  are the electric and magnetic form factors of the proton, respectively. In the experimental measurements of proton form factors it was found that they drop sharply with increasing momentum transfer. That was the first evidence for a distributed structure of the proton within the sphere with an estimated radius of  $(0.85 \pm 0.1) fm$  [6]. As a basis for inelastic  $ep$  scattering cross section calculation, the result for electron-muon scattering was taken [7]. Then the following result for inelastic  $ep$  scattering cross section was obtained taking into account the unknown structure of the proton parametrized in terms of two structure functions  $W_1$  and  $W_2$  [8]:

$$\left(\frac{d\sigma}{dE'd\Omega}\right)_{ep \rightarrow ep} = \frac{\alpha^2}{4E^2 \sin^4(\theta/2)} \left(W_2(\nu, Q^2) \cos^2(\theta/2) + 2W_1(\nu, Q^2) \sin^2(\theta/2)\right) \quad (1.4)$$

where  $W_1$  and  $W_2$  are related to their elastic counterparts  $G_E$  and  $G_M$ . They are functions

of two independent variables  $\nu$  and  $Q^2$  which correspond to the energy and momentum transfer in the rest frame of the target proton:

$$\nu = E - E' \quad (1.5)$$

$$Q^2 = -q^2 = 4EE' \sin^2(\theta/2) \quad (1.6)$$

The structure functions  $W_1$  and  $W_2$  are underivable from the theory of strong interactions, and must be obtained from the experiment. In 1968 Bjorken proposed to investigate the structure functions in the limit of  $Q^2 \rightarrow \infty$  and  $\nu \rightarrow \infty$  but  $\nu/Q^2$  fixed. He introduced a new variable  $x = Q^2/2M\nu$  which had to be kept constant. The most famous result of this pioneering inelastic  $ep$  scattering experiment was the evidence of so-called *scaling invariance* of the proton structure functions  $W_1(\mu, Q^2)$  and  $W_2(\mu, Q^2)$ , i.e. there was no  $Q^2$  dependence of these functions found. In the Bjorken limit these structure functions tend to depend on the ratio  $x$  only:

$$\lim MW_1(\nu, Q^2) = F_1(x) + O(1/Q^2) \quad (1.7)$$

$$\lim \nu W_2(\nu, Q^2) = F_2(x) + O(1/Q^2) \quad (1.8)$$

This feature is expected for scattering from a point-like particle. Similar result hold for electrons scattering on any point-like particle. Based on this Feynman proposed a model, where the proton consists of quasi-free point like partons in the frame, where the proton is moving with infinite momentum. The cross section of deep inelastic  $ep$  scattering is then

the incoherent sum over all electron-parton scattering cross section:

$$\left(\frac{d\sigma}{dx dQ^2}\right)_{ep \rightarrow eX} = \sum_i \int dx e_i^2 q_i(x) \left(\frac{d\sigma}{dx dQ^2}\right)_{eq_i \rightarrow eq_i} \quad (1.9)$$

where  $q_i(x)$  is the parton momentum density of the parton  $i$  with the charge  $e_i$  inside the proton. The four momentum transfer  $Q^2$  and  $x$  correspond to the mass of the virtual photon and the fraction of the proton momentum carried by the parton which is hit by the exchanged virtual photon, respectively. Deep inelastic scattering experiments were fundamental in understanding the structure of the nucleon. However, the parton density functions as measured in DIS do not provide enough information needed for complete discription of the nucleon structure.

### 1.3 Generalized Parton Distributions

A good way of introducing Generalized Parton Distributions (GPDs) is to start from the description of deep inelastic scattering (DIS),  $ep \rightarrow eX$ . In the Bjorken limit, when the photon virtuality  $Q^2 = -q^2$  and the hadronic energy in center of mass both become large with the ratio  $x_B = Q^2/2\nu$  finite, the dynamics factorizes into a hard partonic subprocess, which can be calculated in perturbation theory, and a parton distribution, which is the probability density for finding a parton of specific momentum fraction  $x$  in the nucleon. The cross section of inclusive  $\gamma^*p$  can be related to the imaginary part of the forward Compton amplitude  $\gamma^*p \rightarrow \gamma^*p$  by using the optical theorem [9]. The parton densities can be thought of as the squared amplitudes for the target fluctuating into the parton with momentum fraction  $x$  and any remnant system. This has the meaning of a probability in the classical sense, at least to leading logarithmic accuracy in  $Q^2$ . The simple factorization

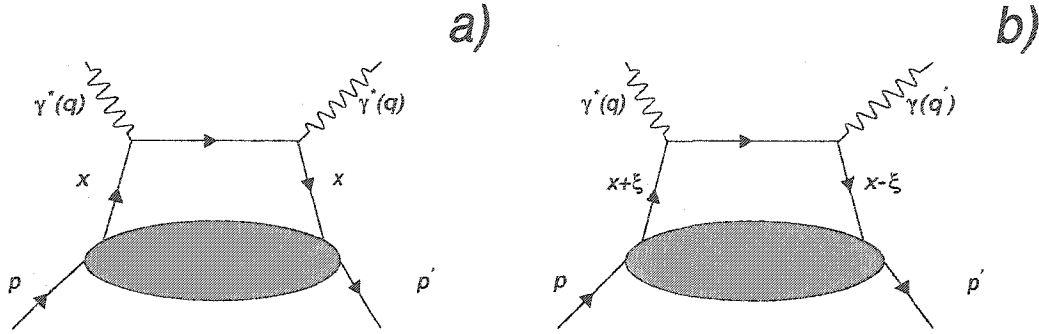


Figure 1-1: a) handbag diagram for the forward Compton amplitude  $\gamma^*p \rightarrow \gamma^*p$ , whose imaginary part gives the DIS cross section. b) Handbag diagram for DVCS in the region  $\xi < x < 1$ .

of dynamics into short- and long-distance parts is not only valid for the forward Compton amplitude, but also for more general case where there is a finite momentum transfer to the target, provided that the virtuality of one of the photons is large. A particular case is where the final photon is on shell, so that it can appear in a physical state. In other words, the limit of large initial photon virtuality  $Q^2$ , with the Bjorken variable and the invariant momentum transfer  $t = (p' - p)$  remaining fixed, must be considered. One then speaks of Deeply Virtual Compton Scattering (DVCS) and the basic process is described by the handbag diagram shown on Figure 1-1, which can be accessed in the exclusive process  $ep \rightarrow ep\gamma$ . The long-distance part, represented by the lower blob, can be parametrized through generalized parton distributions (GPDs).

GPDs also occur in the production of light mesons instead of the  $\gamma$ . If the quantum numbers permit, the GPDs for gluons enter at the same order in  $\alpha_s$  as those for quarks (see Figure 1-1).

The transformation of a virtual photon into a real photon or a meson requires a finite transfer of longitudinal momentum, where longitudinal refers to the direction of the proton

momentum in a frame where  $p$  and  $p'$  move fast. It has been shown that the fraction of momentum lost by the proton is determined by  $x_B$ . If momentum fractions are defined in the symmetric way shown in Figure 1-1, then in the Bjorken limit one has [9]:

$$\xi = \frac{x_B}{2 - x_B} \quad (1.10)$$

where  $\xi$  is called a skewedness variable. The proton and parton momenta are no longer the same on the right and left hand sides of the diagram. Therefore GPDs no longer represent a squared amplitude, but rather the interference between amplitudes describing different quantum fluctuations of a nucleon.

### 1.3.1 Notations

The description of parton densities and related quantities are given in light-cone coordinates. The light-cone momentum  $p^+$  becomes proportional to the momentum of a particle in the infinite momentum frame where  $p^3 \rightarrow \infty$ , but can be used to calculate in any convenient reference frame. For GPDs and for the processes where they appear a commonly used notation is:

$$P = \frac{p + p'}{2}, \quad \Delta = p' - p, \quad t = \Delta^2 \quad (1.11)$$

with  $p$  for the incoming and  $p'$  for the outgoing hadron momentum. For  $\gamma^*p$  scattering we use standard variables:

$$Q^2 = -q^2, \quad W^2 = (p + q)^2, \quad x_B = \frac{Q^2}{2(p \cdot q)} \quad (1.12)$$

where  $q$  is the momentum of the incident  $\gamma^*$ . The skewedness variable is usually defined in

the literature as:

$$\xi = \frac{p^+ - p'^+}{p^+ + p'^+} \quad (1.13)$$

Since the  $p^+$  of physical states are non-negative, the physical region of  $\xi$  is the interval  $(-1, 1)$ .

## 1.4 GPD Formalism

### 1.4.1 Phenomenology of the GPDs

It has been shown that the amplitude of Deeply Virtual Compton Scattering [10] and deeply exclusive production of mesons in the forward direction can be factorized in leading order pQCD into a hard-scattering part, which can be exactly calculated in pQCD, and a non-perturbative nucleon structure part. The later can be parametrized at leading twist in terms of Generalized Parton Distribution (GPD) structure functions. At twist-two level there are four GPDs, denoted  $H$ ,  $\tilde{H}$ ,  $E$ ,  $\tilde{E}$ , which depend on kinematical variables :  $x$ ,  $\xi$  and  $t$ . Where  $x$  (light-cone momentum fraction) is defined as  $k = x\bar{P}^+$ , where  $k$  is the quark loop momentum and  $\bar{P}$  is the nucleon average momentum. The kinematical variable  $\xi$  is defined by  $\Delta = -2\xi\bar{P}$ . The third variable is the total squared momentum transfer to the nucleon ( $t = \Delta^2$ ). On the light-cone the non-perturbative amplitude at leading twist can be parametrized as:

$$\frac{\bar{P}^+}{2\pi} \int dy^- e^{ix\bar{P}^+y^-} \langle p' | \bar{\psi}_\beta(-y/2) \psi_\alpha(y/2) | p \rangle =$$

$$\frac{1}{4} \left\{ (\gamma^-)_{\alpha\beta} [H^q(x, \xi, t) \bar{N}(p') \gamma^+ N(p) + E^q(x, \xi, t) \bar{N}(p') i\sigma^{+k} \frac{\Delta_k}{2m_N} N(p)] + \right.$$

$$(\gamma_5 \gamma^-)_{\alpha\beta} [\tilde{H}^q(x, \xi, t) \bar{N}(p') \gamma^+ \gamma_5 N(p) + \tilde{E}^q(x, \xi, t) \bar{N}(p') \gamma_5 \frac{\Delta^+}{2m_N} N(p)] \quad (1.14)$$

where  $\psi$  is the quark field for flavor  $q$ ,  $m_N$  the nucleon mass and  $N$  the nucleon spinor. The variable  $x$  runs from  $-1$  to  $1$ , hence the momentum fractions defined as  $x - \xi$  and  $x + \xi$  can be either positive or negative. There are two regions for the GPDs: when  $x > \xi$  both partons represent quarks, and for  $x < \xi$  antiquarks [11]. In these regions the GPDs are the generalization of the usual parton distributions from DIS, and in the forward direction, the GPDs  $H$  and  $\tilde{H}$  reduce to the quark density distributions  $q(x)$  and quark helicity distributions  $\Delta q(x)$  obtained from DIS:

$$H^q(x, 0, 0) = \begin{cases} q(x), & x > 0, \\ -\bar{q}(-x), & x < 0. \end{cases} \quad (1.15)$$

$$\tilde{H}^q(x, 0, 0) = \begin{cases} \Delta q(x), & x > 0, \\ \Delta \bar{q}(-x), & x < 0. \end{cases} \quad (1.16)$$

Functions  $E$  and  $\tilde{E}$  are not accessible through DIS, since in the forward limit ( $\Delta \rightarrow 0$ ), the associated tensors in Eq.(1.14) vanish. Therefore  $E$  and  $\tilde{E}$  are accessible through hard exclusive electro-production reactions only and are new leading-twist functions. Similarly, the region  $-\xi < x < \xi$ , corresponds to the limit  $\xi \rightarrow 0$ , is absent in DIS. In this region GPDs behave like a meson distribution amplitudes and contain completely new information about nucleon structure. At finite momentum transfer, the first moments of GPDs are related to the elastic form factors of the nucleon through model independent sum rules. By integrating over  $x$  one can obtain for a particular quark flavor (for any  $\xi$ ):

$$\int_{-1}^{+1} dx H^q(x, \xi, t) = F_1^q(t) \quad (1.17)$$

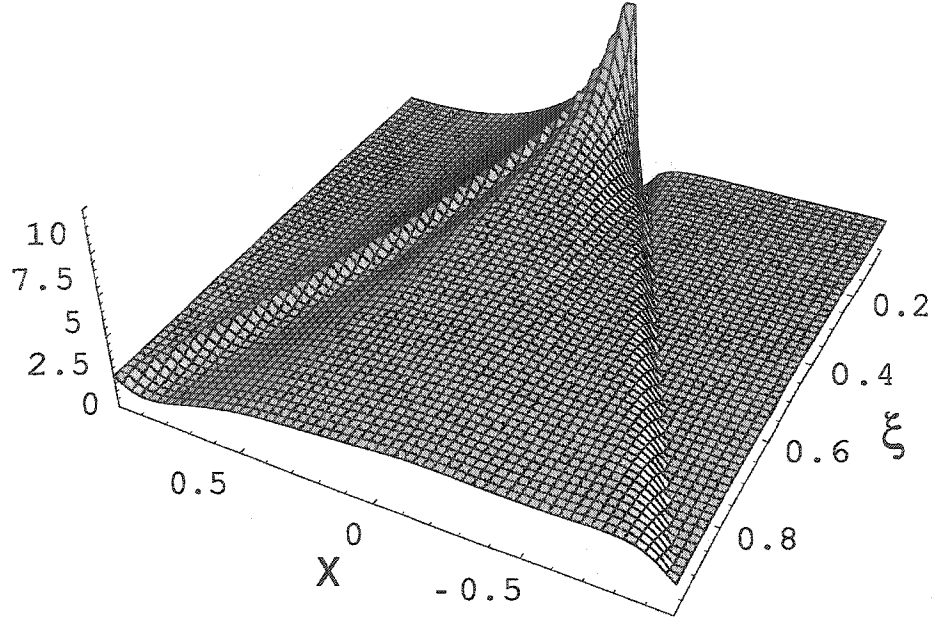


Figure 1-2: Model calculation of GPD  $H(x, \xi, t)$  as a function of  $x$  and  $\xi$  at  $t = 0$ .

$$\int_{-1}^{+1} dx E^q(x, \xi, t) = F_2^q(t) \quad (1.18)$$

$$\int_{-1}^{+1} dx \tilde{H}^q(x, \xi, t) = g_A^q(t) \quad (1.19)$$

$$\int_{-1}^{+1} dx \tilde{E}^q(x, \xi, t) = h_A^q(t) \quad (1.20)$$

where  $F_1^q(t)$  and  $F_2^q(t)$  represent the elastic Dirac and Pauli form factors for the quark flavor  $q$  in the nucleon,  $g_A^q$  is the axial isovector form factor of the nucleon, and  $h_A^q$  is the pseudo-scalar form factor. In the following when referring to the quark flavor form factors the proton form factor is assumed, e.g.  $F_1^u(t) = F_1^{u/p}(t)$ . In this notation, the  $u$ -quark form factor is normalized as  $F_1^u(t=0) = 2$  so as to yield the normalization of 2 for the  $u$ -quark distribution in the proton, similarly the  $d$ -quark form factor is normalized as  $F_1^d(t=0) = 1$  so as to yield the normalization of 1 for the  $d$ -quark distribution in the proton. These

elastic form factors for one quark flavor in the proton are related to the physical nucleon form factors as:

$$\begin{aligned} F_1^{u/p} &= 2F_1^p + F_1^n + F_1^s \\ F_1^{d/p} &= 2F_1^n + F_1^p + F_1^s \end{aligned} \quad (1.21)$$

where  $F_1^p$  and  $F_1^n$  are the proton and neutron electromagnetic form factors respectively, normalized as  $F_1^p(0) = 1$  and  $F_1^n(0) = 0$ . In Eq.(1.21)  $F_1^s$  is the strangeness form factor of the nucleon. Similar relations hold for the Pauli form factors  $F_2^q$ . For the axial vector form factors the isospin decomposition is used:

$$\begin{aligned} g_A^u &= \frac{1}{2}g_A + \frac{1}{2}g_A^0 \\ g_A^d &= -\frac{1}{2}g_A + \frac{1}{2}g_A^0 \end{aligned} \quad (1.22)$$

where  $g_A$  and  $g_A^0$  are the isovector and isoscalar axial form factors of the nucleon respectively. Similar relations exist for  $h_A$ . The isovector axial form factors  $g_A$  is measured experimentally, and is known to be  $g_A(0) \sim 1.267$ .

There is also a sum rule that relates the second moments of GPDs to the angular momentum carried by the quark in the nucleon [1]:

$$\int_{-1}^1 dx x(H^q(x, \xi) + E^q(x, \xi)) = 2J^q \quad (1.23)$$

where  $J^q$  is the fraction of the angular momentum carried by quark flavor  $q$  in the nucleon. The quark helicity in  $J^q$  has been measured in the past decade through polarized deep-inelastic scattering. Therefore, an experimental determination of  $J^q$  allows a measurement

of the quark orbital angular momentum [12]. The sum rule combined with DIS data on helicity distribution will allow us to understand how the nucleon spin is distributed among its constituents, and shed new light on the “spin-puzzle”.

### 1.4.2 Spatial Image of the Nucleon

Deep-inelastic scattering experiments have not only played a crucial role in establishing QCD as theory of strong interactions but have also been an important tool for exploring the quark-gluon structure of hadrons.

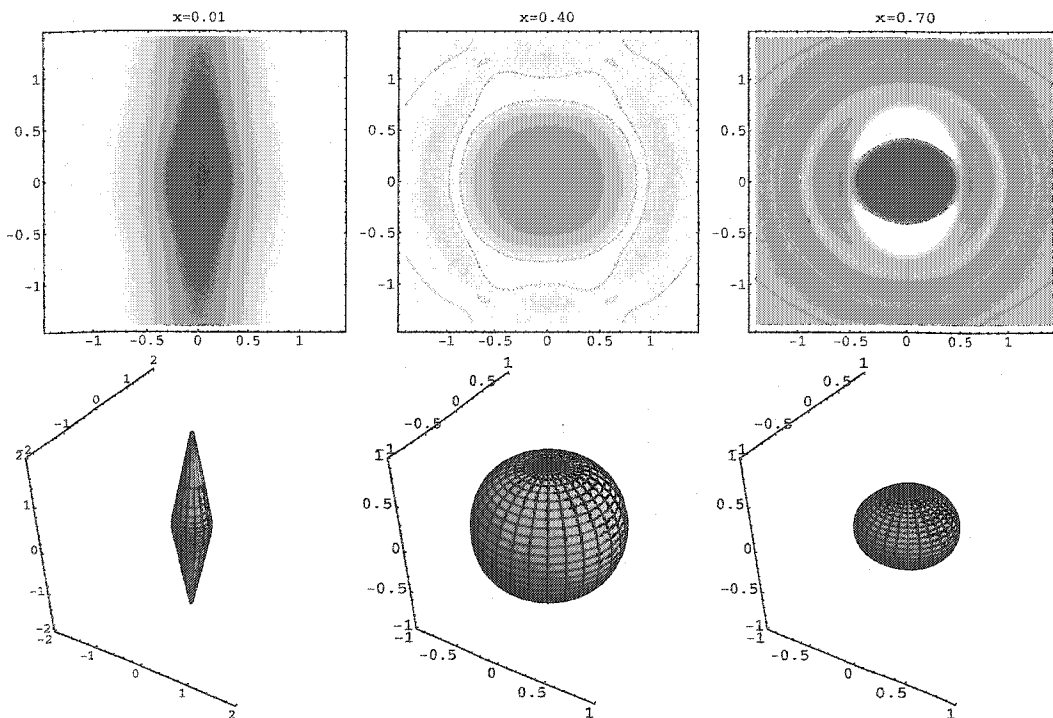


Figure 1-3: The  $u$ -quark phase-space charge distribution at different values of the Feynman momentum for non-factorizable ansatz of generalized parton distributions. The vertical and horizontal axis correspond to  $z$  and  $|\vec{r}_\perp|$ , respectively, measured in femtometers. The [dashed] contours separate regions of positive [darker areas] and negative [lighter areas] densities. Below each contour plot the shape of three-dimensional isodensity contours are presented.

In the Bjorken scaling limit these experiments allow probing parton distribution functions (PDFs), which have a very physical interpretation as the probability density for finding partons carrying the fraction  $x$  of the target's total momentum in the infinite momentum frame [13]. The DIS experiments, due to the probability interpretation of PDFs, have contributed substantially to present intuitive understanding of the quark gluon structure of hadrons.

These forward parton distributions contain no information about the spatial distribution of partons. In the recent calculation it was found ([13],[14]) that knowledge of GPDs at  $\xi = 0$ , can provide information (by Fourier transform) about the longitudinal momentum and transverse position of partons in the target. This is completely new information about the internal structure of the nucleons, and it will allow to understand how the spatial distributions of the partons in the nucleons vary with  $x$  and what is the parton distribution at a given distance from the center of momentum. An example plot is shown in Figure 1-3 [14], where the up-quark charge distribution is calculated from  $H_u(x, \xi, t)$  for various values of  $x = \{0.01, 0.4, 0.7\}$ . The plots show significant change in the distribution on the longitudinal momentum fraction  $x$ . At the small  $x$ , the distribution extends far beyond the normal nucleon size along the  $z$  direction. The physical explanation for this is that the the position space uncertainty of the quarks is large at small  $x$ , and therefore the quarks are de-localized along the longitudinal direction.

In summary, GPDs uniquely connect the charge and current distributions of the nucleon with the forward quark distribution measured in DIS. Recent results demonstrate the applicability of the GPD framework at currently achievable values of  $Q^2$  for DVCS and possibly for vector meson production. New results from experiments combined with theoretical calculations will provide new insights into the internal dynamics of the nucleon unimaginable

few years ago.

### 1.4.3 Parametrization of the GPDs

Extracting GPDs from experimental data is not a simple task. Phenomenological parametrizations of GPDs are necessary to fit the experimental data. One of the commonly used parametrizations of GPDs uses double distributions [10]. In terms of double distribution functions the GDPs are given via:

$$q(x, \xi, t) = \int_{-1}^1 dy \int_{-1+|y|}^{1-|y|} dz \delta(y + \xi z - x) f(y, z, t) \quad (1.24)$$

where  $f(y, z, t)$  is the double distribution function and  $q(x, \xi, t)$  is the corresponding GDP. One of the non-trivial properties of the generalized parton distributions is the polynomiality of their Mellin moments [11] which follows from the Lorentz invariance of nucleon matrix elements. Presenting GPDs through double distribution functions leads to a violation of the polynomiality condition. This problem has been resolved by taking into account an extra term, the so-called D-term [15], assuming two-components for the GPDs. For the unpolarized case for each  $i$ -flavor of quarks one has:

$$\begin{aligned} H_i(x, \xi, t) &= q_i(x, \xi, t) + \frac{1}{N_f} \theta\left(1 - \left|\frac{x}{\xi}\right|\right) D(x, \xi, t) \\ E_i(x, \xi, t) &= r_i(x, \xi, t) - \frac{1}{N_f} \theta\left(1 - \left|\frac{x}{\xi}\right|\right) D(x, \xi, t) \end{aligned} \quad (1.25)$$

with the D-term contributing equally to all  $N_f$  active quark species. In Eq.(1.25)  $r_i$  is the parametrization of  $E$  and has similar form with  $q_i$ . Similar equations exist for gluonic GPDs with gluonic D-term,  $(1/N_f)D(x/\xi) \rightarrow D_G(x/\xi)$ . The D-term is an antisymmetric function

of  $x/\xi$  and drops out in the sum  $H + E$ . Due to its antisymmetry the D-term does not enter into the sum rules, therefore the  $t$  dependence is not constrained by it. The following model is used:

$$D(z, t) = \left(1 - \frac{t}{m_D^2}\right)^{-3} D(x/\xi) \quad (1.26)$$

where the  $t$ -dependence is characterized by the cutoff mass  $m_D$ , considered as a free parameter. The  $q_i$  in Eq.(1.25) represent sums over valence and sea quarks, and can be further decomposed into these components to extract the momentum transfer dependence into valence and sea form factors, as:

$$q_i(x, \xi, t) = F_1^{i, val}(t) q_i^{val}(x, \xi) + F_1^{sea}(t) q_i^{sea}(x, \xi) \quad (1.27)$$

where  $i = u, d, s$ , and  $q_s^{val} = 0$  for the  $s$ -quark. At this point the  $(x, \xi)$  dependence of  $r_i(x, \xi, t)$  is not constrained at all. Since its first moment is given by the Pauli form factor, it is extracted from  $r_i(x, \xi, t)$  and the remainder is set to be equal to  $q(x, \xi)$ :

$$r_i(x, \xi, t) = F_2^{i, val}(t) q_i^{val}(x, \xi) + F_2^{sea}(t) q_i^{sea}(x, \xi) \quad (1.28)$$

here the valence  $u$ - and  $d$ - quark form factors as before are extracted from proton and neutron form factors, via:

$$2F_{1,2}^{u, val}(t) = 2F_{1,2}^p(t) + F_{1,2}^n(t) \quad 2F_{1,2}^{d, val}(t) = F_{1,2}^p(t) + 2F_{1,2}^n(t) \quad (1.29)$$

The Dirac and Pauli form factors are fairly well known from experimental measurements,

and in the small- $t$  region can be parametrized by a dipole form:

$$G_E^p(t) = \frac{1}{1+k_p} G_M^p(t) = \frac{1}{k_n} G_M^n(t) = \left(1 - \frac{t}{m_V^2}\right)^{-2} \quad (1.30)$$

where  $k_p = 1.793$  and  $k_n = -1.913$  are the proton and neutron magnetic moments, respectively. And  $m_V$  is a cutoff mass. The electric form factor of the neutron is set to  $G_E^n = 0$ . The corresponding quark Sachs form factors in terms of Dirac and Pauli form factors are given via:

$$G_E^i(t) = F_1^i(t) + \frac{t}{4M^2} F_2^i(t)$$

$$G_M^i(t) = F_1^i(t) + F_2^i(t)$$

The sea-quark form factors in terms of Sachs form factors read:

$$G_E^{sea}(t) = \frac{1}{1+k_{sea}} G_M^{sea} = \left(1 - \frac{t}{m_{sea}^2}\right)^{-3} \quad (1.31)$$

where  $m_{sea}$  is another cutoff mass. The slope of  $F_1^{sea}$  is given by [16]:

$$B_{sea} = \left. \frac{\delta F_1^{sea}}{\delta t} \right|_{t=0} = \frac{3}{m_{sea}^2} - \frac{k_{sea}}{4M^2} \quad (1.32)$$

where  $B_{sea}$  and  $k_{sea}$  are two free parameters. The parameter  $k_{sea}$  enter in the sum rule which gives the fraction of the orbital angular momentum carried by quarks. With the above mentioned assumption of  $r_i = q_i$ , the spin sum rule reads:

$$J^q = \lim_{\Delta \rightarrow 0} \sum_{i=u,d,s} \frac{1}{2} \int_{-1}^1 dx x \left( H^i(x, \xi, t, Q^2) + E^i(x, \xi, t, Q^2) \right) \quad (1.33)$$

$$= \frac{1}{2} \left( (1 + k_p + k_n/2) P^{u,val} + (1 + k_p + k_n) P^{d,val} + (1 + k_{sea}) P^{sea} \right)$$

where the momentum fractions carried by quarks  $P^i$  can be deduced from deeply inelastic data. The quarks are modeled as a product of a profile function  $\pi$  with conventional quark ( $f_i(y)$ ) and antiquark ( $\bar{f}_i(y)$ ) densities using Eq.(1.24). This is possible to do, since the D-term does not affect the GPDs in the forward limit. For the sea and valence quark contributions we have [14]:

$$f_i^{val}(y, z) = f_i^{val}(y) \theta(y) \pi(|y|, z, b_{val})$$

$$f_i^{sea}(y, z) = \left( \bar{f}_i(y) \theta(y) - \bar{f}_i(-y) \theta(-y) \right) \pi(|y|, z, b_{sea})$$

where the definition of valence densities  $f_i^{val} = f_i(y) - \bar{f}_i(y)$  is used. The profile function is assumed to be universal for both valence- and sea-quark species and it reads:

$$\pi(y, z; b) = \frac{\Gamma(b + \frac{3}{2})}{\sqrt{\pi} \Gamma(b + 1)} \frac{[(1 - y)^2 - z^2]^b}{(1 - y)^{2b+1}} \quad (1.34)$$

The parameter  $b$  encodes the skewedness effect, i.e., a larger value of  $b$  suppresses  $\xi$  dependence, and  $q^i(x, \xi, Q^2)$  reduces to the parton density  $f^i(x, Q^2)$  in the limit of  $b \rightarrow \infty$ . This limit is called the forward parton distribution model (FPD). One may choose the asymptotic distribution amplitude in case of valence quarks, which implies  $b_{val} = 1$ . In case of sea quarks  $b_{sea}$  is considered to be a free parameter. The adjustment of this parameter was made to predict measurements done by H1 experiment at HERA at small- $x_B$  (discussed in [16]). This parametrization with different parameters of  $B_{sea}$ ,  $k_{sea}$ ,  $b_{val}$  and  $b_{sea}$  was used to fit the experimentally measured beam spin asymmetries at HERMES and CLAS (discussed

in section 1.5.1).

#### 1.4.4 Twist-3 GPDs

Recently the DVCS amplitude has been computed introducing a term of the order  $O(1/Q)$  [17]. Inclusion of this term is necessary to ensure the electromagnetic gauge invariance of the DVCS amplitude to the order of  $\Delta/Q$ . At the order of  $1/Q$  the DVCS amplitude depends on a new set of generalized parton distributions:

$$F^\mu(x, \xi, t) = \frac{\bar{P}^+}{2\pi} \int_{-\infty}^{+\infty} dy^- e^{ix\bar{P}^+y^-} \langle p' | \bar{\phi}(-y/2) \gamma^\mu \phi(y/2) | p \rangle \Big|_{y^+ = y^\perp = 0}$$

$$\tilde{F}^\mu(x, \xi, t) = \frac{\bar{P}^+}{2\pi} \int_{-\infty}^{+\infty} dy^- e^{ix\bar{P}^+y^-} \langle p' | \bar{\phi}(-y/2) \gamma^\mu \gamma_5 \phi(y/2) | p \rangle \Big|_{y^+ = y^\perp = 0} \quad (1.35)$$

The index  $\mu$  in the above equation projected into the “plus” light-cone direction ( $\mu = +$ ) (see Eq.(1.14)). The case of  $\mu = -$  corresponds to the twist-4 GPDs which contribute to the DVCS amplitude at the order of  $O(1/Q^2)$ . The twist-three GPDs correspond to the  $\mu = \perp$ . The twist-3 GPDs in Wandzura-Wilczek approximation (where quark-gluon-antiquark correlations are neglected) can be related to twist-2 GPDs. The operators entering the definition of twist-3 GPDs  $F^\mu$  can be decomposed into so-called WW terms  $F_\pm^{WW}$  and a function containing new dynamical information arising from antiquark-gluon-quark correlations ( $F_\pm^{qGq}$ ):

$$F_\pm^3 = F_\pm^{WW} + F_\pm^{qGq} \quad (1.36)$$

where the WW parts are expressed in terms of twist-2 functions and have the following form:

$$\begin{aligned} F_+^{WW}(x, \xi) &= \int_{-1}^1 \frac{dy}{\xi} W_+ \left( \frac{x}{\xi}, \frac{y}{\xi} \right) \left( y \frac{\overleftarrow{\partial}}{\partial y} - \xi \frac{\overrightarrow{\partial}}{\partial \xi} \right) F(y, \xi) - \frac{1}{\xi} F(x, \xi) - \frac{4M^2 F_+^\perp(x, \xi)}{(1-\xi^2)(t-t_{\min})}, \\ F_-^{WW}(x, \xi) &= - \int_{-1}^1 \frac{dy}{\xi} W_- \left( \frac{x}{\xi}, \frac{y}{\xi} \right) \left( y \frac{\overleftarrow{\partial}}{\partial y} - \xi \frac{\overrightarrow{\partial}}{\partial \xi} \right) F(y, \xi) - \frac{4M^2 F_-^\perp(x, \xi)}{(1-\xi^2)(t-t_{\min})}, \end{aligned} \quad (1.37)$$

for “+” and “-” components of the twist-3 GDPs in the WW approximation. And  $t_{\min}$  is given by:

$$-t_{\min} = Q^2 \frac{2(1-x_B)(1-\sqrt{1+\epsilon^2}) + \epsilon^2}{4x_B(1-x_B) + \epsilon^2} \approx \frac{M^2 x_B^2}{1-x_B + x_B M^2/Q^2} \quad (1.38)$$

The functions  $F_\pm^\perp$  are given by:

$$\begin{aligned} H_\pm^\perp(x, \xi) &= \mp \frac{\Delta^2}{4M^2} \int_{-1}^1 dy \left\{ \xi W_\pm \left( \frac{x}{\xi}, \frac{y}{\xi} \right) (H+E)(y, \xi) - W_\mp \left( \frac{x}{\xi}, \frac{y}{\xi} \right) \tilde{H}(y, \xi) \right\}, \\ E_\pm^\perp(x, \xi) &= \pm \int_{-1}^1 dy \left\{ \xi W_\pm \left( \frac{x}{\xi}, \frac{y}{\xi} \right) (H+E)(y, \xi) - W_\mp \left( \frac{x}{\xi}, \frac{y}{\xi} \right) \tilde{H}(y, \xi) \right\}, \\ \tilde{H}_\pm^\perp(x, \xi) &= \pm \int_{-1}^1 dy \left\{ \xi \left( 1 - \frac{\Delta^2}{4M^2} \right) W_\pm \left( \frac{x}{\xi}, \frac{y}{\xi} \right) \tilde{H}(y, \xi) + \frac{\Delta^2}{4M^2} W_\mp \left( \frac{x}{\xi}, \frac{y}{\xi} \right) (H+E)(y, \xi) \right\}, \\ \tilde{E}_\pm^\perp(x, \xi) &= \pm \frac{1}{\xi} \int_{-1}^1 dy \left\{ W_\pm \left( \frac{x}{\xi}, \frac{y}{\xi} \right) \tilde{H}(y, \xi) - \xi W_\mp \left( \frac{x}{\xi}, \frac{y}{\xi} \right) (H+E)(y, \xi) \right\}. \end{aligned} \quad (1.39)$$

The  $W_\pm$  functions are called  $W$ -kernels and are defined by:

$$\begin{aligned} W_\pm \left( \frac{x}{\xi}, \frac{y}{\xi} \right) &= \frac{1}{2\xi} \left\{ W \left( \frac{x}{\xi}, \frac{y}{\xi} \right) \pm W \left( -\frac{x}{\xi}, -\frac{y}{\xi} \right) \right\} \\ W(x, y) &= \frac{\theta(1+x) - \theta(x-y)}{1+y}. \end{aligned} \quad (1.40)$$

As it turns out, only the difference  $\mathcal{F}_+^3 - \mathcal{F}_-^3$  enters in the amplitude of DVCS, therefore

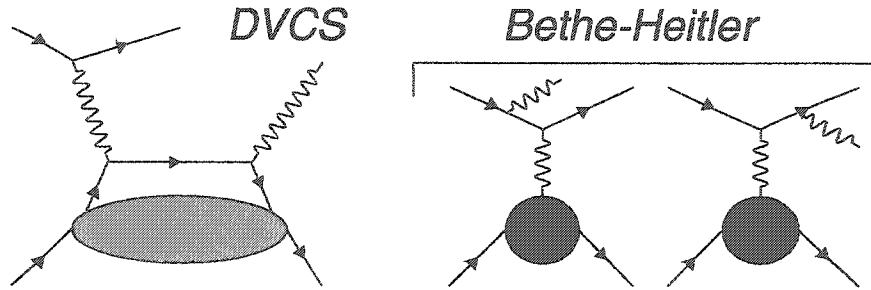


Figure 1-4: Handbag diagrams for DVCS and Bethe-Heitler processes.

only four independent GPDs remain in twist-3 level. In the WW approximation, which neglects the antiquark-gluon-quark correlation, all the twist-3 GPDs are entirely determined by the four twist-2 GPDs  $H, E, \tilde{H}$  and  $\tilde{E}$ .

## 1.5 Deeply Virtual Compton Scattering

Deeply Virtual Compton Scattering is a very promising reaction for accessing GPDs experimentally. Theoretical studies of the DVCS amplitude have done recent advances and it has been derived up to twist-3 accuracy. There are four twist-2 level GDPs involved in the description of DVCS amplitude (GPDs  $H^q, \tilde{H}^q, E^q, \tilde{E}^q$ ), plus four new structure functions from gluonic transversity distribution.

DVCS has the same final state as the Bethe-Heitler (BH) reaction, where a photon is emitted by the incoming or outgoing electron (Figure 1-4):

$$\gamma^*(q) + N(p) \rightarrow \gamma(q') + N(p') \quad (1.41)$$

and therefore the experiment measures the sum of amplitudes of these two processes. The

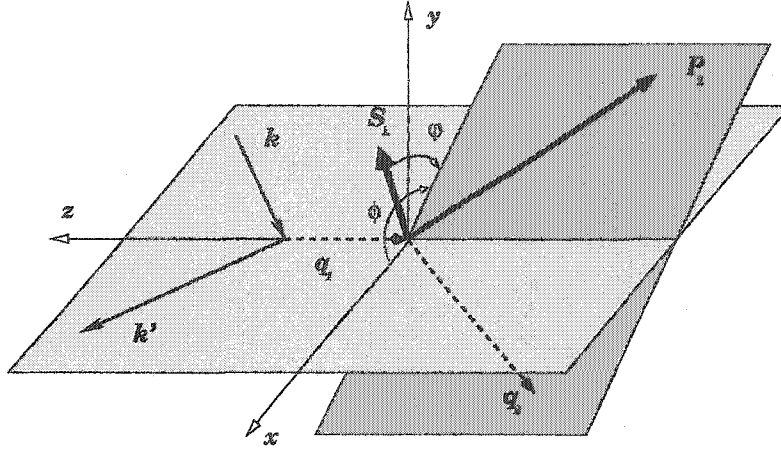


Figure 1-5: The kinematics of lepton production in the rest frame of the target. The  $z$ -direction is chosen counter-along the three momentum of the incoming virtual photon. The lepton three-momenta form the lepton scattering plane, while the recoil proton and outgoing real photon define the hadron scattering plane. In this reference system the azimuthal angle of the scattered lepton is  $\phi_l = 0$ , while the azimuthal angle between the lepton plane and the recoiled proton momentum is  $\phi_N = \phi$ . When the hadron is transversely polarized (in the reference frame)  $S_{\perp} = (0, \cos\Phi, \sin\Phi, 0)$ , the angle between the polarization vector and the scattered hadron is denoted as  $\phi = \Phi - \phi_N$ .

cross section of deeply virtual production of a photon can be presented as:

$$\frac{d\sigma}{dydx_B dtd\Phi} = \frac{\alpha^3 x_B y}{16\pi^2 Q^2 \sqrt{1+\epsilon^2}} \left| \frac{T}{e^3} \right|^2 \quad (1.42)$$

where  $x_B$  is the Bjorken scaling variable,  $y = (p \cdot (q - q')) / (p \cdot q)$  is the lepton energy function,  $Q^2$  is the virtuality of the photon,  $\alpha$  is electromagnetic interaction constant,  $e$  is the electron charge,  $\Phi$  - the azimuthal angle between lepton and hadron planes (see Figure 1-5), and  $\epsilon$  is the polarization of the virtual photon. In the Eq.(1.42),  $\phi = \phi_N - \phi_l$  is the angle between hadron and lepton planes. The frame is rotated with respect to the laboratory frame in such a way that the virtual photon four-momentum has no transverse component. The kinematics is fixed by choosing the  $z$ -component of the virtual photon momentum to be

negative and the  $x$ -component of the incoming lepton to be positive:

$$k = (E, E\sin\theta_l, 0, E\cos\theta_l), \quad q_1 = (q_1^0, 0, 0, -|q_1^3|)$$

The amplitude  $\mathcal{T}$  is the sum of the DVCS ( $\mathcal{T}_{DVCS}$ ) and Bethe-Heitler ( $\mathcal{T}_{BH}$ ) amplitudes, given as:

$$\mathcal{T}^2 = |\mathcal{T}_{BH}|^2 + |\mathcal{T}_{DVCS}|^2 + \mathcal{I} \quad (1.43)$$

where  $\mathcal{I}$  is the interference term:

$$\mathcal{I} = \mathcal{T}_{DVCS}\mathcal{T}_{BH}^* + \mathcal{T}_{DVCS}^*\mathcal{T}_{BH} \quad (1.44)$$

The Bethe-Heitler amplitude is real and is parametrized in terms of electromagnetic form factors, which are known from other measurements. The azimuthal angular dependence of each term arises from the contraction of leptonic and hadronic tensors [16].

The squared DVCS amplitude  $\mathcal{T}_{DVCS}$ , Bethe-Heitler amplitude  $\mathcal{T}_{BH}$ , and the interference term read ([16]):

$$|\mathcal{T}_{BH}|^2 = \frac{e^6}{x_B^2 y^2 (1 + \epsilon^2)^2 t P_1(\phi) P_2(\phi)} \left\{ c_0^{BH} + \sum_{n=1}^2 c_n^{BH} \cos(n\phi) + s_1^{BH} \sin(\phi) \right\} \quad (1.45)$$

$$|\mathcal{T}_{DVCS}|^2 = \frac{e^6}{y^2 Q^2} \left\{ c_0^{DVCS} + \sum_{n=1}^2 [c_n^{DVCS} \cos(n\phi) + s_n^{DVCS} \sin(n\phi)] \right\} \quad (1.46)$$

$$I = \frac{\pm e^6}{x_B y^3 t P_1(\phi) P_2(\phi)} \left\{ c_0^I + \sum_{n=1}^2 [c_n^I \cos(n\phi) + s_n^I \sin(n\phi)] \right\} \quad (1.47)$$

where the  $+$  ( $-$ ) in the interference term stands for negatively (positively) charged beam. Generation of new harmonics in the azimuthal angular dependence for the Fourier coeffi-

coefficients, presented below, are terminated at twist-3 level. The coefficients  $c_1^I, s_1^I$  and  $c_0^{DVCS}$  arise at twist-2 level, and the rest provides an additional angular dependence and is given in terms of twist-2 ( $c_0^{BH}$ ) and twist-3 ( $c_1^{DVCS}, s_1^{DVCS}, c_2^I, s_2^I$ ) GPDs. The effects of dynamical higher-twist contributions are neglected in consequent considerations, they will give power suppressed corrections to the Fourier coefficients, discussed above.

All Fourier coefficients for all the  $\mathcal{T}_{BH}, \mathcal{T}_{DVCS}$  and  $I$  can be found in [16]. Here only those are presented which are relevant for DVCS single spin asymmetries. For the phenomenology of GPDs, the interference term (I) is the most interesting quantity since it is linear in Compton Form Factors (CFF), which simplifies their disentanglement from experimental measurements. For an unpolarized target, the Fourier harmonics for the interference term are given:

$$c_0^I = -8(2-y)\Re\left\{\frac{(2-y)^2}{1-y}K^2\mathcal{C}^I(\mathcal{F}) + \frac{\Delta^2}{Q^2}(1-y)(2-x_B)(\mathcal{C}^I + \Delta\mathcal{C}^I)(\mathcal{F})\right\}, \quad (1.48)$$

$$\begin{Bmatrix} c_1^I \\ s_1^I \end{Bmatrix} = 8K \begin{Bmatrix} -(2-2y+y^2) \\ \lambda y(2-y) \end{Bmatrix} \begin{Bmatrix} \Re \\ \Im \end{Bmatrix} \mathcal{C}^I(\mathcal{F}), \quad (1.49)$$

$$\begin{Bmatrix} c_2^I \\ s_2^I \end{Bmatrix} = \frac{16K^2}{2-x_B} \begin{Bmatrix} -(2-y) \\ \lambda y \end{Bmatrix} \begin{Bmatrix} \Re \\ \Im \end{Bmatrix} \mathcal{C}^I(\mathcal{F}^{\text{eff}}), \quad (1.50)$$

$$c_3^I = -\frac{8Q^2K^3}{M^2(2-x_B)^2}\Re\mathcal{C}_T^I(\mathcal{F}_T). \quad (1.51)$$

where the  $\mathcal{C}$  are coefficient functions. They depend on GPDs, integrated over the momentum fraction. For the harmonics involving  $H, E, \tilde{H}, \tilde{E}$  they read:

$$C_{unp}^I = F_1\mathcal{H} + \frac{x_B}{2-x_B}(F_1 + F_2)\tilde{\mathcal{H}} - \frac{\Delta^2}{4M^2}F_2\mathcal{E} \quad (1.52)$$

and the power-suppressed contributions are defined as:

$$\Delta C_{unp}^{\mathcal{I}} = -\frac{x_B}{2-x_B}(F_1 + F_2) \cdot \left( \frac{x_B}{2-x_B}(\mathcal{H} + \mathcal{E}) + \tilde{\mathcal{H}} \right) \quad (1.53)$$

Here again only coefficient functions for the interference term with unpolarized target are presented. The coefficient functions for DVCS and BH amplitudes can be found in [16].

The coefficient functions are given in terms of Compton Form Factors (CFF), which are related to GPDs by a convolution of perturbatively calculable coefficient functions  $C^{\pm}$ :

$$\begin{aligned} \left\{ \mathcal{H}, \mathcal{E}, \mathcal{H}_+^3, \mathcal{E}_+^3, \tilde{\mathcal{H}}_-^3, \tilde{\mathcal{E}}_-^3 \right\}(\xi) &= \int_{-1}^1 dx C^{(-)}(\xi, x) \left\{ H, E, H_+^3, E_+^3, \tilde{H}_-^3, \tilde{E}_-^3 \right\}(x, \eta)|_{\eta=-\xi}, \\ \left\{ \tilde{\mathcal{H}}, \tilde{\mathcal{E}}, \tilde{\mathcal{H}}_+^3, \tilde{\mathcal{E}}_+^3, \mathcal{H}_-^3, \mathcal{E}_-^3 \right\}(\xi) &= \int_{-1}^1 dx C^{(+)}(\xi, x) \left\{ \tilde{H}, \tilde{E}, \tilde{H}_+^3, \tilde{E}_+^3, H_-^3, E_-^3 \right\}(x, \eta)|_{\eta=-\xi}, \end{aligned} \quad (1.54)$$

where the terms of  $1/Q^2$ -power have been neglected. The summations over quark species on the right hand side is implied in the above equation, so that they have to be understood as follows:

$$C^{(\pm)} F \rightarrow \sum_{i=u,d,s} C_i^{(\pm)} F_i \quad (1.55)$$

where the perturbative expansion of  $C^{(\pm)}$  is given by:

$$C^{(\pm)} = C_{(0)}^{(\pm)} + \frac{\alpha_s}{2\pi} C_{(1)}^{(\pm)} + \mathcal{O}(\alpha_s) \quad (1.56)$$

At LO in the QCD coupling constant the coefficient functions for even (-) and odd (+) parity sectors read:

$$\xi C_{(0)i}^{(\pm)} = \frac{Q_i^2}{1-x/\xi-i0} \pm \frac{Q_i^2}{1+x/\xi-i0} \quad (1.57)$$

where  $Q_i$  is the quark charge. These formulae are complete results of the real-photon production at twist-2 level. The strategy for accessing the GPDs is to measure experimentally the Fourier harmonics  $c_i^I$  and  $s_i^I$ . The table 1.1 shows which sector (Im and Re) can be accessed at twist-2 and twist-3 measurements of Fourier coefficients. The cross section for

twist	sector $\mathcal{C}$ 's	harmonics in I unpol.	extraction of CFFs	$\alpha$ (of $Q^{-\alpha}$ )	$\Delta_{\perp}^I$ behavior (unpol)
two	$\Re\mathcal{C}(\mathcal{F}), \Delta\mathcal{C}(\mathcal{F})$	$c_1, c_0$	over complete	1,2	1
	$\Im\mathcal{C}(\mathcal{F}), \Delta\mathcal{C}(\mathcal{F})$	$s_1, -$	over complete	1,2	1
three	$\Re\mathcal{C}(\mathcal{F}^{eff})$	$c_2$	complete	2	2
	$\Im\mathcal{C}(\mathcal{F}^{eff})$	$s_2$	complete	2	2
two	$\Re\mathcal{C}_T(\mathcal{F}_T)$	$c_3$	$1 \times \Re$ of 4	1	3
	$\Im\mathcal{C}_T(\mathcal{F}_T)$	$-$	$3 \times \Im$ of 4	1	3

Table 1.1: Fourier coefficients  $c_i^I$  and  $s_i^I$  of the interference term.

leptoproduction of the real photon has a quite rich angular structure. The goal of experiments is to pin down the GPDs and this requires a clean disentanglement of different components of the cross section. So far eight CFFs have been introduced at twist-2 level, where four of them related to gluonic transversity contributions. Four new GPDs arise at twist-three level. This sectors can be separated due to their characteristic azimuthal dependence, summarized in Table 1.1, for the interference ( $\mathcal{I}$ ) term.

### 1.5.1 Previous Measurements

The azimuthal dependence of the beam spin asymmetry has been recently measured by the CLAS [18] and HERMES [19] collaborations with electron (4.25 GeV) and positron (27.6 GeV) beams, respectively, scattered on hydrogen target. In both experiments the average value of  $\langle y \rangle$  was large, thus the BH part of the total cross section dominates over the DVCS, so the denominator of the beam spin asymmetries ( $d\sigma^{\uparrow} + d\sigma^{\downarrow}$ ) is dominated by the BH contribution, with  $c_{0,unp}^{BH}$ -coefficient being the dominant one, and higher har-

monics are suppressed. The BH part provides a much stronger contribution for the CLAS experiment than for HERMES. Thus, the  $\phi$  dependence of the BH propagator in  $A_{LU}(\phi)$  almost cancels. A simple model with several free parameters was introduced in the preceding sections to calculate beam spin asymmetries in DVCS and compare them with available measurements. In [16] three models are considered, summarized in Table 1.2. After fix-

model	$b_{val}$	$b_{sea}$	$B_{sea}[GeV^{-2}]$	$\kappa_{sea}$
A	1	$\infty$	9	0
B	$\infty$	$\infty$	9	-3
C	1	1	5	0

Table 1.2: Parameters sets for models of H- and E- type GPDs.

ing the parameters in the sea-quark sector from H1 data, numerical estimates were given for unpolarized fixed target experiments. In these kinematics the azimuthal dependence is expected to be approximately given by a  $\sin(\phi)$  function [20]:

$$A_{LU}(\phi) \sim \pm \frac{x_B}{y} \frac{s_{1,unp}^I}{c_{0,unp}^{BH}} \approx \mathcal{I}m(F_1 \mathcal{H} + \frac{x_B}{2-x_B} (F_1 + F_2) \tilde{\mathcal{H}} - \frac{t}{4M^2} F_2 \mathcal{E}) \sin(\phi) \quad (1.58)$$

where higher harmonics are suppressed by  $\Delta/Q$ . In this approximation  $A_{LU}$  is linear in CFFs, and within presented model the dominant contribution arises from  $\mathcal{I}m\mathcal{H}$ . In the leading order (LO) the imaginary part is given by the GPDs on the diagonal  $x = \pm\xi$ . Thus, the uncertainties due to poor knowledge of GPDs are minimized in beam spin asymmetries. The  $D$ -term appears to affect the asymmetries only slightly, nevertheless, it was included in calculations according to the model described above and the slope parameter was set equal to the sea-slope parameter ( $B_D = B_{sea}$ ). The results of the CLAS and HERMES measurements are shown in Figure 1-6 along with GPD expectations at twist-3 level for

LO CFFs. For CLAS kinematics, due to higher average  $\langle y \rangle$ , a stronger contamination by higher harmonics is induced by the squared DVCS term in  $d\sigma^\uparrow + d\sigma^\downarrow$  as well as twist-three effects. The model predictions for the CLAS experiment, plotted in Figure 1-6 (b), have a much smaller deviation from  $\sin(\phi)$  than the HERMES one, shown on Figure 1-6 (a). Calculations with model A are compatible with the HERMES data (solid curve). The experimental result for integrated asymmetry from HERMES was:

$$A_{LU} = -0.23 \pm 0.04(stat) \pm 0.03(syst)$$

$$A_{LU}(MODEL A) = -0.27 \quad (1.59)$$

If smaller slope parameter  $B_{sea}$  or a smaller  $b_{sea}$  parameter is considered, the absolute value of the asymmetry increases. In the model C, for example, it leads to:

$$A_{LU}(MODEL C) = -0.37$$

with an obvious deviation from  $\sin(\phi)$ -like shape (dashed curve), which is mainly due to kinematical effects. On the other hand the larger value of  $b_{val}$  and a smaller  $\kappa_{sea}$ , going beyond the WW-approximation, decrease the absolute value of  $A_{LU}$ . The effects due to antiquark-gluon-quark correlations can be demonstrated by assuming a large contribution proportional to the twist-two one, with a phase difference  $\phi^{qGq}$ :

$$\mathcal{F}^{qGq} = \frac{1}{\xi} |\mathcal{F}| \cdot \exp[i \arg(\mathcal{F}) + i\phi^{qGq}]$$

where  $\mathcal{F} = (\mathcal{H}, \mathcal{E}, \tilde{\mathcal{H}})$ . And with  $\phi^{qGq} = -\pi/3$ , model B gives  $A_{LU} = -0.16$ , which is also compatible with data (dash-dotted curve). The measurements of the CLAS collaboration,

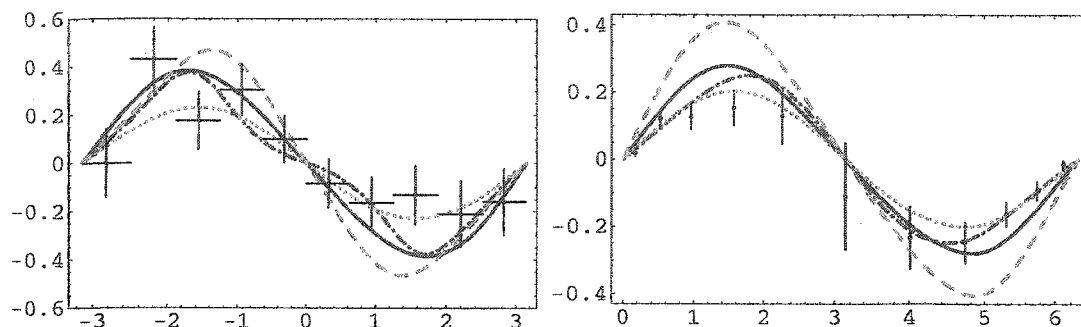


Figure 1-6: The beam-spin asymmetry as function of azimuthal angle measured at HERMES a) in reaction  $e^+p \rightarrow e^+p\gamma$  with initial beam energy  $27.6\text{GeV}$  kinematical. (b) BSA from CLAS in  $ep \rightarrow ep\gamma$  at  $E = 4.25\text{GeV}$

which were fitted with function:

$$A_{LU}(\phi) = \alpha \sin(\phi) + \beta \sin(2\phi) \quad (1.60)$$

gives:

$$\alpha = 0.202 \pm 0.028(\text{stat}) \pm 0.013(\text{syst})$$

$$\beta = -0.024 \pm 0.021(\text{stat}) \pm 0.009(\text{syst})$$

The  $\beta$ -parameter is compatible with zero. The calculations with model A (solid curve) and C (dashed curve) failed to describe the data, giving:

$$(\text{MODEL A}) \quad \alpha = 0.28, \beta = 0.028$$

$$(\text{MODEL C}) \quad \alpha = 0.40, \beta = 0.014$$

Using model B and going beyond the WW-approximation by including antiquark-gluon-quark correlation effects with phase difference  $\phi^{qGq} = \pi$ , one can get a result compatible

with the CLAS measured asymmetry (dash-dotted curve):

$$\alpha = 0.24, \quad \beta = -0.03$$

whereas for model B in the WW-approximation one gets:

$$\alpha = 0.24, \quad \beta = 0.014$$

where the  $\alpha$  value seems to be insensitive to antiquark-gluon-quark contribution, but the  $\beta$  term is quite different. Model A fails to describe the experimentally measured asymmetry from CLAS, however, model B is in fairly good agreement with the measurement. Note that contrary to  $\alpha$ , the second harmonic parametrized by  $\beta$  is very sensitive to quark-gluon-quark correlations [21].

## CHAPTER 2

# EXPERIMENTAL SETUP

The experiment was performed using electron beam provided by Continuous Electron Beam Facility (CEBAF) at the Thomas Jefferson National Lab (Newport News, VA).

### 2.1 Accelerator

The CEBAF accelerator is a superconducting radio frequency (RF) electron accelerator, devoted to the investigation of the structure of mesons, nucleons and nuclei using a high power electron or photon beam with energies up to 6 *GeV*, with a resolution of  $< 0.01\%$  and 100% duty cycle. The primary electron beam from the accelerator is separated and sent to three different experimental Halls (A,B and C). An RF chopping system (operating at 499 *MHz*) is used to develop a 3-beam 1.4971 *GHz* bunch train at 100 *keV*. The beam is then longitudinally compressed into 2 $ps$  bunches separated by 2.0039 *ns* intervals. The beam from the injector is accelerated in the recirculating beam-line (Figure 2-1), with two linear accelerators joined by two 180<sup>0</sup> arcs with radius of 80 *m*. The linear accelerators are equipped with twenty cryomodules, each containing eight superconducting niobium

cavities. The accelerating cavities are kept superconducting at temperature  $2\text{ K}$  with liquid helium, produced at the Lab's Central Helium Liquefier (CHL). The beam is steered and focused while passing each arc using quadrupole and dipole magnets. The beam, after recirculating in the linac and reaching the desired energy, is delivered to the experimental halls. The CEBAF accelerator delivers beam currents sufficient to achieve luminosities of several times  $10^{38}\text{ cm}^{-2}\text{ s}^{-1}$  to Halls A and C. The luminosity achievable in Hall B is limited by the maximum rates in the detector to about  $2 \times 10^{34}\text{ cm}^{-2}\text{ s}^{-1}$ .

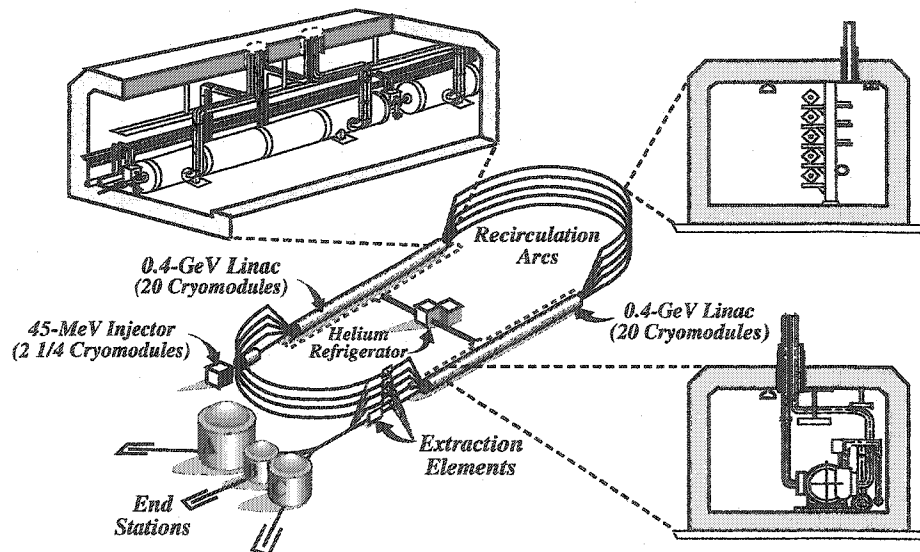


Figure 2-1: CEBAF Accelerator. In the right upper corner blowup shows cross section of five recirculating arcs in the tunnel. In the right lower corner the cross section of a cryomodule. In the upper left corner the linac cryomodules cross section is shown.

## 2.2 CLAS Detector

The main setup of Hall B is the CEBAF Large Acceptance Spectrometer (CLAS). CLAS, is a nearly  $4\pi$  detector (shown in Figure 2-2) based on a superconducting toroidal magnet (TORUS).

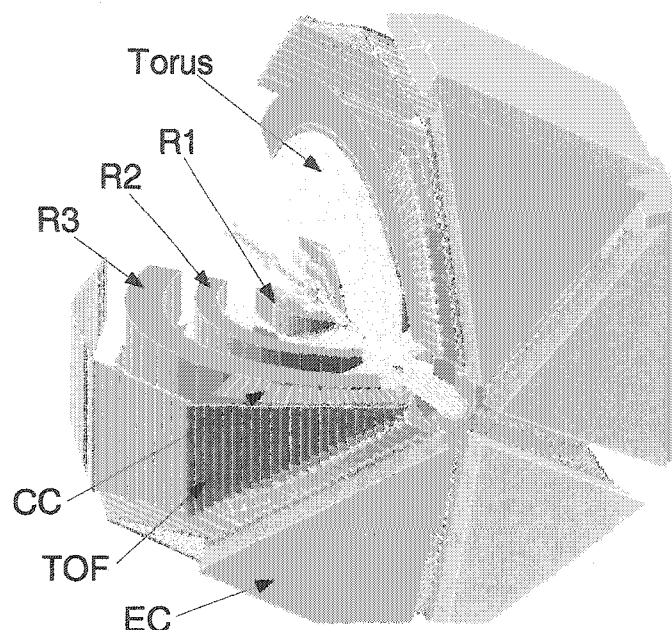


Figure 2-2: Three dimensional view of CLAS detector.

The detector package consists of drift chambers (DC) for measuring trajectory of a particle, gas Čerenkov counters (CC) for electron identification, scintillator counters (SC) for time-of-flight measurements, and electromagnetic calorimeters (EC) for identifying electrons, photons and neutrons. It allows detection of charged particles from  $8^\circ$  to  $140^\circ$  in the laboratory frame, and detection of neutral particles from  $\sim 8^\circ$  to  $\sim 60^\circ$ . A target is located inside the detector on the beam axis. The total charge of the beam passing through the target is measured by a Faraday Cup (FC) located at the end of the beam line. The magnetic field of the spectrometer is provided by six superconducting coils, symmetrically located around the beam axis at  $60^\circ$  intervals (see Figure 2-3), which produce a toroidal field in the azimuthal direction. The maximum intensity of the field provided by the superconducting coils is 2 Tesla in the forward region. The advantage of the toroidal magnetic field is that it is nearly constant in the azimuthal direction, hence bending charged particles only in the

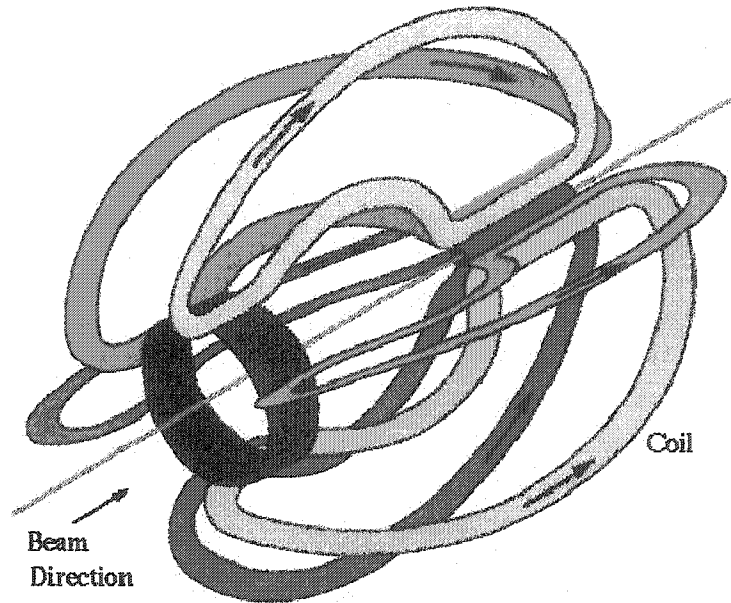


Figure 2-3: CLAS toroidal magnet.

polar direction.

The gaps between the cryostats are filled with six individually instrumented detector packages, which form six independent magnetic spectrometers. This makes a good basis for carrying out experiments that require two or more particles in coincidence in the final state, with 1/1000 or better signal to background ratio at luminosities up to  $2 \times 10^{34} \text{ cm}^{-2} \text{ sec}^{-1}$ .

### 2.2.1 Drift Chambers

The toroidal magnet of CLAS bends particles toward or away from the beam axis leaving the azimuthal angle practically unchanged. The Drift Chambers (DC) are then used to measure the trajectories of charged particles, and determine their momenta. The drift chambers cover a range from  $8^\circ$  to  $140^\circ$  in polar angle and an average of 80% of the azimuthal range. In each sector there are three regions of DC (Figure 2-2). The first region

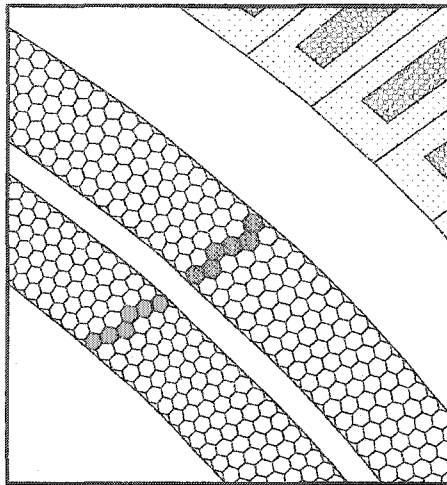


Figure 2-4: Layout of super-layers in Region 3. The sense wires are located in the center of each cell, while the field wires are located in the vertices of the hexagons. The shadowed hexagons represent the cells containing the sense wires which produced a signal for a representative track.

(*R1*) is located nearest to the beam line in a nearly field-free region, and is used to determine the initial direction of the charged particle. The second region (*R2*) is located between the Torus coils in a strong magnetic field, and is used to obtain measurements of the track where the curvature is maximum. The third (*R3*) region is located outside of the coils, where the magnetic field is low, and measures the final direction of the charged particles heading towards the Time-of-Flight counters (TOF), Čerenkov counter (CC) and Electromagnetic Calorimeter (EC).

Each region of the Drift Chambers consists of two Super-layers: one axial, where the wires are strung parallel to the magnetic field lines, and one stereo, where the wires are strung at  $6^\circ$  with respect to the axial wires. This design provides accurate measurement of the polar angle  $\theta$  and the azimuthal angle  $\phi$  of the charged particles. Each super-layer consists of 6 layers of sense wires (4 layers in the case of Region 1 Stereo). Each sense wire is surrounded by 6 shared field wires, which form a hexagonal shape pattern (see Figure 2-4).

The hexagonal shape of the cells provides a good approximation to the circular cell in which the time/drift relation is independent of the particle's entrance angle.

The drift chambers are filled with a mixture of 9/10 Ar (Argon) and 1/10  $CO_2$ , which provides a drift velocity of up to  $0.04 \text{ m}/\mu\text{sec}$  and an operating voltage plateau of several hundred volts. The average efficiency to detect particle tracks for each layer is greater than 98% [22].

In the reconstruction stage, the hits from each super-layer are grouped to form a track segment. Track segments from different super-layers are then linked together to form a track. This gives a momentum from 3 – 5% of its true value. Then, the start time from scintillator counters is used to obtain the drift time, which is converted into a distance from the center of the cell. This then allows for a more accurate fit which includes not only the center of the wire but also includes the distance from this center to the track. This final fit allows for a computed momentum that has a resolution of 0.4% and a track reconstruction efficiency greater than 95%. The overall efficiency of drift chambers is  $> 95\%$  for a hit occupancy of up to 4% and the momentum resolution ( $\sigma$ ) is better than 0.4% [22].

### 2.2.2 Čerenkov Counters

The Čerenkov counter is used to separate electrons from pions and other charged particles [23]. CLAS is equipped with threshold Čerenkov counters in the forward region in every sector covering polar angles up to  $\theta = 45^\circ$ . In electroproduction experiments it is essential to have clean electron-pion separation at the trigger level, since the primary background is due to pions. For inclusive cross section measurements it is important to have fewer than 1 in 100 electron triggers coming from mis-identified pions. With a typical rejection factor of 100 : 1, the Čerenkov counters can ensure this when the number of  $\pi^-$  to the number

of  $e^-$  is less than 1 ( $N_{\pi^-}/N_{e^-} < 1$ ). The radiator gas used in the Čerenkov detector is

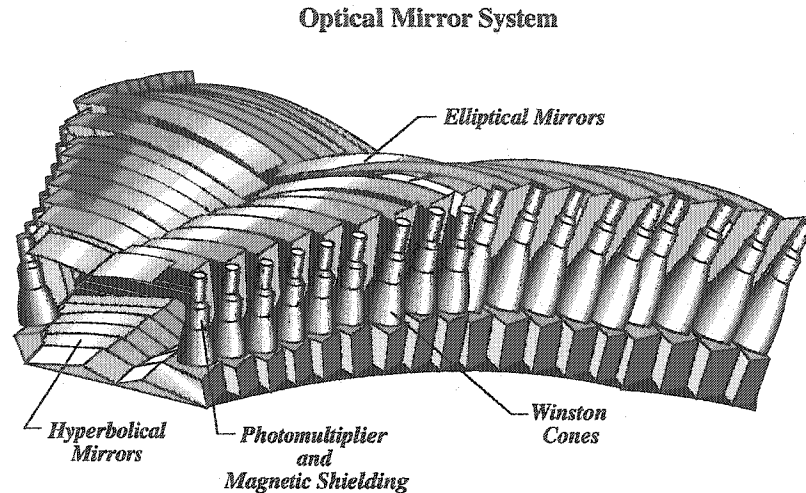


Figure 2-5: Arrangement of the CC optical modules of one sector.

perfluorobutane ( $C_4F_{10}$ ) with index of refraction 1.00153, which results in high photon yield and a pion momentum threshold of  $2.5 \text{ GeV}/c$  [24]. The Čerenkov counter in each sector of CLAS consists of two parts, each consisting of 18 optical modules (Figure 2-5).

Each of the modules is equipped with elliptical, hyperbolic and cylindrical mirrors, to direct the light into the light collection cone with the PMT attached to the end of it (Figure 2-6). The components of Čerenkov counters are mounted on a triangular shaped aluminium frame and protected with a 0.08 mm Tedlar PVF film sandwiched around a sheet of mylar. The PMTs are mounted in the region obscured by the torus so that they do not increase the material in the path of particles passing through CLAS. The gain of the PMTs of the Čerenkov counters are equalized by single-photoelectron response of the photomultiplier. An electron, traveling through the active volume of the detector, typically produces 4 – 5 photoelectrons. The efficiency of Čerenkov counters is better than 98% in the fiducial active detection region [25].

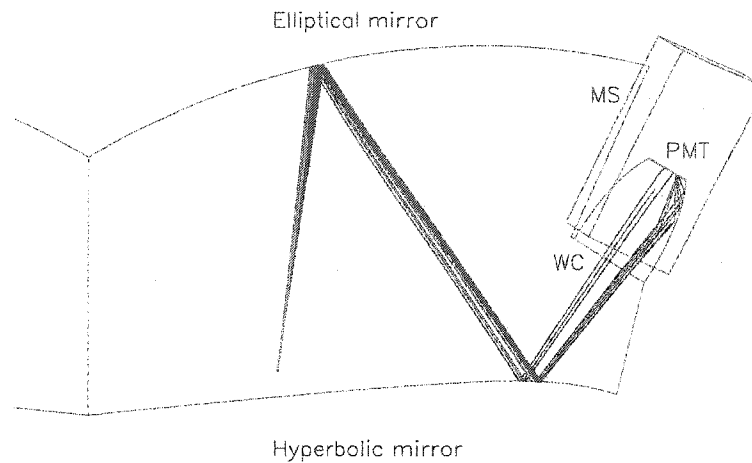


Figure 2-6: One optical module of CLAS Čerenkov counter, showing the detector components and the hypothetical light paths from electrons. Čerenkov light from electrons reflected twice from the mirrors into the Winston Cone (WC), surrounded by the magnetic shield (MS). The Winston cones are used to collect the light onto the surface of the Photo-multipliers (PMT).

### 2.2.3 Scintillation Counters

Charged particle identification in CLAS is done using the momentum measured in DC and the time-of-flight (TOF) measured in the scintillation counters [26]. The TOF counters cover the polar angular range between  $8^\circ$  and  $142^\circ$  and the entire active range of azimuthal angle  $\phi$ , and are located behind the drift chambers (see Figure 2-2). Each sector of TOF consists of 57 scintillators (Bicron BC-408) aligned perpendicular to the beam direction, each covering an approximate scattering angle of  $1.5^\circ$ . The first 23 and last 4 counters have width of 15 cm, and 22 cm for the remaining strips. The widths were chosen to optimize the timing resolution of a single counter and still have sufficient granularity for the triggering process. The scintillator thickness of 5.08 cm is uniform throughout, chosen to give a large signal for traversing minimum-ionizing particles. Each of the TOF counters (“paddles”) has one PMT at each end (shown on Figure 2-7). The last 18 counters in each sector, covering the back angles, are paired into 9 logical counters, so that there are 48

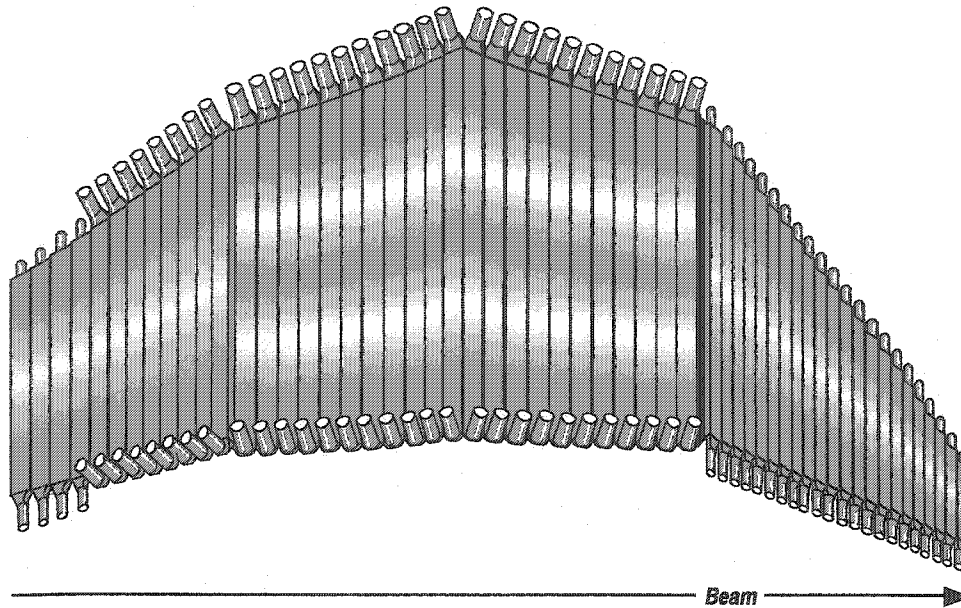


Figure 2-7: TOF system for one sector. The length, the width and the readout configurations are different for different paddles.

logical counters per sector. The timing resolution of a single counter depends on its length and width, with a resolution of about  $130 \text{ ps}$  for the forward counters, and about  $300 \text{ ps}$  for the back counters (with  $\theta > 90^\circ$ ), providing pion-proton separation up to  $2.5 \text{ GeV}$ .

#### 2.2.4 Forward Electromagnetic Calorimeter

The forward region of all six sectors of the CLAS detector are equipped with an Electromagnetic Calorimeter (EC) of 16 radiation lengths, covering a polar angle in the range  $8^\circ < \theta < 45^\circ$  [27]. In two of the sectors this coverage is extended up to  $60^\circ$  by the Large Angle Calorimeters (LAC). The Electromagnetic Calorimeter has a lead-scintillator sandwich design consisting of alternating layers of scintillator strips and lead sheets, with a lead/scintillator ratio of 0.21, resulting in 39 cm of scintillator and 8.4 cm of lead per module. With this ratio, approximately  $1/3$  of the energy is deposited in the scintillators.

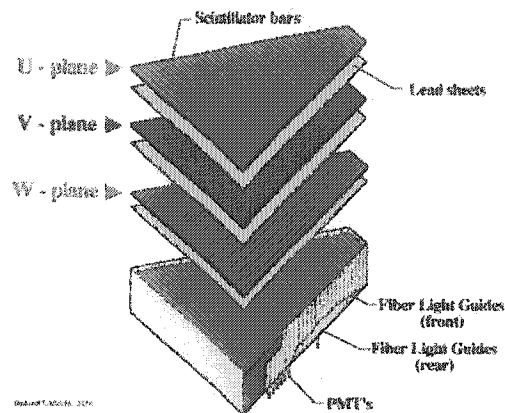


Figure 2-8: CLAS Forward Electromagnetic Calorimeter exploded view of one of the sectors.

The EC has a triangular shape and is composed of 39 layers of BC412 scintillator of 10 mm thick, with 2.2 mm Pb sheets in-between. Each layer is composed of 36 scintillator strips parallel with one side of the triangle (see Figure 2-8), the orientation changing by approximately  $120^\circ$  between two adjacent layers. The three orientations, called views, are labeled U, V and W, each containing 13 layers. This design provides stereo information on the hit position. The entire detector is subdivided into inner and outer parts, containing 5 and 8 layers for each view, respectively. This provides longitudinal sampling of the shower for improved hadron identification. The readout scheme can be seen in Figure 2-9. The EC in total consists of 8424 scintillator strips and 1296 photo-multipliers. The two Large Angle Calorimeters are implemented only in sectors 1 and 2 (see Figure 2-2). They consist of 33 layers, each composed of a 0.2 cm thick lead foil and of 10 cm wide and 1.5 cm thick NE110A scintillator strips. The layers form a  $40 \times 24$  matrix with cell size  $10 \times 10 \text{ cm}^2$ ,

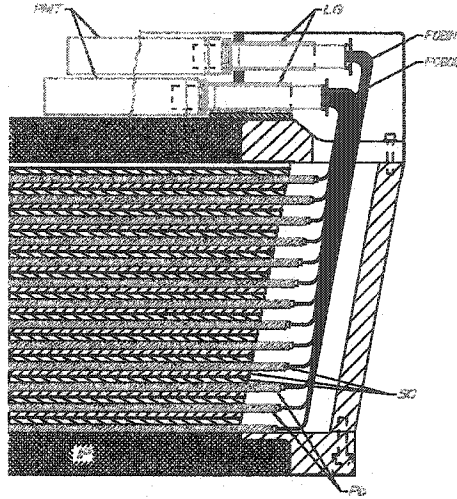


Figure 2-9: Electromagnetic Calorimeter readout scheme. PMT - photomultiplier, LG - Light Guide, FOBIN - Fiber Optic Bundle Inner, FOBOU - Fiber Optic Bundle Outer, SC - Scintillators, Pb - 2.2 mm Lead Sheets, IP - Inner Plane (Composed of two 1.905 mm Stainless Steel Face Sheets and 72.2 mm Foam Core Plate)

and each consecutive layer is rotated by  $90^\circ$ . Each module of the LAC is divided into inner and outer parts providing better electron/pion discrimination. To avoid optical cross over each pair of contiguous scintillators are separated by Teflon strips of 0.2 mm thickness, and another layer of Teflon (0.2 mm thick) is inserted between lead foils and scintillators. The module thickness corresponds to 12.9 radiation lengths. The Electromagnetic Calorimeter's features are summarized below:

- Fast total energy sum for triggering ( $< 100$  ns)
- $e/\gamma$  energy resolution  $\sigma/E \leq \sqrt{E(\text{GeV})}$
- position resolution of  $\delta r \approx 2$  cm at 1 GeV
- $e/\pi$  rejection  $> 99\%$  at energies greater than 1 GeV
- Mass resolution for two-photon decay of  $\delta m/m \leq 0.5$  GeV

- Neutron detection efficiency greater than 50% for  $E_n > 0.5 \text{ GeV}$
- Time-of-flight resolution around  $0.4 \text{ ns}$

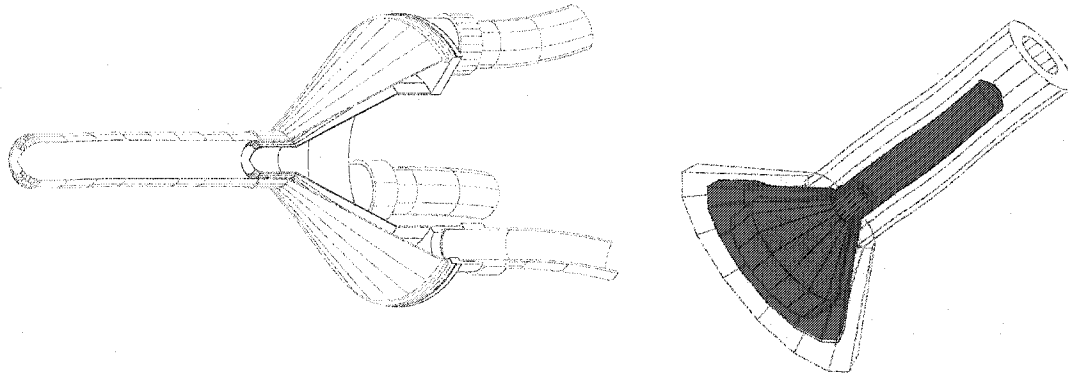


Figure 2-10: Engineering drawings (CAD) of CLAS cryogenic target cell on (the left) and GSIM image of the target used in simulations.

### 2.3 Liquid Hydrogen Target

The experiment measures electron scattering on an unpolarized proton. As a source of protons a liquid hydrogen target is used. The hydrogen is maintained in a liquid state using an aluminium cell (see Figure 2-10) at a temperature of  $\sim 20 \text{ K}$ . The target cell has a cylindrical shape with  $5 \text{ mm}$  diameter and  $15 \mu\text{m}$  thick input and output windows. The liquid hydrogen is circulated through the system of pipes, shown on Figure 2-10 [28]. During the experiment the target parameters such as temperature and pressure are monitored and stored in the database.

## 2.4 Trigger System and Data Acquisition

The triggering system is designed to select events of interest and reject the background. In CLAS there are two levels of trigger. The first level trigger (Level-1) is used to identify possible event candidates. Most electroproduction experiments in CLAS require the scattered electron to be detected. The Level-1 trigger serves the purpose to select events with a possible electron in the detector and triggers the data acquisition system to record the event, which will be further analyzed. The Level-1 trigger uses information from the pretrigger boards of the EC, CC and TOF (in case of e1d experiment, only EC and CC were used in the trigger) to form a coincidence signal which is sent to a Read-Out-Controller (ROCs). This level only ensures that there was sufficient energy deposited in the electromagnetic calorimeter and there was a signal in the Čerenkov counter (EC and CC are in coincidence for each sector separately). To improve the event/background ratio even more the Level-2 trigger was implemented in CLAS, which identifies possible track candidates in the drift chambers. The Level-2 trigger reads information from the Drift Chamber wires and searches for track segments. In the “e1d” experiment the Level-1 trigger was used in coincidence with Level-2. The CLAS data acquisition (DAQ) system was designed for an event rate of 2 *kHz*. Continued development of the DAQ system has resulted in operation at event rates of 3 – 4 *kHz*. The data output rate limit at present is 25 *MBytes/s*, constrained by the speed of the RAID disks that store the data. The DAQ consists of 17 Read-Out-Controllers (ROCs) communicating with a Trigger Supervisor board which make the decision whether the event should be read out. If there is a trigger the data signals are read out, and sent to the Event Builder (EB) process, which forms a complete event by putting together data from different parts of the detector and stores it in the Data Distribution (DD) ring. The

Data Distribution ring is a shared memory which allows more than one process to access the event for writing it out and analyzing at the same time. The Event Recorder (ER) process writes data from the DD ring to the RAIDs (Redundant Array of Inexpensive Disks). The data from the RAIDs are later transferred to a tape SILO for permanent storage. The schematics of the DAQ is shown in Figure 2-11([29]). Some subset of events from the DD ring are constantly being processed to monitor data quality and identify problems. The status of detector components are constantly monitored during the experiment and stored in the database for offline analysis.

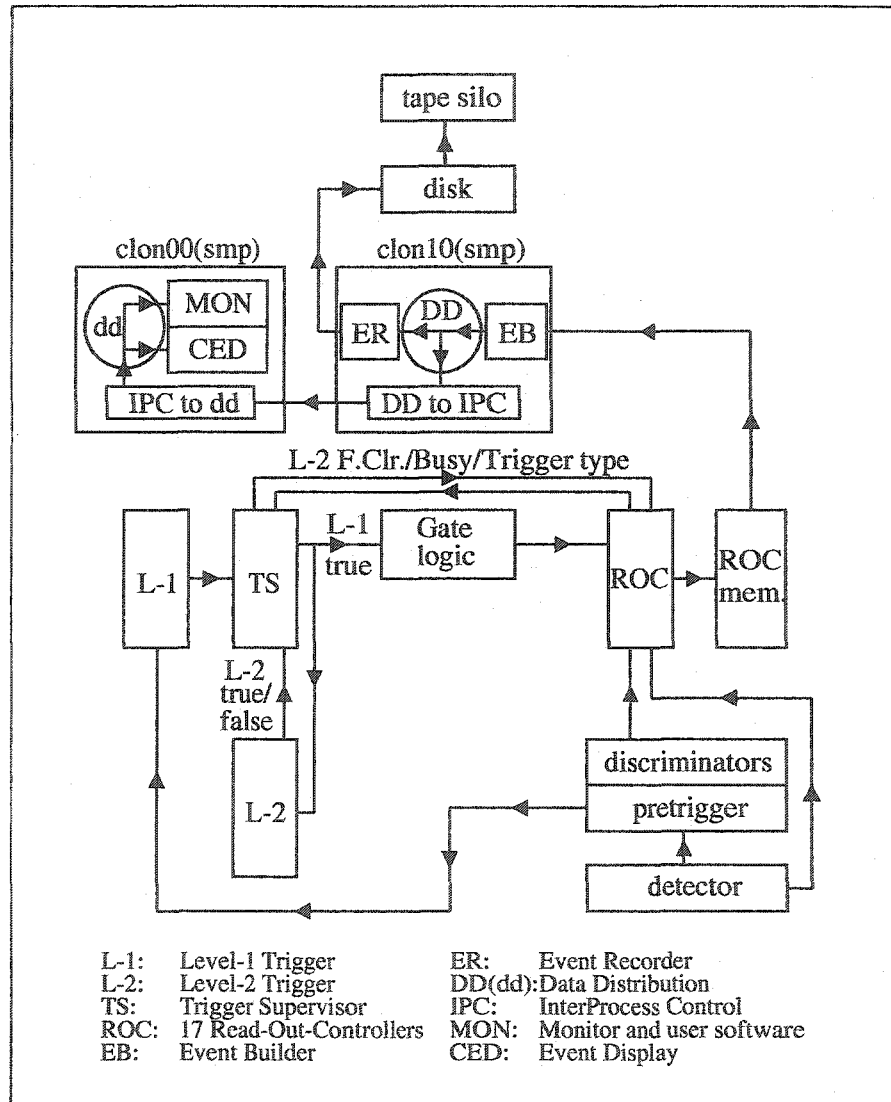


Figure 2-11: CLAS Data Acquisition System schematic view. The signals from the detector go to the ROCs and pretriggers. The pretriggers initiate the readout from the particular detector system as well as provide an input for the Level-1 trigger. In case of present trigger the data signals are read out, digitized and transferred to a process called Event Builder (EB) running on the main computer clon10 and are temporarily stored in the Data Distribution (DD) ring in shared memory. A process called the Event Recorder (ER) writes data from the DD ring onto disks from where they are transferred to the tape silo. Some of the events from the DD ring on clon10 are transferred to a different computer clon00 to be used as an input stream for monitoring programs.

## CHAPTER 3

# DATA CALIBRATION AND PROCESSING

The experiment presented here was carried out during 03-*Feb*-2000 to 02-*Mar*-2000. It measured electroproduction on a liquid hydrogen target. The data from the experiment are saved in separate files for each run containing  $\sim 500k$  *Events* (each run contains  $\sim 10M$  *Events*), this limitation comes from the fact that files are limited to a size of 2 *GBytes*. The RAW data are saved in BOS format. For analysis these files are processed by the offline reconstruction program (RECSIS [30]) in order to identify particles in the events (the process of reconstruction is referred to as “cooking”). Part of the data are processed to calibrate the various detector components in order to achieve the optimum resolution from each detector element. After this, all data are processed to generate the final 4-momentum vectors.

### 3.1 Data Processing

The data are “cooked” using the RECSIS offline reconstruction program. The program consists of software modules for each detector, designed to reconstruct hits from the RAW

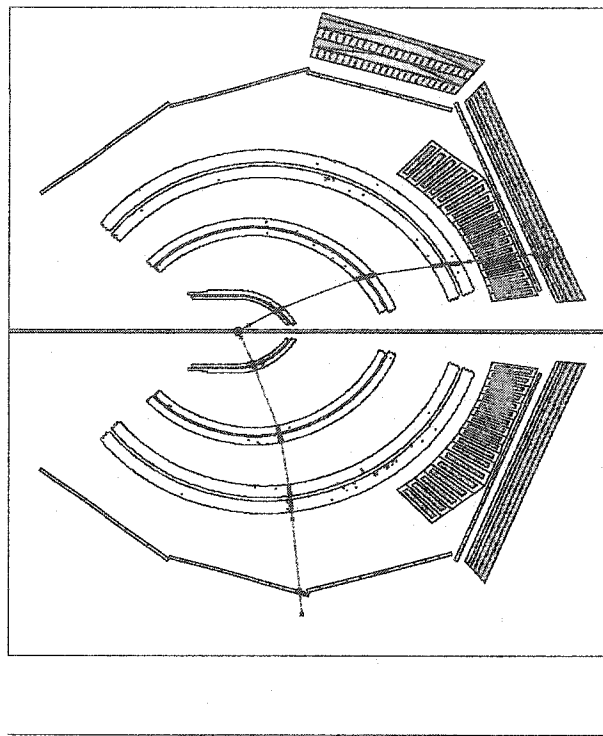


Figure 3-1: An example of an event reconstructed by RECSIS. The in-bending track on the top half of the detector corresponds to an electron that triggered the event, the out-bending track in the lower half corresponds to a positively charged particle.

data. First, each detector package reconstructs hits in the detector based on raw ADC and TDC information, and stores the results of the hits in intermediate banks (BOS Banks [31]). Then the output from all detectors are passed to the event builder module (SEB) which combines the different detector hits to identify individual particles in the event, and produces an output containing the events that will be used for further analysis. The main goals of SEB are [32]:

- geometrically match the tracks and hits.
- identify the trigger particle.
- calculate the trigger time.

- define particle identification (PID).
- build an event and write it to output.

The information on reconstructed hist and tracks is read from the so-called “intermediate” BOS banks, after which geometrical matching is done. The concept of geometrical matching is to define distances between the detector hit position ( $r_i$ ) and the position on the detector plane ( $r_{pl}$ ) defined by a track. For each hit the squared sum of the difference between the coordinates of the track and the detector hit is divided by the error of the coordinates:

$$C_i^2 = \sum_{i=x}^z \frac{(r_{pl} - r_i)^2}{\sigma_{r_i}^2} \quad (3.1)$$

where  $i$  runs over the  $x, y$  and  $z$  coordinates for a given detector, and  $\sigma_{r_i}$  is the error for this coordinate. The hit with minimum  $C_i$  is taken as a match. First the matching is done for all charged tracks, reconstructed in an event, then the remaining hits in the Electromagnetic Calorimeter that were not associated with any track, are considered as candidates for neutral particles. Next, the trigger particle is identified, for which it is required to have a negative track and a showering hit in the EC. From all the possible candidates the one is chosen that is best matched to an electron candidate.

The time of the interaction in the target (vertex time) is defined as:

$$t_{tr} = t_{det} - \frac{R_{det}}{\beta c} \quad (3.2)$$

where  $t_{det}$  is the time for trigger particle measured by the detector,  $R_{det}$  is the path length of the particle (determined in the track reconstruction module), and  $\beta = P_{trk} / \sqrt{P_{trk}^2 + m_e^2}$  ( $P_{trk}$  is the particle momentum). If the trigger particle is found then SEB constructs

a logical structure for storing particle information. An example of SEB hit matching is shown in Figure 3-1. After defining the trigger particle and calculating the trigger time,  $\beta$  is calculated for each of the remaining particle candidate based on the detector measured time and path length from the target to the detector:

$$\beta = \frac{R_{trk}}{(t_{det} - t_{trk}) \cdot c} \quad (3.3)$$

The charged particles are then identified using a cut on  $\beta$ . For the neutral particles the  $\beta$  is calculated from the time measured by the EC, and is used to distinguish between photons and neutrons. If  $\beta$  is within 5% of 1 then the particle is marked as a photon, otherwise it is marked as a neutron.

## 3.2 TOF Calibration

The time-of-flight counters are essential components of the CLAS detector. In combination with the reconstructed particle momentum they are used to identify charged particles. The quality of particle identification depends primarily on the measurement of  $\beta$ , which depends on TOF, therefore a big effort is devoted to TOF calibration. The TOF calibration consists of several steps: (1) the calibration of individual TDC and ADC channels, (2) the left-right PMT alignment, (3) the attenuation length calibration and (4) the counter-to-counter calibration. In the following sections, these steps are described in some details.

### 3.2.1 Pedestal and TDC calibration

The pedestals of the Analog-to-Digital Converter (ADC) is the channel where an effective zero measurement would fall. It depends on the level of noise in all the components hooked

up to the ADC. These pedestals were measured by taking runs with random triggers. These data are analyzed and saved in the calibration database.

The Time-to-Digital Converter (TDC) was calibrated using runs taken with a special DAQ configuration. Every counter in the TOF system was pulsed with a laser and the response of each TDC was analyzed for various delays between “START” and “STOP” signals. The actual time was parametrized in terms of the measured TDC time as:

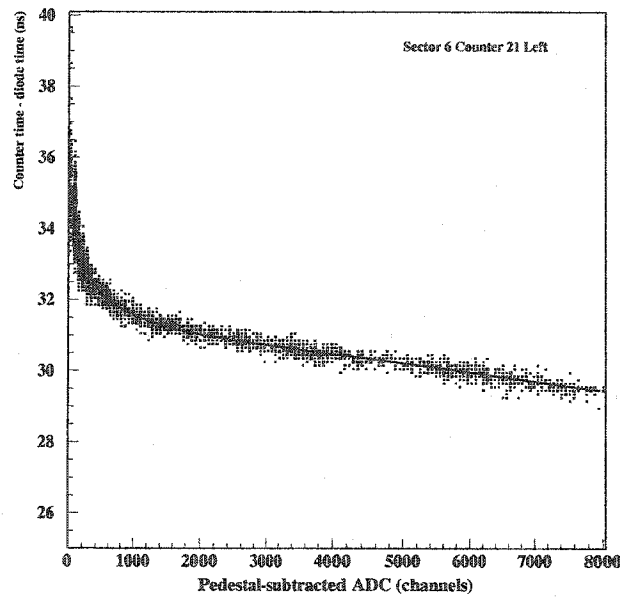


Figure 3-2: Typical distribution of TDC time (channels) versus pulse height (ADC channels). The fitted function  $f_w$  (parametrization of  $f_w$  is given by Eq.(3.6)) used in time-walk corrections Eq.(3.5).

$$t = c_0 + c_1 T + c_2 T^2 \quad (3.4)$$

The constants  $c_1$  and  $c_2$  are saved in the calibration database. The parameter  $c_0$  is not relevant, since the left-right calibration is subsequently performed to equalize the left-right difference for each counter.

### 3.2.2 Time Walk Correction

The time-walk corrections were done using data obtained with a laser pulse run. The amount of light delivered to each counter was varied, and the pulse height and signal time were measured for pulses with different amplitudes to obtain the pulse height to time dependence. The time-walk correction is done in the software using the following relation:

$$t_w = t - f_w \frac{(A - P)}{V_T} + f_w \frac{600}{V_T} \quad (3.5)$$

where  $V_T$  is the TDC channel corresponding to the leading-edge discriminator threshold of 20 mV ( $\sim 35$  channels),  $A$  is the corresponding ADC channel,  $P$  is the pedestal of the ADC channel, and  $f_w$  is the time walk correction function shown on Figure 3-2. The parametrization of  $f_w$  contains three parameters ( $a$ ,  $b$  and  $c$ ). These parameters are determined for each PMT separately using the laser calibration runs. The rapidly changing function (see Figure 3-2) is parametrized by:

$$f_w(x) = \frac{b}{x^c}, \quad \text{for } x < a$$

$$f_w(x) = \frac{b}{a^c}(1 + c) - \frac{bc}{a^{c+1}}x, \quad \text{for } x > a \quad (3.6)$$

The fit parameters  $a$ ,  $b$  and  $c$  are saved in the calibration database for offline software corrections.

### 3.2.3 Left-Right PMT Alignment

The position of the hit in the TOF counter is determined by the time delay between the left and right PMT. Therefore the offset between the left and right counter must be determined

**gavalian (129.57.16.57)**

**JLab Printing Info:**

**<http://cc/services/printing>**

to provide an accurate measurement of the position. For each counter the quantity:

$$l = LEFT_{TDC} - RIGH_{TDC} \quad (3.7)$$

should be centered around zero. If this is not the case, the offset of  $\Delta t$  is added to this value, defined as:

$$\Delta t = \frac{l}{v_{eff}} \quad (3.8)$$

where  $v_{eff}$  is the effective velocity of the light in the TOF counter. The effective velocity is calculated using hit position information provided by tracking:

$$y = v_{eff} \frac{(t_L - t_R - t_{off})}{2} \quad (3.9)$$

The dependence of the distribution  $t_L - t_R$  versus  $y$  for each counter is fitted with a linear function to determine the constants  $t_{off}$  and  $v_{eff}$ . The offsets ( $\Delta t$ ) are saved in the calibration database for offline time corrections.

### 3.2.4 Energy Calibration

The time-of-flight system also serves for proton-pion separation without using timing information. At relatively low particle momentum, the separation of protons from pions can be accomplished using information of the deposited energy in the scintillators. The dependence of the deposited energy ( $\delta E/\delta x$ ) on the particle momentum is different for protons and pions. The ADC pulse heights are normalized using the energy deposited in the scintillators

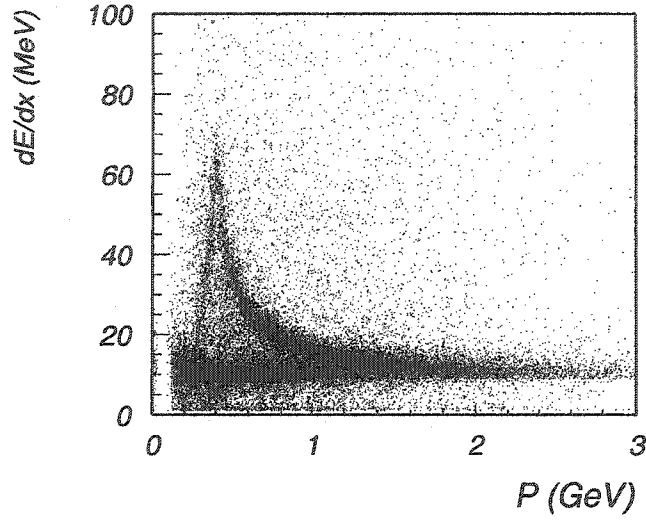


Figure 3-3: Energy deposited in the TOF scintillators by hadrons versus hadron momentum after MIP calibration is done. Pion and proton bands are clearly distinguishable.

by minimum ionizing particles [33]:

$$A_L = \frac{N_L}{k} \exp\left(-\frac{L/2 - y}{\lambda}\right), \quad A_R = \frac{N_R}{k} \exp\left(-\frac{L/2 + y}{\lambda}\right) \quad (3.10)$$

where  $A_L$  and  $A_R$  are the ADC channels (pedestal subtracted),  $N_L$  ( $N_R$ ) is the peak height of the Left (Right) PMT when the minimum ionizing particle passes through the center of the scintillator,  $L$  is the scintillation counter length,  $y$  is the distance of the hit measured from the center of the counter. Then the energy is found by calculating the geometrical mean from the Left and Right ADC channels [34]:

$$\bar{A}_g = \sqrt{A_L A_R} = \alpha E_d \exp\left(-\frac{L}{2\lambda}\right) \quad (3.11)$$

where  $\alpha = (N_L N_R)^{-1/2}/k$ , and  $E_d$  is a position-invariant measure of the deposited energy.

The energy calibration is performed using minimum ionizing pions. The timing information

from scintillator counters is used to select the pions, therefore the method requires reasonable timing calibration. In Figure 3-3 the deposited energy ( $\delta E/\delta x$ ) of hadrons versus hadron momentum is plotted after energy calibration. At low energies, protons and pions can be well separated. At higher momentum, starting from  $0.8 \text{ GeV}/c$ , as protons become minimum ionizing, the two bands start to merge. This method of pion identification is not used in standard data analysis, its main purpose is to provide a reasonably clean sample of pions for further calibration.

### 3.2.5 RF and Paddle-to-Paddle calibration

Once all individual scintillator paddles have been calibrated, it is important to obtain constants for offline correction of the delays of paddles to the same reference frame. The time of the hit in the counter is calculated as:

$$T_{SC} = \frac{T_{Left} + T_{Right}}{2} - \frac{V_{right} - V_{left}}{2V_{right}V_{left}}y \quad (3.12)$$

where  $T_{Left}$  ( $T_{Right}$ ) is the time measured by the Left (Right) PMT,  $y$  is the hit position, and  $V_{left}$  ( $V_{right}$ ) is the speed of the light propagation toward the left (right) PMT. First, timing of each scintillating counter is aligned to the timing of the accelerator's RF-signal. The difference between the event start time and RF time is calculated as:

$$\Delta\tau = T_{SC} - T_{flight} - T_{RF} \quad (3.13)$$

where  $T_{flight}$  is the time of flight of the particle, calculated from the information provided by tracking (using the path length the particle has traveled and assumption that  $\beta = 1$  for electron candidates),  $T_{RF}$  is the time of the RF-signal.

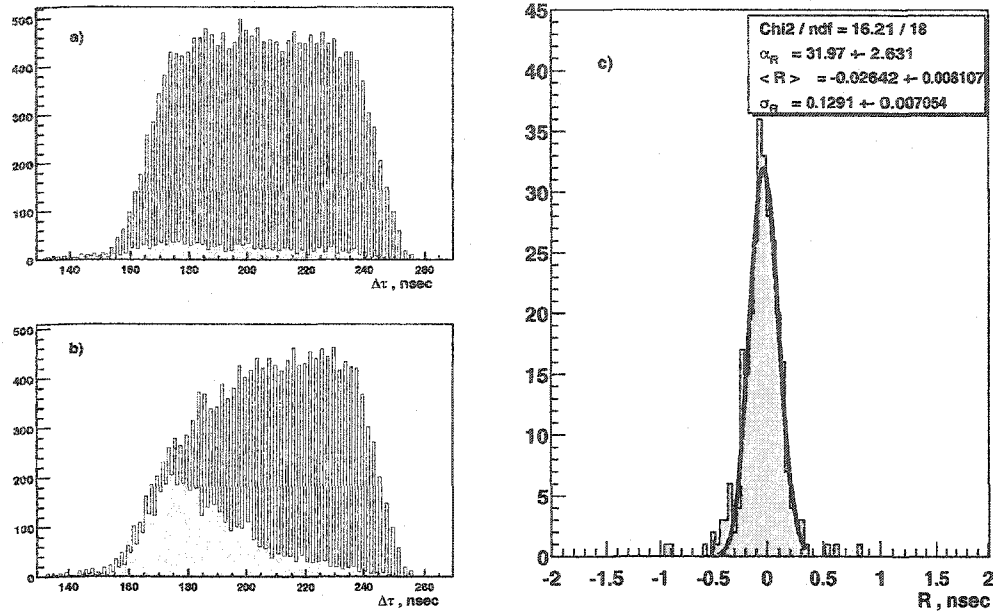


Figure 3-4: Illustration of the beam RF-structure: a)  $\Delta\tau$  distribution with properly calibrated TDCs, b)  $\Delta\tau$  distribution when the  $c_1$  parameter of the TDC of the RF-signal is mis-calibrated by less than 1%, c) R-distribution (described in Eq.(3.15)) for a single scintillator channel, fit to a Gaussian.

The RF-signal is provided by the accelerator. This signal is generated with each electron bunch (length of the bunches are  $\sim 2ps$ , and distance between the bunches  $\sim 2ns$ ) with frequency  $\nu = 1.4971 GHz$  in the injector. The RF-signal is sent to all three experimental halls with a prescale factor of 40. The bunches delivered to each hall are separated by time intervals of:

$$\Delta T = \frac{3}{\nu} = \frac{3}{1.4971 GHz} = 2.0039 ns \quad (3.14)$$

where  $\nu$  is the accelerator frequency, and the factor 3 appears because the beam from the injector is shared among three experimental halls. In Figure 3-4 (a) the quantity  $\Delta\tau$  is plotted for a single channel. The multiple peaks on the plot arise from the 40 prescale factor of RF-signal. If the TOF and RF-signal TDCs are well calibrated the peaks in the plot should be separated by exactly  $\Delta T$  (2.0039 ns). This plot is also sensitive to the TDC

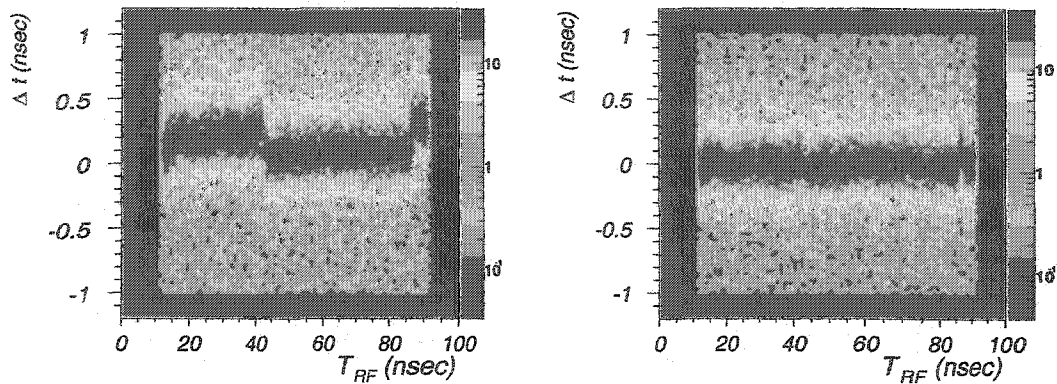


Figure 3-5: Two dimensional plot of  $R$  versus  $t_{rf}$  distribution for a) uncalibrated RF-signal and b) calibrated RF-signal.

calibrations described in section 3.2.1. If the TDC was not calibrated well it may cause a pattern similar to the one shown in Figure 3-4 (b).

For each scintillator counter the time-offset is calculated as [35]:

$$R = \text{mod}(T_{SC} - T_{flight} - T_{RF} + 100 \cdot \Delta T, \Delta T) - \frac{\Delta T}{2} \quad (3.15)$$

where  $\Delta T$  is defined in Eq.(3.14). This quantity defines the time delay for the particular scintillation counter with respect to the RF-signal. In Figure 3-4 c) the time delay ( $R$ ) can be seen for one counter. This value must be subtracted from the measured time by the scintillation counter when calculating the mass of the particle. The resolution depends on timing characteristics of the scintillator, the quality of the calibration of TDCs, and the calibration of the RF-signal. The TDCs of the RF-signal have a slope which needs to be calibrated before calibrating the scintillation counters with respect to the RF-signal. The procedure of RF-signal calibration is described in [36]. In Figure 3-5 (a) the time delay ( $R$ ) is plotted versus  $T_{RF}$  if the RF-signal is not calibrated, and (b) shows the same

dependence after calibration. Once the RF-signal has been calibrated the  $R$  (given by Eq.(3.15)) for each counter is fitted to find the mean value (the shift from zero). These constants, called “fine tuning constants”, are saved in the database, and the time measured by a particular scintillation counter will be corrected with the corresponding time delay constant in software. Since electrons are mainly produced in the forward direction, to calibrate backward counters pions are used. In case of pions the time of flight is calculated using the tracking information.

### 3.2.6 Crude Tuning

After all scintillator counters have been calibrated relative to the RF-signal, there still might be an offset between different counters, because the counters might be aligned with the RF-signal corresponding to different electron bunch. In this case the time difference between different scintillator counters should be multiple of  $2.0039 \text{ ns}$ . The procedure described in [35], called “crude tuning”, is used to resolve this ambiguity by using events with an electron and at least one pion in the final state. First the time delays for the first ten paddles in each sector are equalized. Then events with an electron in the first ten counters and a pion in the sector next to the sector opposite of the electron sector are selected. The reason for not using the opposite sector is possible contamination from elastic events with a proton mis-identified as a pion. The electron and pion vertex time difference is a multiple of  $2.0039 \text{ ns}$ , and is defined as:

$$\delta t_{\text{ort}} = (T_{SC}^e - T_{\text{flight}}^e - T_{FT}^e - R^e) - (T_{SC}^\pi - T_{\text{flight}}^\pi - T_{FT}^\pi - R^\pi) \quad (3.16)$$

where  $T_{SC}^e$  ( $T_{SC}^\pi$ ) is the time measured by the scintillator counter for the electron (pion),

$T_{flight}^e$  ( $T_{flight}^\pi$ ) is the time of flight of the electron (pion), and  $T_{FT}^e$  ( $T_{FT}^\pi$ ) is the fine tuning constant for the scintillator counter with an electron (pion) hit.  $R^e$  and  $R^\pi$  are the constants, defined by Eq.(3.15) for electron and pion paddles. Figure 3-6 shows example plots for two counters. The bin with the largest number of counts in the plot determines the time offset to be applied to the scintillation counter. After aligning the timing for the first ten counters,

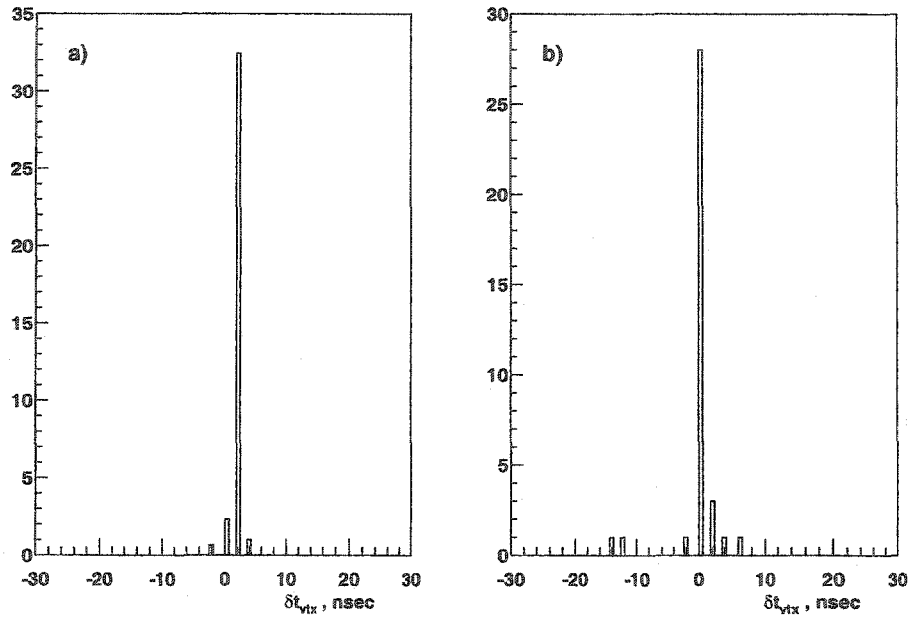


Figure 3-6: Distribution of number of events versus  $\delta t_{vtx}$  defined in Eq.(3.16) for two different counters. On a) the maximum number of events is detected with  $\delta t_{vtx} = 2.0039$  ns time shift. b) the maximum number of events is detected with  $\delta t_{vtx} = 0.0$  ns.

one needs to find the relative delays for the different sectors (which also can be only multiple of 2.0039 ns). For this purpose events are selected with the electron hits in one of the first ten paddles in a sector other than Sector 1, while the pion is in one of the first ten counters in Sector 1. This way all sectors are calibrated with respect to Sector 1. The time difference at the vertex is calculated as:

$$\delta t_{vrt} = (T_{SC}^e - T_{flight}^e - T_{10}^e - T_{FT}^e - R^e) - (T_{SC}^\pi - T_{flight}^\pi - T_{10}^\pi - T_{FT}^\pi - R^\pi) \quad (3.17)$$

where  $T_{10}^i$  ( $i = e, \pi$ ) are the constants obtained in the first step of “crude tuning” (described above). The quantity  $\delta t_{vert}$ , calculated for each sector, is then subtracted from the measured time. Once the first ten counters in all the sectors have been calibrated and the relative time delay of different sectors have been determined, the rest of the counters are calibrated (scintillator paddles from # 11 – 48). Events with an electron in the first ten counters and a pion in one of the backward counters are used for this purpose.

### 3.2.7 Alignment of TOF system to the RF-signal

To determine the mass of hadrons using flight time information, one has to know the start time of the event. The natural choice would be to use the electron time to determine the start time of the event at the vertex. The time of flight of the hadron and its resolution is given by:

$$T_{flight}^h = T_{SC}^h - \left( T_{SC}^e - \frac{L_{track}^e}{\beta c} \right)$$

$$\delta T_{flight}^h = \sqrt{(\delta T_{SC}^h)^2 + (\delta T_{SC}^e)^2 + \left( \frac{\delta L_{track}^e}{\beta c} \right)^2} \quad (3.18)$$

where  $L_{track}^e$  is the length of the electron track from target to the scintillation counter,  $c$  is the speed of light, and  $\beta$  is taken to be equal to 1. The electron timing resolution  $\delta T_{SC}$  makes a significant contribution to the uncertainty of the time-of-flight determination of hadrons. To eliminate the contribution from electron timing errors the RF-signal is used to determine the event start time. After the paddle-to-paddle calibration is complete, the timing of all scintillation counters are adjusted with respect to the same RF bunch. Therefore, the time measured by scintillators for hadrons can be corrected using the RF-signal [37]:

$$T_{flight} = T_{SC}^h - \left( T_{SC}^e - \frac{L_{track}^e}{\beta c} - R^e \right) \quad (3.19)$$

$$\delta T_{flight} = \sqrt{(\delta T_{SC}^h)^2 + \left(\frac{\delta L_{track}^e}{\beta c}\right)^2} \quad (3.20)$$

where  $T_{SC}^h$  is the time measured by the scintillation counter hit by the hadron. Before using Eq.(3.19), all time-of-flight counters must be adjusted with respect to the RF-signal. But because the tuning of the beam can change the path length of the electrons from the injector to the target in the experimental hall, and because the signal propagation speed in the cables may vary with time e.g. due to temperature changes, these adjustments must be done for every run.

### 3.2.8 Calibration Results

The procedures described above were applied to allow the CLAS off-line analysis software to distinguish between different types of hadrons reliably. The timing resolution determined by the Time-of-Flight calibration is very important to reduce non-physical background, and allow the investigation of multi-particle final states using the missing mass technique. The quality of Particle Identification (PID) can be seen in Figure 3-7 (a), where particle velocity  $\beta$  versus the particle momentum is plotted (all scintillation counters combined in this graph). One can identify distinguishable bands for different particles: protons can be clearly separated from kaons and pions up to  $\approx 3.5$  GeV. The mass of particles can be calculated knowing the particle's velocity, measured by the TOF, and the particle momentum, measured by tracking. In Figure 3-7 (b) the mass spectrum is shown for an empty target run at an electron beam energy of 4.4 GeV. Separate peaks corresponding to the pions, kaons, protons and deuterons can be seen. At low momentum the resolution of the TOF system is adequate even for the separation of positrons, pions and muons from pion decays, as can be seen in Figure 3-8. The feasibility of separating these three particles is

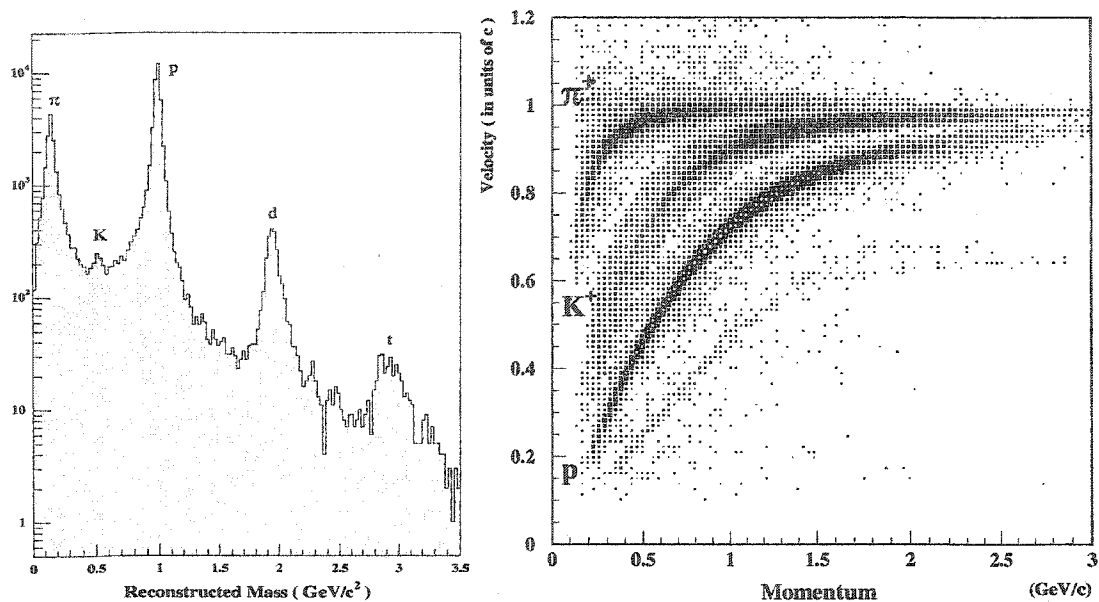


Figure 3-7: The TOF Calibration Results. a) the velocity of positively charged particles versus momentum is plotted. The kaon band is artificially enhanced by preselecting events from data sample with a loose kaon cut. b) Mass spectrum of hadrons calculated from TOF for an empty target run at  $E_0 = 4 \text{ GeV}$  is plotted. Clearly visible peaks correspond to pions, kaons, protons, deuterons and tritons respectively.

strongly momentum dependent. Particles with a momentum  $P < 0.25 \text{ GeV}/c$  and a signal in the scintillation counters above #20 are selected. In Figure 3-8 (a) the mass spectrum of these particles is shown. In 3-8 (b) the mass spectra of these particles are shown with the electron and the other charged particle in registered in the same sector, in order to enhance the positron peak. At higher momenta the resolution of CLAS deteriorates and these peaks merge. For this reason the CLAS off-line particle identification procedure always presumes all these particles to be pions.

### 3.3 Drift Chamber Calibration

The primary purpose of the Drift Chamber calibrations is to refine the accuracy of

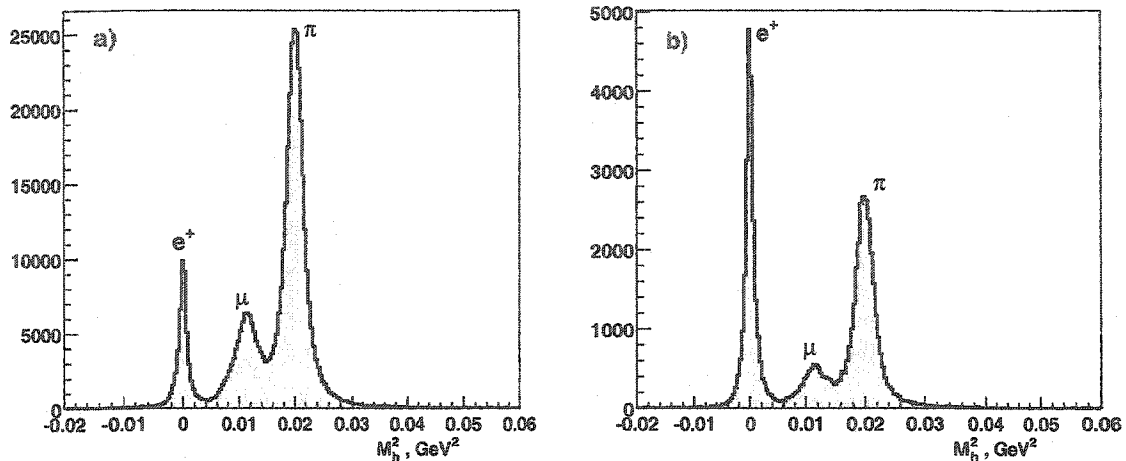


Figure 3-8: Mass squared distribution for backward flying particles with momentum  $P < 0.25 \text{ GeV}$ : a) without any sector cut, b) electron and the other particle are required to be in the same sector.

position measurements from time-based tracking. The constants for the time-to-distance conversion have to be systematically calibrated and checked for stability over the run period. Commonly, runs are chosen from each day of the running period and approximately 100  $K$  events from these runs are used in the calibration. The calibration procedure consists of several iterations of running the reconstruction program followed by refitting the calibration constants. The track reconstruction in the Drift Chambers is done in two stages. In the first stage, individual tracks are fit to the hit wire positions (“hit-based tracking”). In this stage, the hits inside the super-layer are combined into track segments, which are then linked together to form tracks across all three regions. At this stage, due to the comparatively small size of the drift cells and large number of wire layers, the track momenta can be reconstructed with 3 – 5% resolution [22]. In the second stage, the time-of-flight information, obtained from scintillator counters, is used to correct the drift times. Then these drift times are converted to drift distances using pre-determined time-to-distance constants. The corrected hit positions are then used to determine the final track parameters. This last stage is called

time-based-tracking (TBT). The drift time is given by:

$$t_{drift} = t_{start} + t_0 - t_{TDC} - t_{flight} - t_{prop} - t_{walk} \quad (3.21)$$

where  $t_{start}$  is the event start time (determined by TOF),  $t_{TDC}$  is the time measured by the Drift Chamber's TDC,  $t_{flight}$  is the particle flight time from the reaction vertex to the wire,  $t_{prop}$  is the signal propagation time in the wire, and  $t_{walk}$  is a small time-walk correction due to different ionization for slow and fast particles.

### 3.3.1 Drift Chamber Nomenclature

The CLAS drift chamber consists of six identical slices one for each sector. For each sector the chambers are divided into three regions. Each region is a separate physical volume consisting of two super-layers with axial and stereo wires. A schematic view of the Drift Chamber system is shown in Figure 3-9. Each super-layer contains six layers of sense wires (except super-layer 1, which has only 4 layers sense wires), and each super-layer is calibrated separately, yielding 36 sets of calibration constants [38]. When a charged particle goes through the drift chambers, each of the 34 layers is hit <sup>1</sup>. Each hit detected in the chamber is used to determine the particle's track via least squares fit performed in the CLAS reconstruction program. The quantities used to describe the distance of the charged particle track from a sense wire are:

- *DOCA* (Distance Of Closest Approach) is the distance from the track to the sense wire determined by time-based tracking. This quantity is obtained from fits to the

---

<sup>1</sup>In fact, in average there are 30 hits per time based track, due to inefficiencies and holes in the drift chambers

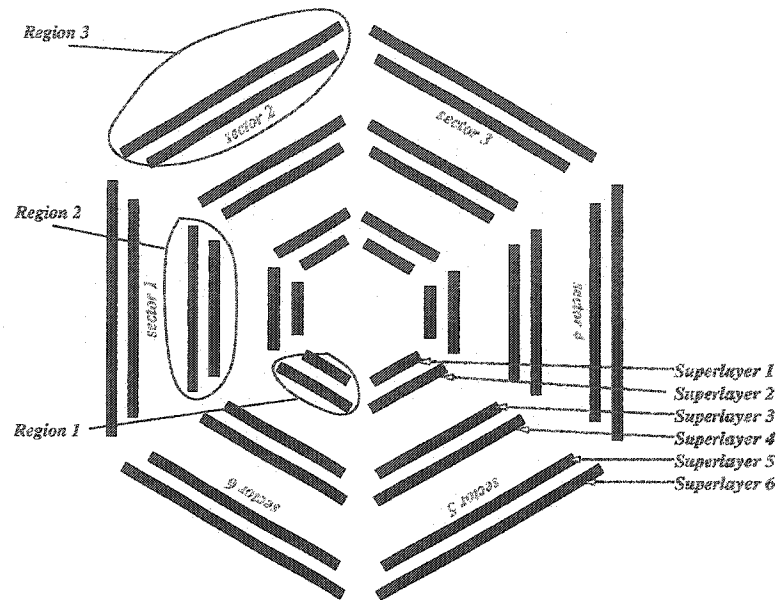


Figure 3-9: Schematic View of CLAS Drift Chambers. This view represents a slice through the drift chambers at target position. The schematic shows how regions and super-layers are placed and named.

global track that includes all layers.

- *DIST* is the predicted distance from the sense wire to the track, which is calculated from the drift time and other parameters. The drift time is determined from the TDC values for the wire corrected with fixed cable delays and track dependent delays such as flight time.

The difference between these quantities is called the “time residual”, defined as:

$$Res = |DOCA| - |DIST| \quad (3.22)$$

The sign of the “time residual” is determined by the sign of any systematic shift. The residuals are the primary means of measuring the resolution of the drift chambers. The standard deviations of the residual distributions are estimated by means of Gaussian fits.

Note, that *DIST* is defined as positive definite, while *DOCA* is assigned a sign determined whether the track passes to the right or to the left of the wire.

### 3.3.2 Function Parametrization

The goal of the calibration of the Drift Chambers is to parametrize the drift velocity function for every super-layer in each sector. The drift velocity function is the relation between the calculated distance of closest approach (*DIST*) of a particle track and the drift time, the time it takes the electrons created by the particle to drift to the sense wire. The time to distance correlation function is determined by the drift chamber geometry, operating conditions and the gas mixture. The fact that the cells of the drift chambers are not circular but hexagonal leads to angle-dependent corrections <sup>2</sup>. The drift time to drift distance function at a given track entrance angle is given by:

$$x(t) = v_0 t + \eta \left( \frac{t}{t_{max}} \right)^p + \kappa \left( \frac{t}{t_{max}} \right)^q \quad (3.23)$$

where  $v_0$  is the saturated drift velocity near  $t = 0$ , and the parameters  $\eta, \kappa, p$  and  $q$  are determined by fitting the time-to-distance distribution. For the tracks near the outer edge of the cell, the first arriving ions follow the electric-field line from the field wire to the sense wire, independent of entrance angle [22]. The corresponding drift time is referred to as  $t_{max}$ . A normalized drift time  $\hat{t} = t/t_{max}$  is used as an argument to the time-to-distance function that satisfies the cell boundary constraint:

$$x(\hat{t} = 1, \alpha) = C \cdot \cos(30^\circ - \alpha) \quad (3.24)$$

---

<sup>2</sup>By angle the track angle relative to the edges of hexagon is understood, defined to be in the range of  $0^\circ - 30^\circ$

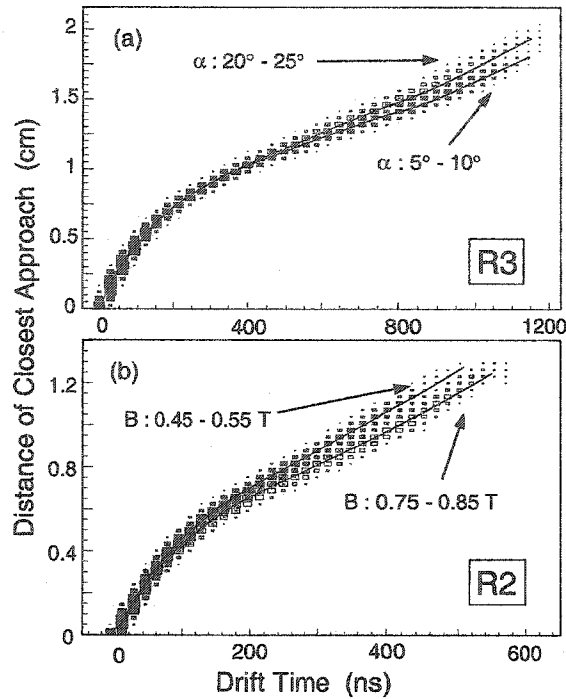


Figure 3-10: Scatter plot of DOCA versus the corrected drift time for a) R3 axial wires showing the track local-angle dependence, and b) R2 axial wires showing the magnetic-field dependence where the local angle ranges between  $23^\circ$  and  $25^\circ$ . The overlaid curves represent the fitted time-to-distance function.

where  $\alpha$  is the track entrance angle and  $C$  represents the cell size. The time-to-distance function is deduced using a correction function:

$$x(\hat{t}, \alpha) = x_0(\hat{t}, \alpha) + C(\cos(30^\circ - \alpha) - \cos(30^\circ - \alpha_0))f(\hat{t}) \quad (3.25)$$

where  $x_0$  represents the drift distance expected for a given normalized drift time assuming an entrance angle  $\alpha_0$ . The entrance angle is taken to be the average entrance angle for the full fitted data set. The function  $f(\hat{t})$  is used to correct the extracted drift distance for the true entrance angle of the track. Since Region 2 of the drift chambers is located between the torus cryostats, the inhomogeneous magnetic field affects the drift velocity.

These effects are modeled by a modification of the effective entrance angle of the track and by increasing  $t_{max}$ . These issues are studied and described in [22]. An example of the fitted time-to-distance distribution are shown in Figure 3-10 for the Region 3 chambers and for the Region 2 chambers.

### 3.4 Electromagnetic Calorimeter Time Calibration

The Electromagnetic Calorimeter (EC) is an important part of the CLAS detector. It serves three main functions [27]:

- Detection and triggering of electrons with momentum above 0.5 *GeV*. The total energy deposited in the EC allows minimum ionizing particle rejection at the trigger level.
- Detection of photons at energies above 0.2 *GeV*, allowing  $\pi^0$  and  $\eta$  reconstruction from the detection of their  $2\gamma$  decays.
- Detection of neutrons, with discrimination between photons and neutrons using time-of-flight measurements.

The EC time calibration is performed using the electron time measured by the Time-of-Flight counters. Since there is no magnetic field between the scintillator counters and the electromagnetic calorimeter, the track of the particle is straight. After calibrating the Time-of-Flight system, one can predict the time measured by the EC as:

$$T_{EC} = T_{SC} + \frac{d_{trk} \cos \alpha}{c} \quad (3.26)$$

where  $T_{SC}$  is the time measured by TOF,  $d_{trk}$  is the distance between TOF and EC strips,

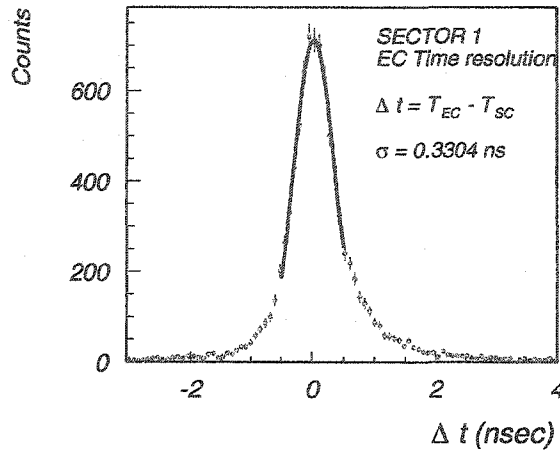


Figure 3-11: The time resolution of the CLAS Electromagnetic Calorimeter.  $\Delta t$  defined in Eq.(3.28) is plotted for one sector after EC calibrations.

and  $\alpha$  is the particle impact angle on the EC plane. The time measured by EC ( $T_{EC}$ ) is assigned to the strip with the largest ADC signal in each of three views. Then the time dependence is fitted with the function:

$$T_{EC} = P_0 + P_1 \cdot A_{TDC} + \frac{P_2}{\sqrt{A_{ADC}}} + P_3 \cdot L^2 + P_4 \cdot L^3 - \frac{L}{v_{eff}} \quad (3.27)$$

where  $L$  is the distance from the hit point to the EC readout edge,  $v_{eff}$  is the speed of light in the scintillator material, and  $A_{ADC}$  and  $A_{TDC}$  are the ADC and TDC values, respectively. The first two terms are the linear responses of the TDCs, the third term is the time-walk correction, the fourth and fifth terms are small corrections for the fact that the signals arrive to the readout edge at slightly different times for scintillator bars connected to the same PMT, and the last term compensates the time for the scintillator light to travel from the hit position to the readout edge. The fit parameters are saved in the calibration database. The time difference between the Time-of-Flight and the EC can be seen in Figure 3-11. The

quantity  $\Delta t$  (for electrons) is plotted for one sector, defined as:

$$\Delta t = T_{EC} - T_{SC} - T_{trk} \quad (3.28)$$

where  $T_{EC}$  is the time measured with the Electromagnetic Calorimeter,  $T_{SC}$  is the time measured with the TOF counters, and  $T_{trk}$  is the time that it takes a particle with  $\beta = 1$  to travel the distance between the TOF counters and the plane of the EC. As can be seen from the picture the overall  $\sigma$  is  $\sim 330$  ps, which is partially due to the TOF resolution. Taking the TOF resolution equal to 150 ps, one can calculate the EC resolution for electron to be  $\sqrt{330^2 - 150^2} = 294$  ps. For neutral particles the resolution is not as good as for electrons.

### 3.5 Čerenkov Detector Calibration

The Čerenkov detector calibrations are important for determining the detector efficiency and for correct time measurements. In order to achieve precise knowledge of the amplitude and the time from the Čerenkov detector (CC), one needs to calibrate some parameters from run to run. Some parameters can be calibrated in the off-line analysis using beam interactions, and some parameters can be determined either with cosmic rays or intrinsic photo-multiplier noise [39]. The part of the calibration which are done without the beam interactions help determining the T1 (TDC channel to time constant), pedestals and Single-Photoelectron position. The T1 constant is calibrated using a pulsar signal, sent to each TDC channel with different time delays. The response of each TDC is fitted with linear function with T1 as a slope parameter (similar to T1 constant calibration of the TOF), and the obtained T1 parameter is saved in the calibration database for each TDC channel. For accurate ADC measurements the pedestals need to be calibrated. Usual value of pedestals

vary from 300 to 800 channels, and sigma is about 2 – 3 channels. The pedestal calibration of the CC is a part of pedestal calibrations for all detector group.

### 3.5.1 Cosmic Ray calibrations

The Single Photo-Electron (SPE) amplitude calibration is a unique procedure, used for the CC only. The SPE amplitude position calibration is done using self-triggering of the Čerenkov detector to measure the noise function and to define the position of ONE Photo-Electron. To measure SPE one needs to accumulate distribution of ADC for every PMT. Then this distribution is fitted with Gaussian function to determine the SPE position. An example is shown in Figure 3-12. In case of large noise the background is parametrized with  $f(x) = a \cdot e^{-bx}$ . An example of PMTs with large noise is shown on Figure 3-13, fitted with Gaussian function plus exponential background.

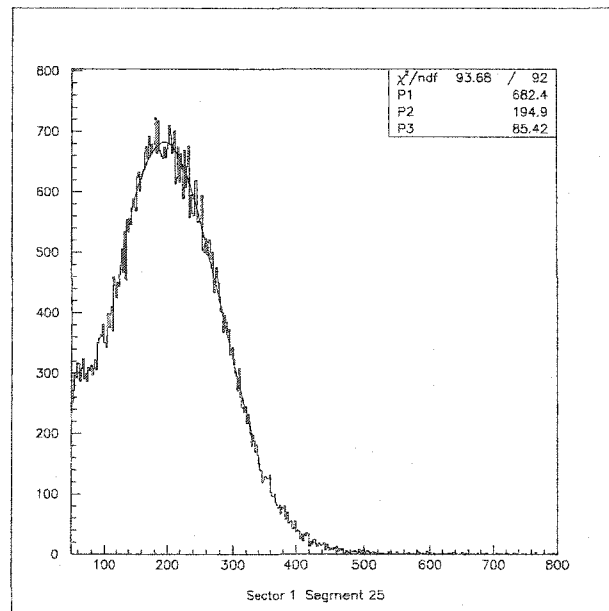


Figure 3-12: Calibration of Single photo-electron amplitude.

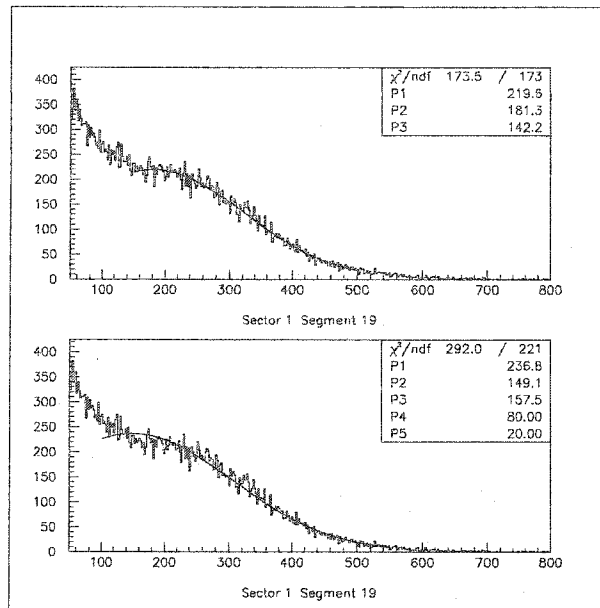


Figure 3-13: Example of PMT with large noise function fitted with Gaussian function and a background of form  $f(x) = a \cdot e^{-bx}$ .

### 3.5.2 Electron Beam Calibration

In order to obtain improved timing information from the Čerenkov detector one needs to obtain the time offset for each PMT. The constant, called  $T_0$ , is obtained using timing information from the TOF scintillator counters. This offset can be calculated using time information from the CC and the TOF, and knowing the track length from the target to the CC plane and the SC plane. The difference between the CC and TOF reported times is fitted for each PMT and stored in the calibration database for off-line time correction. Figure 3-14 shows the mean values of this time difference distributions plotted versus the PMT number.

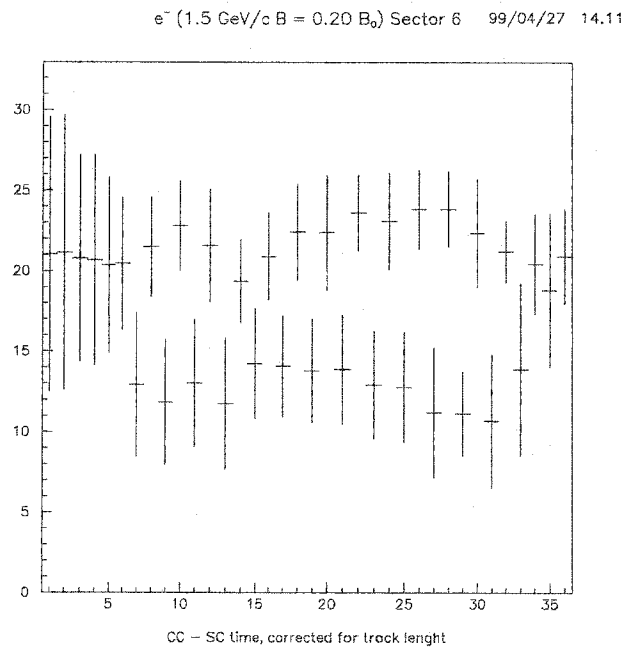


Figure 3-14: Mean value of T0 as function of PMT number. The time is corrected for track length.

# CHAPTER 4

## DATA ANALYSIS

### 4.1 The E1D Run Period

The data used for this DVCS analysis were taken during the e1d run period (the summary of e1d run period is presented in Table 4.1) which run from February 4 to March 2, 2000. A polarized electron beam of  $4.8 \text{ GeV}$ , with average polarization of  $67\% \pm 1.5\%$ , was scattered off a  $5 \text{ cm}$  liquid hydrogen target. The signals from the CC and the EC served as a trigger for recording events. All recorded events were reconstructed using RECSIS (CLAS event reconstruction program). During the e1d run about 660 runs were taken each of them consisting of separate files averaging  $450k - 500k$  events in each file. There were a total of about 2700 files selected with stable running conditions for our analysis. The total number of triggers in the selected files were  $1.261 \text{ M}$  events. After several passes of calibration these data were processed with RECSIS.

#### 4.1.1 Data Reconstruction

The raw data from the detector were processed several time with the RECSIS program.

Run Group	e1d
Beam Energy	4.805 GeV
Target	H <sub>2</sub>
Target Position	(0, 0, 0)
Target Length	5 cm
Average Beam Current	5 nA
Torus Current	3375
Mini-Torus Current	6000
Run Files	22848 – 23500
Luminosity	1.28 fm <sup>-1</sup>
Beam Polarization	67% ± 1.5%

Table 4.1: The e1d run summary.

At the first stage of data reconstruction (called “pass0”), the first file from each run (approx. 500 *K* events) from each day are processed. Then the calibration of each individual component of the CLAS detector is performed (see Chapter 3). After calibrating and saving all the constants in the calibration database all files of all runs are processed (this process is referred to as “pass1”). If necessary, final adjustments are made to the calibration constants and the data are processed once more with these better calibrations. The data cooking is

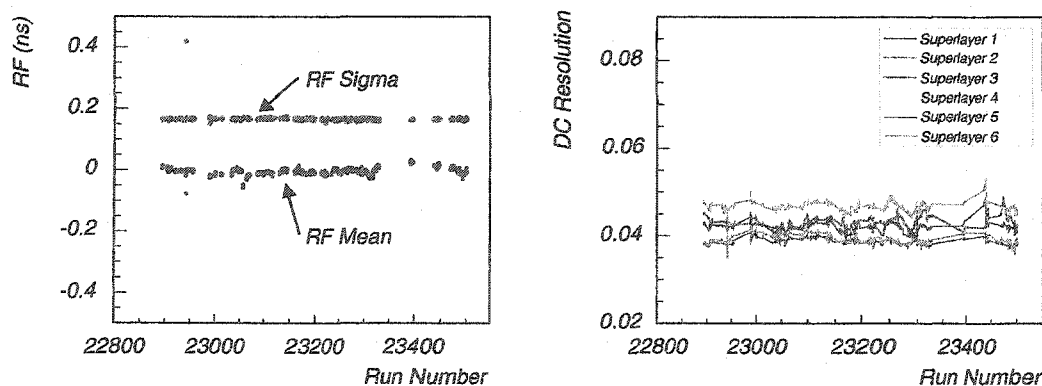


Figure 4-1: Calibration stability a) RF timing calibration for e1d run period. The fitted mean value and sigma are plotted. b) DC resolution for 6 super-layers.

done using the computer FARM provided by the Computer Center at JLAB. The FARM

consists of 175 dual processor Linux systems (20x450 MHz, 25x500 MHz, 50x750 MHz, 60x1 GHz, 20x1.8 GHz) providing a total CPU power of approximately 15000 SPECint95. This system allows for simulations data processing. These resources are shared between the three experimental halls, however CLAS is the more demanding user of this system. Usually one single file takes about 24 to 36 hours to process (depending on the run, and the

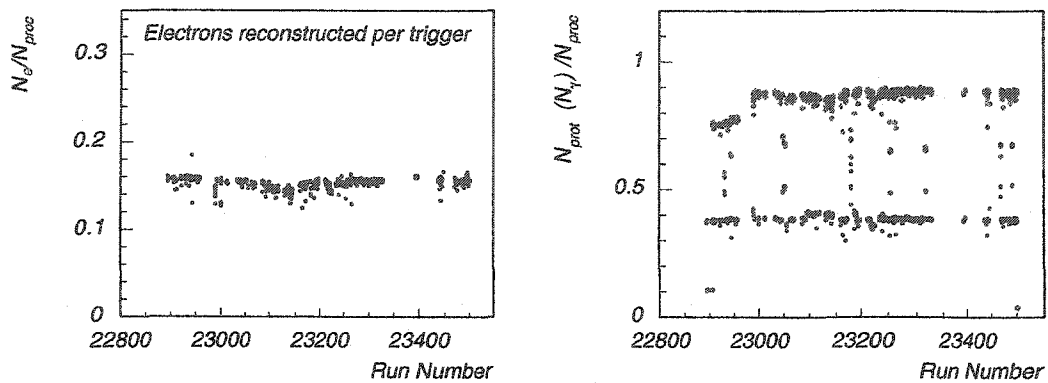


Figure 4-2: Reconstructed particles per run file, a) electrons per trigger, b) reconstructed protons (red dots,  $\sim 0.4$  per trigger) and photons (blue dots,  $\sim 0.85$  per trigger)

machine that is runs on). In order to process large quantities of data in a reasonable time frame, one needs to run 70 to 150 jobs (processes) on the FARM machines simultaneously, which makes it difficult to keep track of all the finished jobs and the quality of the results. For this purpose a module, called CSQL [40], was developed within the CLAS reconstruction framework to communicate with the CLAS offline database during the cooking process and to save important cooking parameters into this database. During the “cooking” process the reconstruction program would store important quantities, such as the number of reconstructed electrons and hadrons, in a temporary table in the CLAS Offline database, which is updated for every 2000 events, and when finished, an entry is made for each run in a separate table which contained these numbers for all runs. A web interface was also

developed [40], in order to interactively view the jobs running on the FARM and to plot reconstruction parameters in graphs on web pages. The procedure of data processing was automated by a cooking-control program, which would check for completed jobs (in the above mentioned database) and submit new ones, or resubmit jobs which exhibit problems during the cooking process. During the cooking procedure the important calibration con-

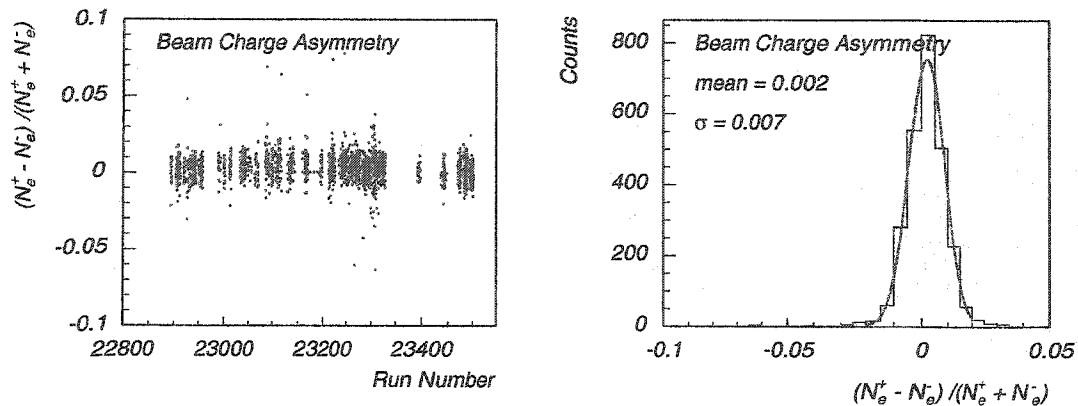


Figure 4-3: Beam charge asymmetry calculated according to Eq.(4.1) versus run number (a), and the beam charge asymmetry distribution for entire run period (b).

stants for each processed file were recorded in the CLAS Offline database to be able to check the stability of the calibration for the entire run period. In Figure 4-1 (a) the RF timing sigmas and means are plotted versus run number. Figure 4-1 (b) shows the Drift Chamber resolution for all super-layers for the entire run period. As can be seen from the plots, the calibration is quite stable over the entire e1d run period. About 18% of the events triggered by CLAS contained a properly identifiable electron and were reconstructed as a good events, the remaining 72% of the data was caused by energetic  $\pi^-$  causing the trigger while the electron remained undetected. The average number of reconstructed electrons per processed trigger against the file number can be seen in Figure 4-2 (a). The number of protons and  $\gamma$ 's reconstructed per file is also stored in the database. In Figure 4-2 (b) the

number of reconstructed protons and photons is plotted versus the run number. Each event recorded in CLAS has information about the electron polarization. One would expect the same number of electrons reconstructed (detected) for both negative and positive helicities. The beam charge asymmetry was calculated as:

$$A_{BC} = \frac{N_e^+ - N_e^-}{N_e^+ + N_e^-} \quad (4.1)$$

where  $N_e^+$  ( $N_e^-$ ) is the number of electrons registered with positive (negative) helicity. Figure 4-3 shows the difference of positive and negative helicity electrons detected normalized to the total number of electrons in the file. As expected the difference is centered around "0" with deviation of  $\sigma$  of 0.7%.

## 4.2 Particle Identification

### 4.2.1 Electron ID

During the cooking process RECSIS selects possible electron candidates based on the measured sign of the charge of the particle, deposited energy in the EC and a hit in the CC. RECSIS will mark these electron candidates with particle id 11 or 0 depending on whether they pass a certain set of cuts or not. After the cooking process one needs to do a more careful particle id for electrons and other particles used in the analysis. For the electron id the energy deposited in the EC and the number of photoelectrons in the CC are used. First, the electron candidates with a hit close to the edge of the Electromagnetic

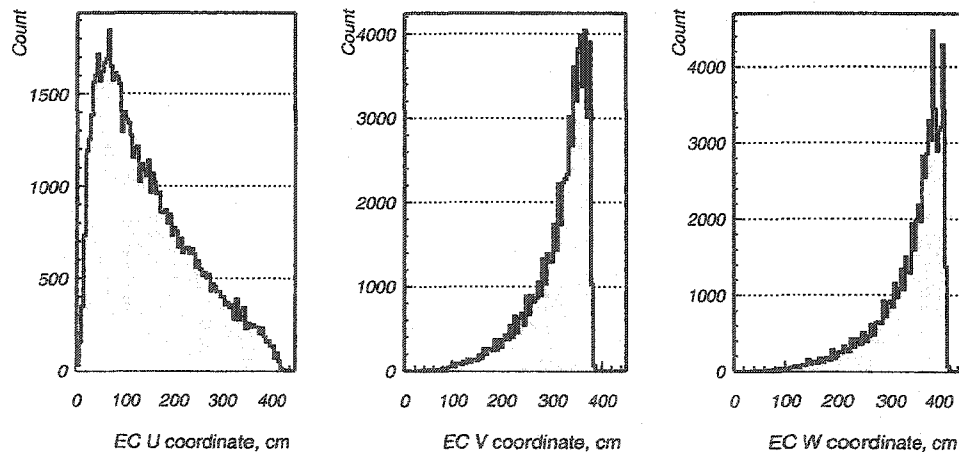


Figure 4-4: The electron hit coordinates are plotted for U,V and W planes from left to right. The cuts were used to eliminate events too close to the edge of Calorimeter ( $U > 15$ ,  $V < 370$  and  $W < 405$ ).

Calorimeter are rejected by applying a cut on the hit position. The electron-pion rejection relies on identifying the shape of the shower produced by a particle in the calorimeter material. When the electron candidate hits close to the edge of the Calorimeter, part of the shower is lost and the corresponding energy is not detected. In order to ensure

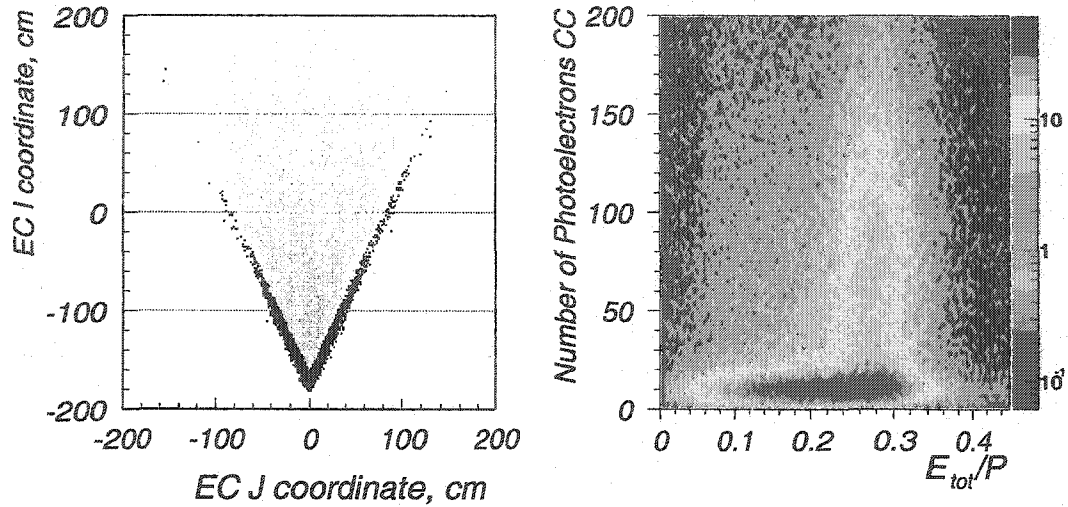


Figure 4-5: (a) EC fiducial cuts. The effect of the applied cuts is shown. The dark area corresponds to all electrons reconstructed by RECSIS, and the lighter area electrons that passed the cut. (b) The number of Photo-Electrons in the CC detector versus energy deposited in the EC. A cut was applied to the number of Photo-Electrons ( $n_{phe} > 25$ ) to eliminate pions.

clean electron-pion separation it is important to cut out these events. Since the EC has three layers of scintillators oriented  $120^\circ$  against each other, the hit position is defined by 3 numbers which represent the distance of the hit from each edge of the Calorimeter (the distance is measured from the hit to the edge where the PMT readout is). In this coordinate system the distances are denoted as  $U$ ,  $V$  and  $W$ . A typical distribution of these distances for electron candidates is shown in Figure 4-4. The cut used to reject events close to the edge are  $U > 15$ ,  $V < 370$ ,  $W < 405$ . Figure 4-5 (a) shows the effect of applied cuts. The dark area is the distribution of hits on the calorimeter plane which we cut out. The distances measured in the Calorimeter frame can be transformed into a 2-dimensional Cartesian coordinate system (usually denoted  $I$  and  $J$ ) which represent the hit position on the surface of the Calorimeter. In Figure 4-5 (a) the distribution of the hits is shown on the surface of the Calorimeter before (the dark area) and after (light area) applying the cuts.

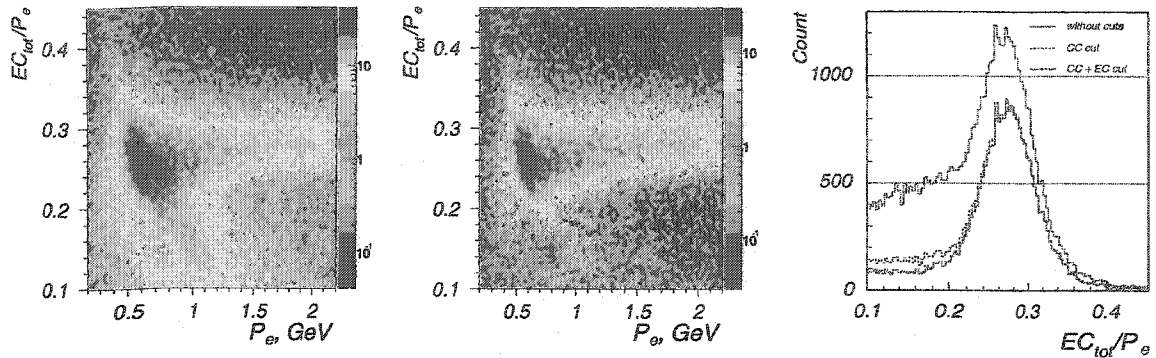


Figure 4-6: The EC deposited energy normalized to momentum versus momentum of the particle, (a) for all electron candidates, (b) after CC+EC cuts. (c) the  $EC_{tot}/P$  distribution showing effects of the cuts.

The next cut used to identify electrons is a cut on the number of photoelectrons produced by the electron candidate in the Čerenkov detector. In Figure 4-5 (b) the distribution of the number of photoelectrons produced in the CC is plotted against the total deposited energy in the Calorimeter for electron candidates. Pions occupy the lower part of the graph. The cut  $N_{ph} > 2.5$  was used to reject pions (where  $N_{ph}$  is the number of photoelectrons in CC). As mentioned above the electron-pion separation relies on identifying the shape of the shower produced by a particle in the EC. For this reason the readout system of the EC was divided into inner (5 layers) and outer (8 layer) parts. The signal is collected separately for inner (closer to the target) and outer part, then in the reconstruction code a “whole” layer is constructed as a sum of the signals from the inner and the outer parts. Since the pions at these energies behave as minimum ionizing particles, the energy deposited in the Calorimeter should be the same, independent of their momentum. In Figure 4-6 (a) the distribution of the  $EC_{tot}/P$  is plotted against the particle momentum, where  $EC_{tot}$  is the total energy deposited in the EC and  $P$  is the momentum of the electron candidate. The lower band corresponds to pions. In Figure 4-6 (c) the effect of the applied cuts can be

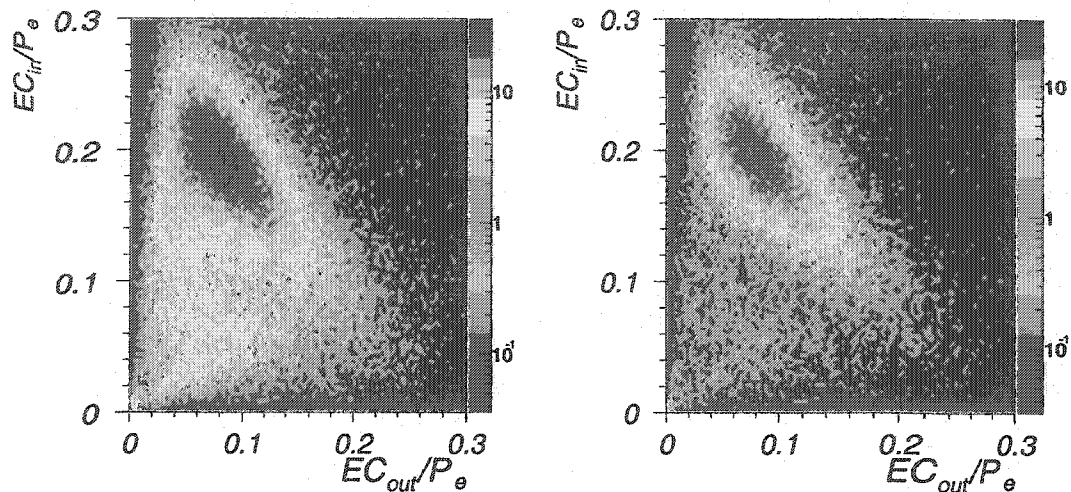


Figure 4-7: Electromagnetic shower distribution in the EC for electron candidates. (a) the deposited energy in the inner versus outer part of EC before cuts and (b) after applied cuts on CC+EC.

seen. The dashed line is the distribution of the  $EC_{tot}/P$  for all electron candidates, the high left shoulder represents pions misidentified as electrons. The dotted line is the same distribution after applying the cut on the number of photoelectrons in the CC. Evidently the left shoulder reduces significantly, with a small reduction under the peak. The solid line shows the distribution after applying the cut on the edges of Calorimeter in addition to the CC cuts. The effect of the cuts can be observed in Figure 4-6 (a) and (b), where the tail in the bottom corner disappears when the cuts are applied. Similarly, the electromagnetic shower produced by the electron is expected, on average, to leave more energy in the inner part of the calorimeter, while for minimum ionizing particles (such as pions with high energy) the energy deposited in the inner and outer parts should depend only on the length of the path through the scintillating material. In Figure 4-7 (a) the distribution of deposited energy normalized to the particle momentum in the inner part of the EC is plotted versus the energy deposited in the outer part. Pions can be visually distinguished in the left bottom

corner of the plot. In Figure 4-7 (b), the same distribution is plotted, the cuts are applied. The events in the left-bottom corner is strongly diminished. As mentioned before both

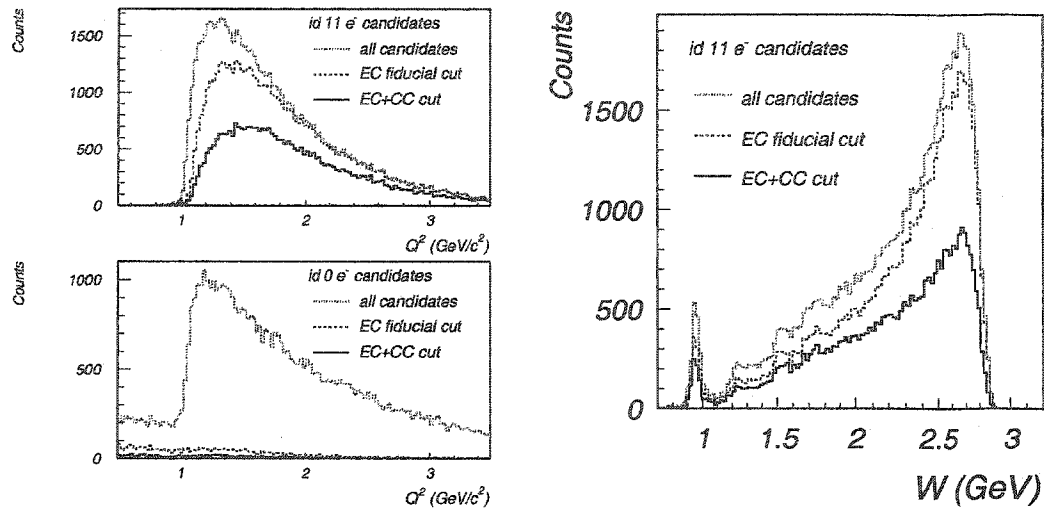


Figure 4-8:  $Q^2$  and  $W$  distributions before and after cuts, a)  $Q^2$  for electron candidates with  $id=11$ , b)  $Q^2$  for electron candidates with  $id=0$ , c)  $W$  spectra for electron candidates with  $id=11$ .

types of electron candidates ( $id = 11$  and  $id = 0$ ) were considered in electron identification. The result of the cuts are shown in Figure 4-8 for the distribution of  $Q^2$  and  $W$ , before and after the cuts. Figure 4-8 (a) shows the  $Q^2$  distribution for electron candidates with particle  $id=11$ , and (b) for candidates with  $id=0$ . Particles that passed the cuts were initially marked as good electrons by reconstruction program, while very few candidates were selected from the  $id = 0$  sample.

### 4.2.2 Proton ID

In CLAS charged hadrons are identified by charge (in-bending or out-bending track in DC), momentum and the time-of-flight calculated from SC measured time [35]. The CLAS TOF system allows for separation of protons and kaons up to 1.6 GeV, and protons and pions up to 2.5 GeV. The preliminary identification of particles is done using the distribution of particle momentum versus  $\beta$ ,  $\beta = L/t_{TOF}$ , where  $L$  is the path length and  $t_{TOF}$  is the time-of-flight from interaction vertex to the SC counter. A typical picture of  $\beta$  versus momentum for positively charged hadrons can be seen in Figure 4-9 (a). The red band represents protons identified by RECSIS, and the curves correspond to  $\pi^+$ ,  $K^+$ ,  $p$  and  $d$  (deuteron) respectively calculated as  $\beta = P/E$ , where  $E = \sqrt{P^2 + m^2}$ , with  $m$  being the exact mass of the particle type. In Figure 4-9 (b) the calculated mass of the identified protons is plotted (dark area) on top of the masses of all positive hadrons (light area). For

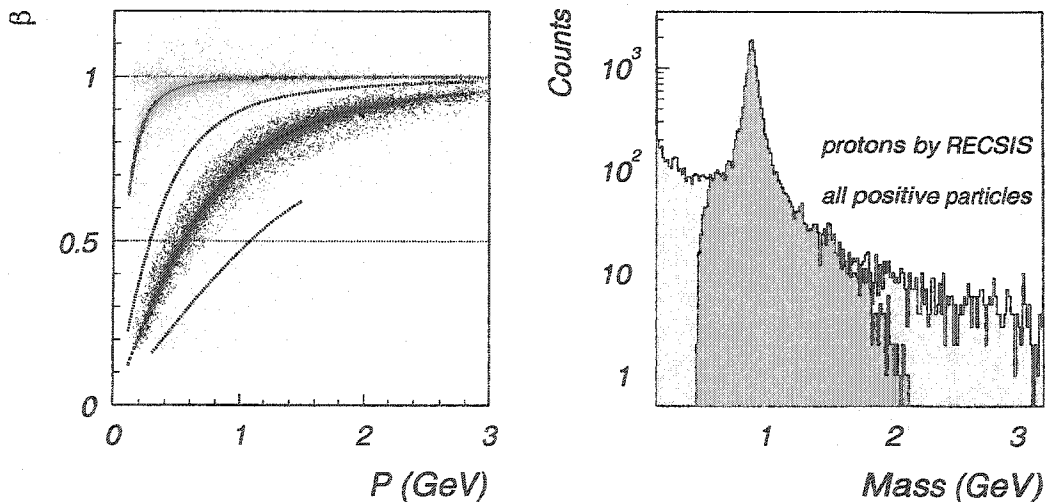


Figure 4-9: Proton identification with measured  $\beta$  of positive particles (a)  $\beta$  versus momentum of positively charged particle, the red band is RECSIS identified protons. (b) the mass distribution of positively charged particles (light area) and RECSIS identified protons (dark area).

these analysis additional selections were made using the vertex time of the track for better

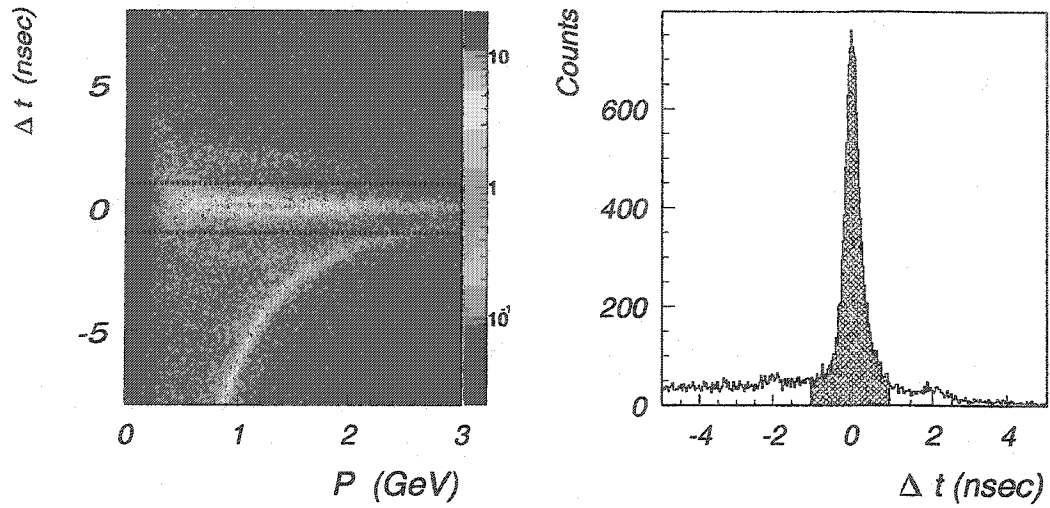


Figure 4-10: The  $\Delta t$  distribution calculated as shown in Eq.(4.2) (a)  $\Delta t$  versus momentum of positive particle, the red lines show the cut used for proton selection. (b) the  $\Delta t$  distribution, the shaded area represents proton cut.

proton identification. The time ( $\Delta t$ ) was calculated for all positive particles as:

$$\Delta t = SC_{time} - START_{time} - \frac{DC_{path}}{\beta} \quad (4.2)$$

where  $SC_{time}$  is the time measured by the scintillation counter,  $START_{time}$  is the time derived from the identified electron,  $DC_{path}$  is the length of the particle track measured by the Drift Chambers.  $\beta$  was calculated as:

$$\beta = \frac{P}{\sqrt{P^2 + M_p^2}} \quad (4.3)$$

where  $M_p$  is the proton mass ( $M_p = 0.93827$ ). In Figure 4-10 (a) the  $\Delta t$  distribution versus particle momentum is plotted. If the particle is a proton,  $\Delta t = 0$ , the band on the low side of the graph consists of  $\pi^+$  particles. The red dashed lines indicate the cut used to separate protons ( $-1 \text{ ns} < \Delta t < 1 \text{ ns}$ ). In Figure 4-10 (b) the  $\Delta t$  distribution is plotted

for all positive particles and the shaded area shows the particles selected as protons. From

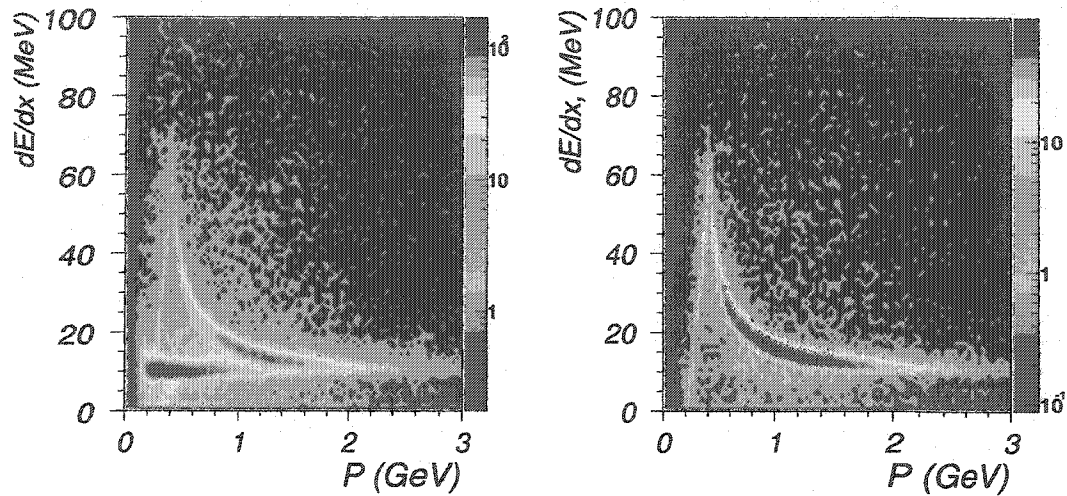


Figure 4-11: a)  $dE/dx$  for all positive particles, b)  $dE/dx$  for positive particles after cutting on  $\Delta t$ .

Figure 4-11 the effect of the timing cut can be seen. Figure 4-11 (a) shows  $\Delta E$  (the deposited energy measured by the scintillator counter) for all positive particles, and in plot (b)  $\Delta E$  for particles that passed the  $\Delta t$  cut is plotted. Pion events which occupied the bottom of the plot 4-11 (a) have disappeared in plot 4-11 (b). In Figure 4-12, the selection of protons can be seen. The calculated mass of the particles identified by RECSIS as protons, and those selected as protons with the  $\Delta t$  cut, is plotted on top of the mass of all positive particles. The  $\Delta t$  cut provides a quite good proton selection and a reduction of the shoulders in the distribution without cutting event from the peak.

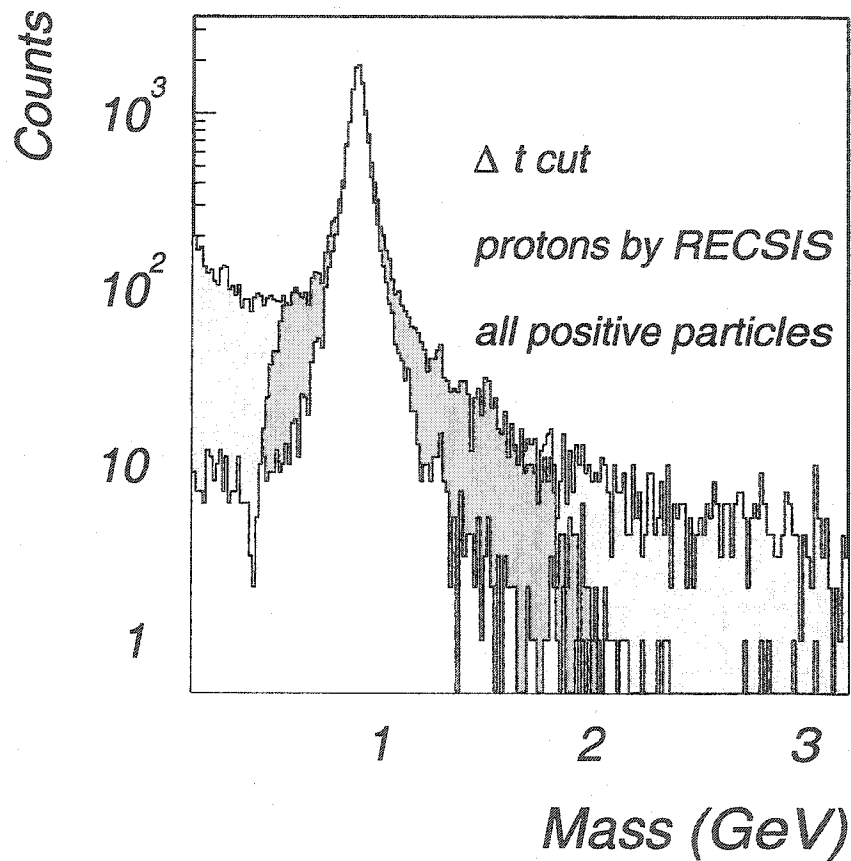


Figure 4-12: Proton selection, SEB identified protons compared with protons identified using  $\Delta t$  cut. The “gray” area is the mass of all positively charged particles, the darker area is the protons identified by RECSIS using cut on momentum versus  $\beta$  distribution, and the lighter area are protons selected using cut on  $\Delta t$ .

### 4.2.3 Photon ID

In CLAS neutral particles are detected and identified in the electromagnetic calorimeter. The neutral particle candidate has to have an EC hit and no matching DC or SC hits. Then time-of-flight from the target is calculated. Then using timing information from the Electromagnetic Calorimeter and the start time derived from the identified electron,  $\beta$  is calculated for the neutral particle. Neutrons and photons are identified by using  $\beta$  of the neutral hit. For these analysis for photon selection a cut on  $\beta$  of the particle ( $\beta > 0.8$ ) was used. Events with an electron, a proton and two neutral particles were selected to

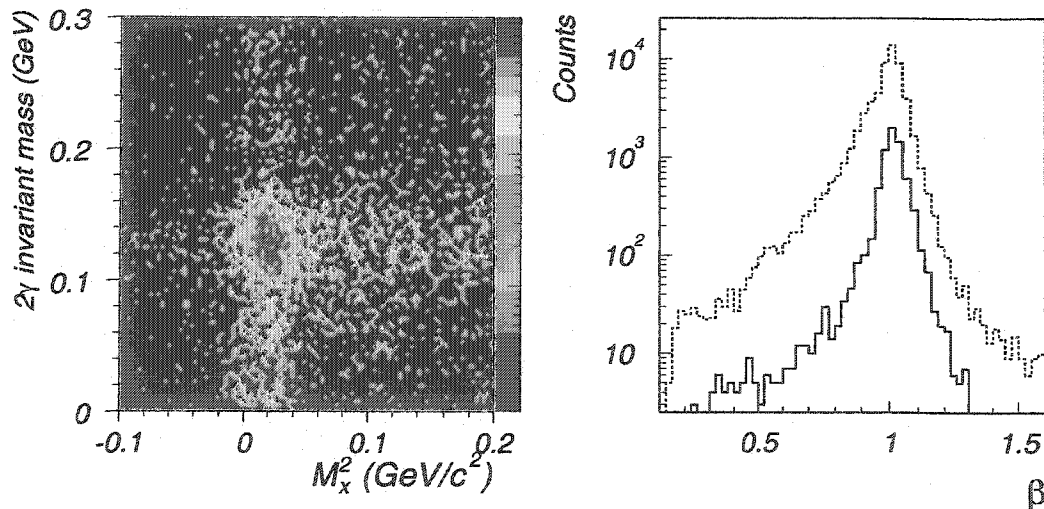


Figure 4-13: The  $ep$  missing mass square distribution for  $ep \rightarrow ep\gamma\gamma$  is plotted versus  $2\gamma$  invariant mass. On the right the negative particles beta is plotted (*dashed line*) and neutral particles that pass invariant mass cut (*solid line*)

verify this cut. In Figure 4-13 (a) the invariant mass of two neutral particles is shown versus missing mass square of  $e'p$ . In the reaction  $ep \rightarrow e'p\gamma\gamma$  the invariant mass of two  $\gamma$ 's should be around the  $\pi^0$  mass. In Figure 4-13 (b) the distribution of  $\beta$  is plotted for all neutral particles in the selected events (*dashed line*) and  $\beta$  of particles that passed the invariant mass cut around the  $\pi^0$  mass (*solid line*). The energy of the neutral particles

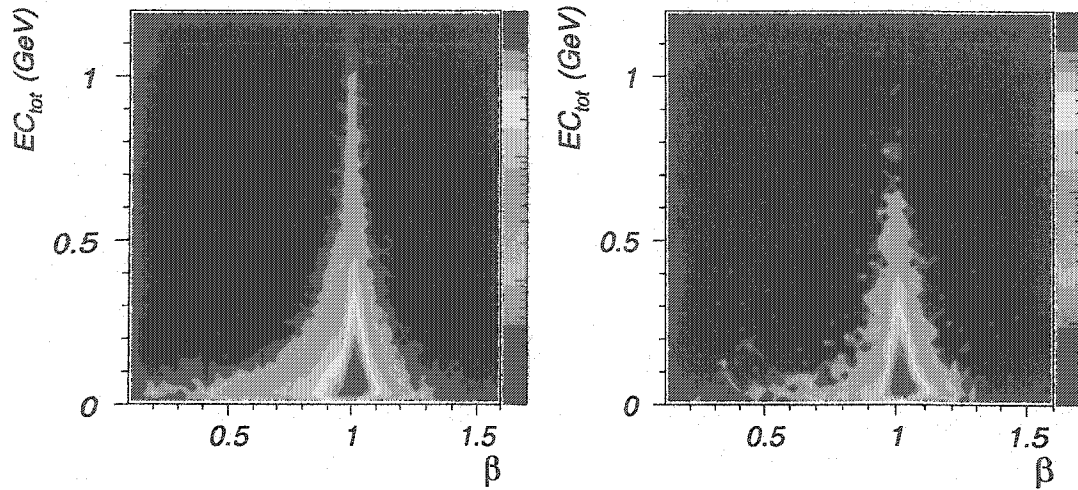


Figure 4-14: The neutral particle EC deposited energy (a) before invariant mass cuts and (b) after cuts.

is reconstructed using the Electromagnetic Calorimeter. Figure 4-14 shows the deposited energy in the EC versus  $\beta$  for neutral particles (a) before cuts on the invariant mass, and (b) after cuts. From this plot it can be seen that neutral particles with low  $\beta$  ( $\beta$  below 0.8), which correspond to neutrons, deposit a small amount of energy in the EC, and the cut on the invariant mass eliminates those particles. If the particle hit is close to the edge of the EC, part of the shower generated by the particle in the Calorimeter is lost, which can result in an inaccurate energy reconstruction. To reject these events the same type of fiducial cuts as for electrons were used.

### 4.3 Particle Momentum Corrections

Due to uncertainties in the torus field distribution and in the DC alignment one needs to do momentum corrections for the final detected particles. These corrections were done for the electron and the proton momentum. Two methods of momentum corrections were considered.

#### 4.3.1 Electron momentum corrections

For electron momentum corrections radiative elastic events are used (at  $W > 2.0$ ). These are events where the electron radiates a photon and then scatters elastically off the proton, so that the missing momentum of the  $e'p$  system should be along the direction of the electron beam. These events can be selected using cuts on the transverse missing momentum and the electron-proton scattering plane.

In Figure 4-15 (a) the transverse component of the missing momentum is shown (the center of the graph corresponds to the beam direction). The following missing momentum cut was applied:

$$\sqrt{\left(\frac{P_m^x}{P_m}\right)^2 + \left(\frac{P_m^y}{P_m}\right)^2} < 0.01 \quad (4.4)$$

where  $P_m$  is the total missing momentum and the  $P_m^x$  and  $P_m^y$  are the  $x$  and  $y$  components, respectively (see Figure 4-15 (a)). In Figure 4-15 (b) the electron proton scattering plane difference is shown,  $(|\phi_e - \phi_p|)$ , for events before the cut on missing momentum (*dashed line*) and after (*solid line*). The sharp peak around  $180^\circ$  corresponds to elastic scattering of the electrons off the proton. One can see from the figure that after the cut, the background disappears, leaving a sharp peak around  $180^\circ$ . Also a cut on the electron-proton scattering plane is used requiring,  $178^\circ < |\phi_e - \phi_p| < 182^\circ$ . The reaction  $ep \rightarrow ep$  was studied in the

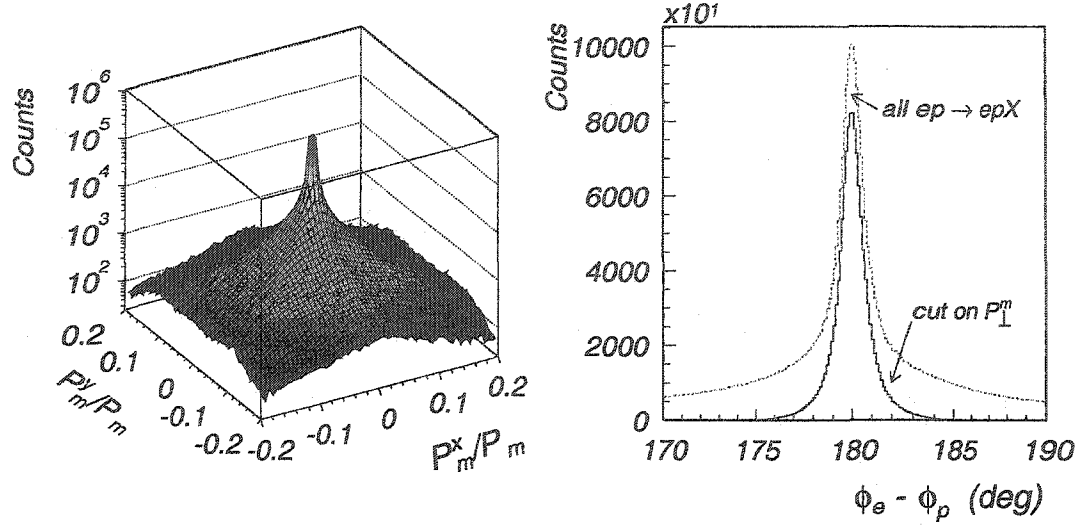


Figure 4-15: Radiative elastic events selection. a)  $epX$  missing momentum transverse component, b)  $ep$  scattering plane ( $|\phi_e - \phi_p|$ ) angle before (*dashed line*) and after *solid line* the cuts.

range  $W > 2.0 \text{ GeV}$  to derive the electron momentum corrections. In elastic scattering the full kinematics are defined by two variables. The incoming electron energy can be calculated assuming that the polar angles of the electron ( $\theta_e$ ) and the proton ( $\theta_p$ ) are reconstructed correctly. The incoming and scattered electron momenta are calculated according to:

$$P_i^e = \frac{M}{1 - \cos\theta_e} (\cos\theta_e + \cos\theta_p \frac{\sin\theta_e}{\sin\theta_p} - 1) \quad (4.5)$$

$$P_f^e = \frac{P_i^e}{1 + \frac{P_i^e}{M}(1 - \cos\theta_e)} \quad (4.6)$$

where  $P_i^e$  is the electron momentum after radiating a photon,  $P_f^e$  is the scattered electron momentum and  $M$  is the proton mass. For momentum correction the ratio of  $P_f^e$ , calculated from the scattering angles of the electron and the proton measured by the DC, to the momentum of the electron, measured by the DC, is used. Events are grouped in five momentum bins:  $P_1 = 0.5 - 0.7 \text{ GeV}$ ,  $P_2 = 0.7 - 0.9 \text{ GeV}$ ,  $P_3 = 0.9 - 1.2 \text{ GeV}$ ,  $P_4 = 1.2 -$

1.6GeV and  $P_5 = 1.6 - 3.0\text{GeV}$ . Then this ratio of momenta of the scattered electron is analyzed as a function of azimuthal angle. The slices of this ratio at each azimuthal angle are fitted with Gaussian function (distributions in each sector are analyzed separately). The mean values of the Gaussian fits are parametrized as a function of  $\phi_e$  and fitted with 4th degree polynomial. The results of the fits are stored for each sector and momentum bin separately to be used for electron momentum corrections in the final analysis.

### 4.3.2 Proton momentum corrections

Protons scattered in CLAS detector pass through material before being detected, and are losing part of their energy. Energy loss corrections for low momentum protons were derived using GEANT simulation for CLAS (GSIM) with eld run conditions. The energy loss was parametrized using a 4 *th* degree polynomial given by:

$$P_p^{corr} = \frac{P_p}{(0.630795 + 1.60892 \cdot P_p - 2.40478 \cdot P_p^2 + 1.20581 \cdot P_p^3)} \quad (4.7)$$

where  $P_p$  is the reconstructed proton momentum and  $P_p^{corr}$  is the proton momentum corrected for energy losses. After the energy loss corrections, additional corrections were done to eliminate detector specific shifts. Similar to the electron momentum corrections, the proton momentum corrections show an azimuthal dependence. The reconstructed proton momentum can be compared with the momentum calculated from elastic scattering, using the incoming electron energy and assuming that the polar angle of the proton was reconstructed correctly. The reaction  $ep \rightarrow e\pi^+n$  was studied for the proton momentum corrections. Since positive particles in the same momentum range travel through the same regions in the drift chamber, corrections derived for  $\pi^+$  will be applicable for protons as

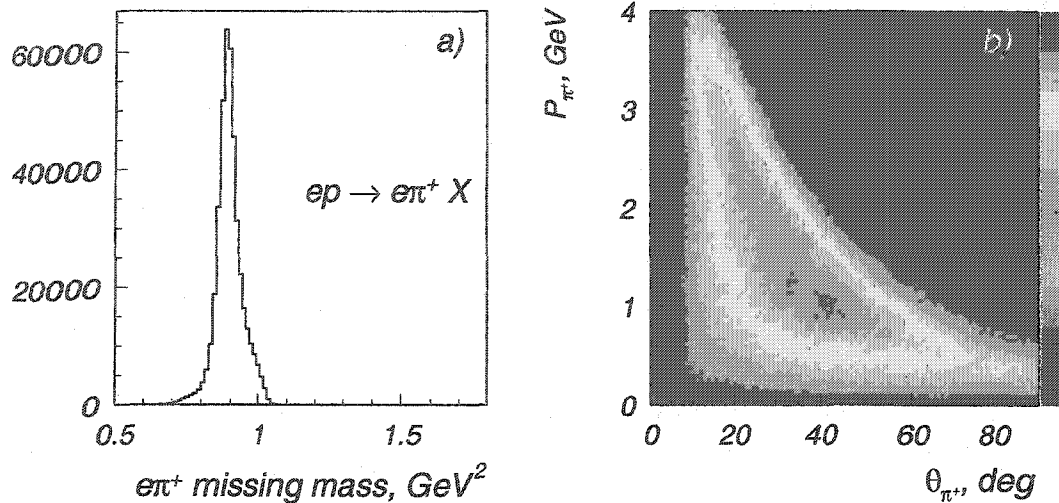


Figure 4-16:  $ep \rightarrow e\pi^+n$  reaction selection, (a) the missing mass of detected  $e'\pi^+$ , (b)  $\pi^+$  kinematical coverage.

well. To select the reaction, events with an electron and a  $\pi^+$  in final state were selected. A cut was applied to the  $e\pi^+$  missing mass around the neutron mass to select  $e\pi^+n$  events (Figure 4-16). The electron momentum was corrected using the correction functions derived from radiative elastic events and, assuming that the polar angle of the  $\pi^+$  was correctly reconstructed, the  $\pi^+$  momentum was calculated (see appendix). The corrections were done for seven  $\theta_{\pi^+}$  bins for each sector separately. The ratio of the calculated and reconstructed momenta for each  $\theta_{\pi^+}$  bin were sliced in  $\phi$  and fitted with Gaussian function. The resulting distribution of the fitted mean values were analyzed with a fourth order polynomial in  $\phi_p$ . The corrections were done in six momentum bins. Figure 4-17 shows final fits for  $p^{meas}/p^{calc}$  distribution for one sector.

### 4.3.3 Second method of corrections

As an alternative method of correcting the particle momentum the method from CLAS-Note 005/2003 [41] was adopted. The reconstructed particle momenta have a clear de-

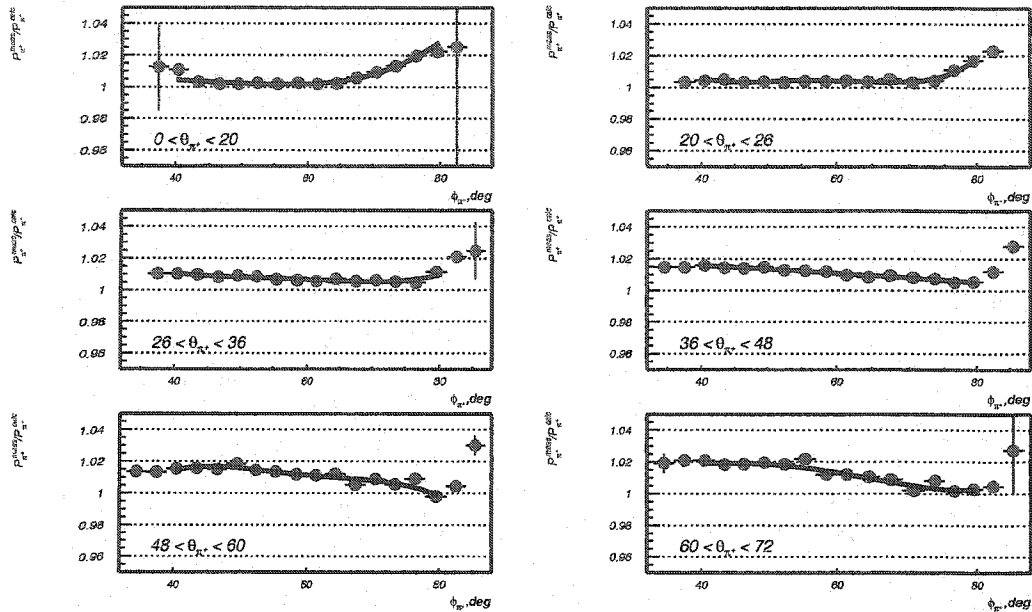


Figure 4-17: Fit to the calculated over reconstructed  $\pi^+$  momentum for different  $\theta_{\pi^+}$  bins (one sector).

pendence on  $\phi_e$  and  $\theta_e$ . Systematic deviations of the reconstructed momentum can arise from:

- Misalignment of the drift chambers relative to their nominal positions.
- Effects like wire sag, thermal and stress distortions of the drift chambers.
- Insufficient or incorrect information in the reconstruction code on the exact location of the wire feed-through holes in the drift chambers.
- Incomplete knowledge of the magnetic field distribution generated by the torus.

All this could affect the angle and momentum reconstruction of particles. In this second method the assumption is made that both polar angle and momenta are distorted by systematic displacements of the drift chambers and by magnetic field deviations from the field map used in the reconstruction code. The drift chamber displacement was parametrized by 10 fit

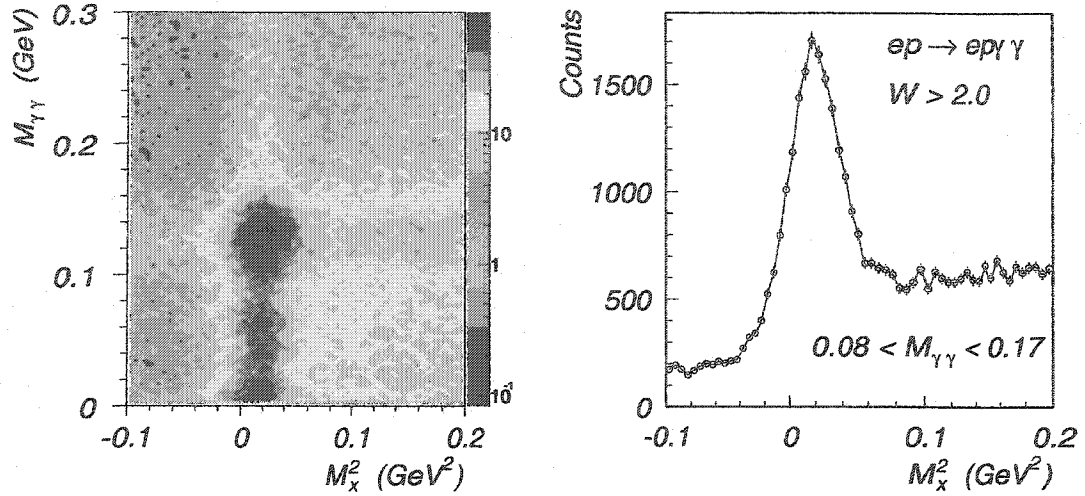


Figure 4-18: Pion event selection. (a) invariant mass of  $2\gamma$  in reaction  $ep \rightarrow e'p\gamma\gamma$  versus  $e'p$  missing mass, (b)  $e'p$  missing mass square distribution after cut on invariant mass ( $0.08 < M_{\gamma\gamma} < 0.17$ )

parameters in each sector. The effect of displacement of the chamber on the reconstructed track can be written as a change  $\Delta\theta$  in the polar angle and  $\Delta p$  in the momentum:

$$\Delta\theta = (A + B\phi + C\phi^2) \frac{\cos\theta}{\cos\phi} + (E + F\phi)\sin\theta \quad (4.8)$$

$$\frac{\Delta p}{p} = ((G + H\phi + K\phi^2) \frac{\cos\theta}{\cos\phi} + (L + M\phi)\sin\theta) \frac{p}{qB_{Torus}} \quad (4.9)$$

where,  $q$  is the particle charge in units of  $e$ ,  $p$  is the RECSIS reconstructed momentum in GeV,  $\theta$  the reconstructed polar angle and  $\phi$  is the azimuthal angle relative to the sector ( $\phi = \phi_e - \phi_{sector}$ ) where  $\phi = 0$  corresponds to the center of the sector. The parametrization of the  $B_{Torus}$  was used from the CLAS Note [41], defined as:

$$B_{Torus} = 0.76 \frac{I_{Torus} \sin^2 4\theta}{3375\theta / (rad)} \quad \text{for } 0 < \theta < \pi/8$$

$$B_{Torus} = 0.76 \frac{I_{Torus}}{3375\theta rad} \quad \text{for } \theta \geq \pi/8 \quad (4.10)$$

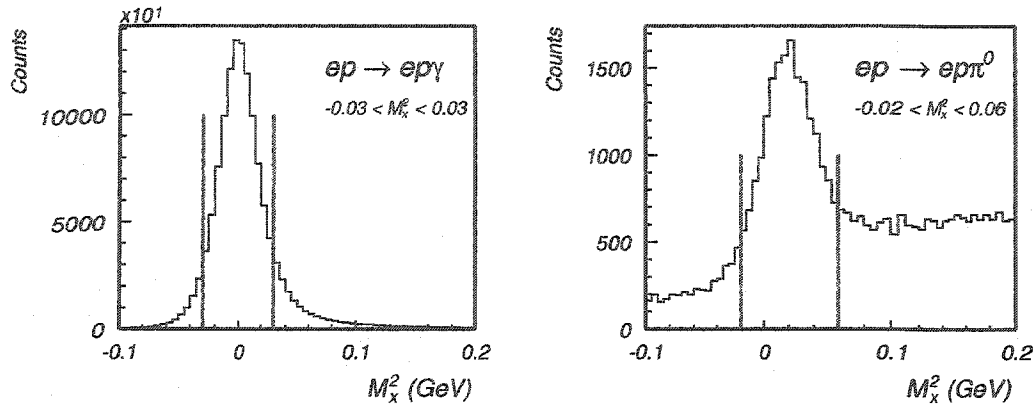


Figure 4-19: Event selection for MINUIT momentum corrections, a) the cut for radiative elastic events, b) cut for the pion events

In the original CLAS note the quadratic parameters in equation 4.8 and 4.9 in the  $\cos \theta$  term were absent. Since there was a quadratic dependence of the missing mass on the azimuthal angle these two parameters were implemented to correct for it.

#### 4.3.4 Selection of Final States

In the second method, for correction two final states were used; Bethe-Heitler ( $ep \rightarrow ep\gamma$ ) and single pion production ( $ep \rightarrow ep\pi^0(\gamma\gamma)$ ). The events were selected in the same kinematical region as was used in the DVCS analysis at  $W > 2.0 \text{ GeV}$ . A missing mass of  $-0.03 < M_x^2 < 0.03$  was used for radiative elastic events, and  $-0.02 < M_x^2 < 0.06$  for pion events. The distribution of radiative elastic and pion events ( $W > 2.0 \text{ GeV}$ ) with the cuts applied are shown in Figure 4-19.

#### 4.3.5 Fit procedure

A fitting code was developed, in C++ using the ROOT [42] libraries, for fitting the momentum corrections. The CERN package "MINUIT" [43] (fitting library) was used to

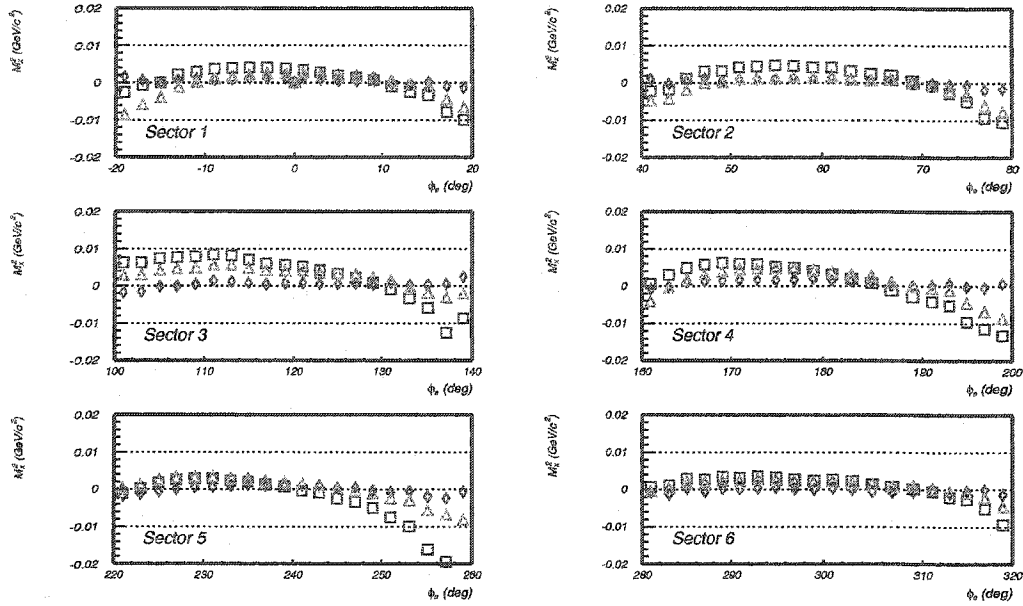


Figure 4-20: Radiative elastic events.  $ep$  missing mass  $\phi_e$  dependence for all sectors. Red squares are uncorrected, blue diamonds are corrected using method I and green triangles are corrected using method II.

optimize 96 parameters (16 per sector) for momentum and angle corrections. For each event the momentum and the polar angle of particle in the final state were corrected according to Eq.(??) and Eq.(??), then the shift of the missing mass from was calculated as:

$$ep \rightarrow ep\gamma, \quad \Delta\chi^2 = \frac{M_x^2(ep)}{(0.016\text{GeV})^2} \quad (4.11)$$

$$ep \rightarrow ep\pi^0, \quad \Delta\chi^2 = \frac{M_x^2(ep) - M_{\pi^0}^2}{(0.020\text{GeV})^2} \quad (4.12)$$

where  $M_x^2$  is the missing mass squared of the  $e'p$  system and  $M_{\pi^0}$  is the mass of the  $\pi^0$  ( $M_{\pi^0} = 0.134$  GeV). The numerical numbers in denominator are the  $\sigma$ 's of the photon and the pion respectively. The  $\chi^2$  that is minimized in the fitting procedure is the sum of all the  $\Delta\chi^2$  terms for all events. To avoid run away parameters the sum of the parameters divided

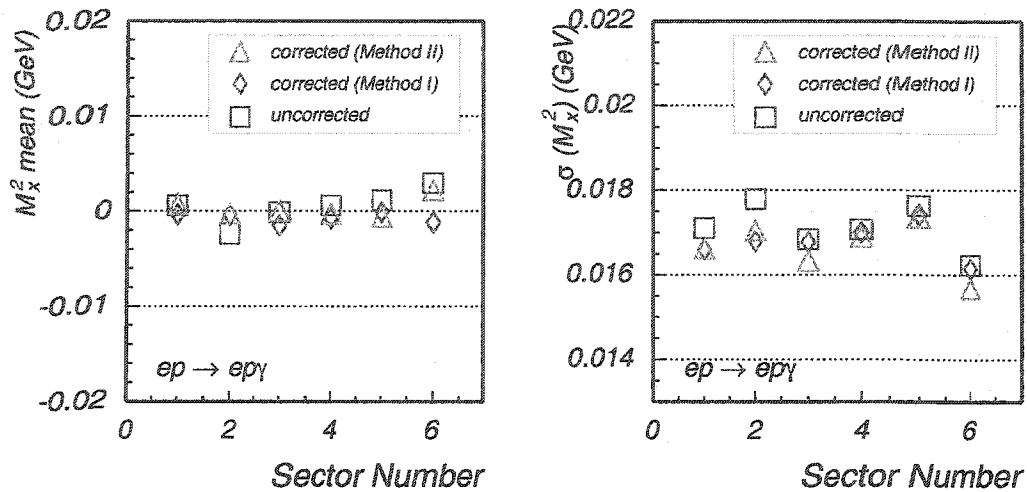


Figure 4-21: The mean and sigma of the radiative elastic peak as a function of electron sector in CLAS. The mean (a) and sigma (b) for each sector are plotted before corrections, and after corrections with two different methods described in this chapter.

by their sigma was added to  $\chi^2$ :

$$\Delta\chi_{params}^2 = \sum \frac{par^2}{\sigma^2(par)}$$

The parameters derived from “MINUIT” by minimizing  $\chi^2$  were used for particle momentum and polar angle corrections in the final analysis.

#### 4.3.6 Check of Corrections

After the corrections were made the missing mass distribution of the  $ep \rightarrow epX$  events did not have any visible  $\phi_e$  dependence. The two methods for momentum correction perform about the same. The missing mass mean distribution versus  $\phi_e$  for each sector can be seen on Figure 4-20. Where the “square” symbols are the mean values of radiative elastic events before any correction were done (except the proton energy loss corrections). The “diamond” shaped symbols represent mean values after the first method of corrections, where electron

and proton momentum were corrected independently and the “triangle” symbols are the mean values after the second method of corrections. In Figures 4-22 and 4-21 means and sigmas of the missing mass are plotted for each sector for identified  $ep \rightarrow ep\pi^0$  events, before and after corrections. The constants for the electron and the proton momentum corrections

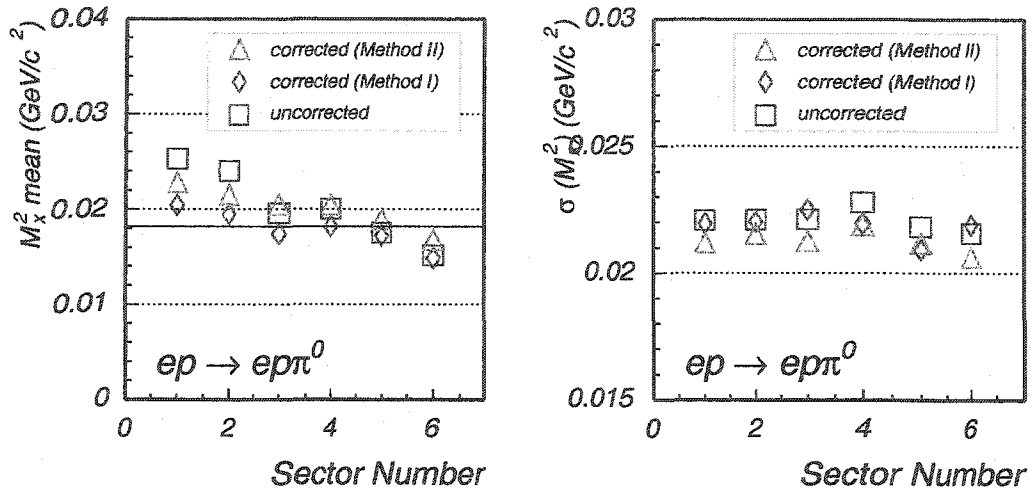


Figure 4-22: The mean and sigma of the  $\pi^0$  peak as a function of electron sector in CLAS.  $\pi^0$  events are selected from  $ep \rightarrow ep\gamma\gamma$  events with cut on  $2\gamma$  invariant mass around pion mass. The mean (a) and sigma (b) for each sector are plotted before corrections, and after corrections with two different methods described in this chapter.

derived using both methods can be found in the appendix. The correction were applied to the electron and the proton momentum to eliminate any sector dependence of mean and sigma values for photon and pion peaks. In the final analysis the corrections derived from the second method were used.

# CHAPTER 5

## DVCS ANALYSIS

### 5.1 Kinematics

The data from the e1d run period were sufficient to allow measurements of the beam spin asymmetry in several kinematical bins. Previous experiments from CLAS and HERMES measured the asymmetry for one integrated bin in  $Q^2$  only. In this section the kinematics of the presented data (e1d) is discussed. The kinematical coverage of the e1d data set is shown in Figure 5-1. In Figure 5-1 (a) the  $Q^2$  versus  $x_B$  distribution is plotted. The lines in the plot indicate the  $Q^2$  bins used for the extraction of the beam spin asymmetries in this study. In Figure 5-1 (b) the distribution of  $Q^2$  is plotted versus  $t$ . The regions selected by rectangles correspond to data selected in the three  $Q^2$  (red) and the three  $t$  (blue) bins. For each of these  $Q^2$  and  $t$  bins the missing mass square distribution in the reaction  $ep \rightarrow epX$  were subdivided into 11  $\phi_{qp}$  bins. Where  $\phi_{qp}$  is the azimuthal angle between electron and proton scattering plane. Fit to the line shape of the missing mass squared distribution for each  $Q^2$ ,  $t$  and  $\phi_{qp}$  bin have been done for positive and negative helicities of the electron beam, and for the helicity sum.

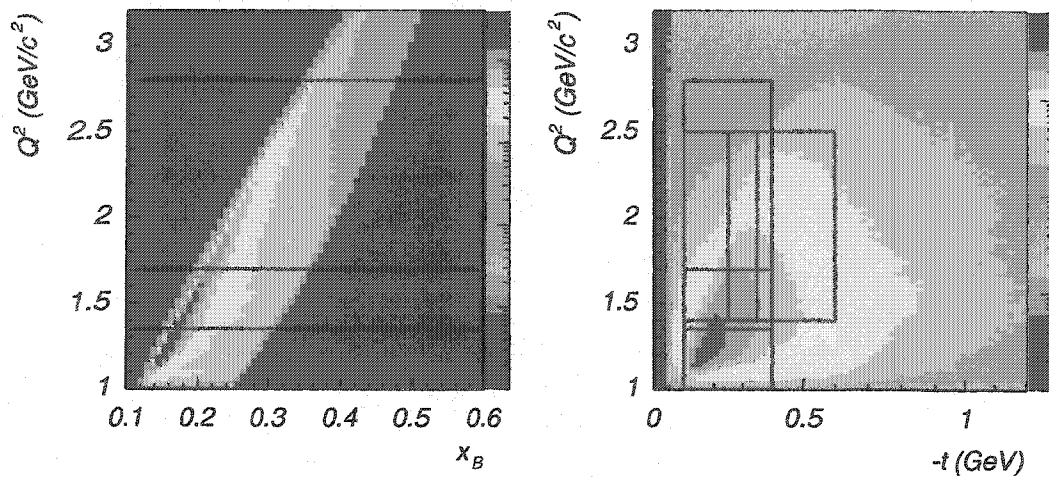


Figure 5-1: The kinematical coverage of the eld data set. (a) the  $Q^2$  versus  $x_B$  distribution is shown with  $Q^2$  bin divisions. (b)  $Q^2$  versus  $t$  distribution is shown, the boxes indicate the kinematical bins used for these analysis.

## 5.2 Missing Mass Technique

The main challenge in the DVCS analysis from the existing CLAS electro-production data is the separation of a single photon and more than one photon, mostly  $\pi^0$ , events in the reaction  $ep \rightarrow epX$ . In the kinematics of the DVCS analysis CLAS resolution on missing mass is not sufficient to separate cleanly these two final states (see Figure 5-2). For the separation of the  $ep\gamma$  and  $ep\gamma\gamma(\pi^0)$  final states a fit to the line shape of the missing mass squared ( $MM^2$ ) distribution is used. In the kinematical range of interest three types of processes contribute to the missing system "X": 1) production of a real photon; 2)  $\pi^0$  production, and 3) the radiative processes like  $ep\gamma_R\gamma$  or  $ep\gamma_R\pi^0$ , where  $\gamma_R$  is the photon radiated by the incoming or outgoing electron. It was assumed that the missing mass squared distributions corresponding to the single photon and the  $\pi^0$  have a Gaussian shape, and the radiative background has a smooth polynomial shape. A sum of two Gaussian and

a polynomial function was used in the fit:

$$F = N_\gamma \cdot G_\gamma + N_{\pi^0} \cdot G_{\pi^0} + P_3 \cdot Pol_3 \quad (5.1)$$

where  $N_\gamma$  and  $N_{\pi^0}$  are the number of single photon and pion final states under the missing mass peak respectively, and are the parameters for the final fit.  $P_3$  is the relative magnitude of the background. The shape of the background is determined by fitting the tails of missing mass squared distribution, and  $P_3$  is a parameter for the final fit. The mean and sigma of  $G_\gamma$  and  $G_{\pi^0}$  are determined from identified  $ep \rightarrow e'p$  and  $ep \rightarrow e'p\pi^0$  events respectively, for particular kinematics. The radiative elastic events from  $ep \rightarrow epX$  sample are chosen (see

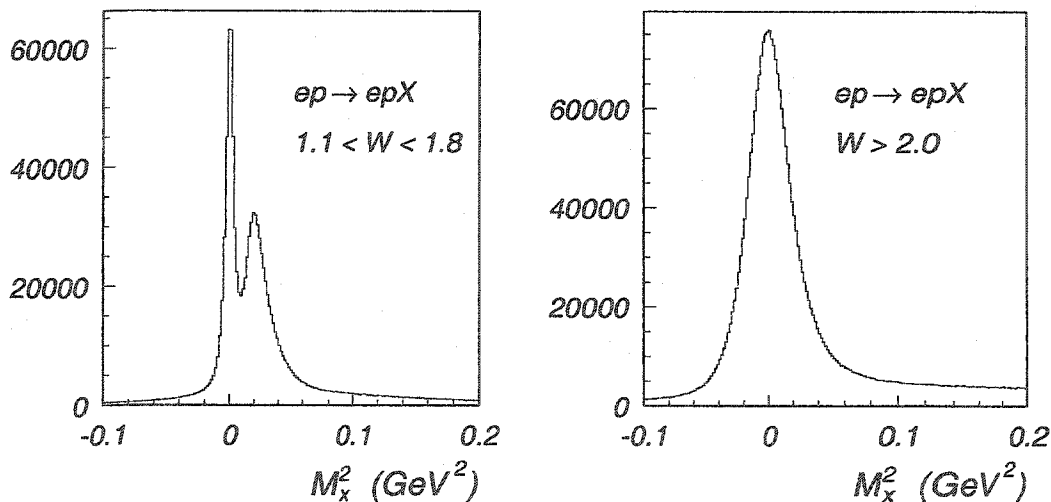


Figure 5-2:  $ep$  missing mass for  $ep \rightarrow epX$  for low  $W$  region (a) and for high  $W$  region (b).

Figure 4-15) to determine the photon peak parameters (e.g. mean ( $M_\gamma$  and sigma  $\sigma_\gamma$ )). To determine parameters of the pion peak,  $ep \rightarrow ep\pi^0$  events were selected from the  $ep \rightarrow ep\gamma\gamma$  sample. For events with both photons detected in the final state the invariant mass of two photons was calculated and cuts around  $\pi^0$  mass were applied to the invariant mass (see Figure 4-18). The resulting  $ep$  missing mass, after the cuts on the 2 photon invariant

mass, was fitted to determine the pion peak parameters (e.g.  $M_{\pi^0}$  and  $\sigma_{\pi^0}$ ). The missing

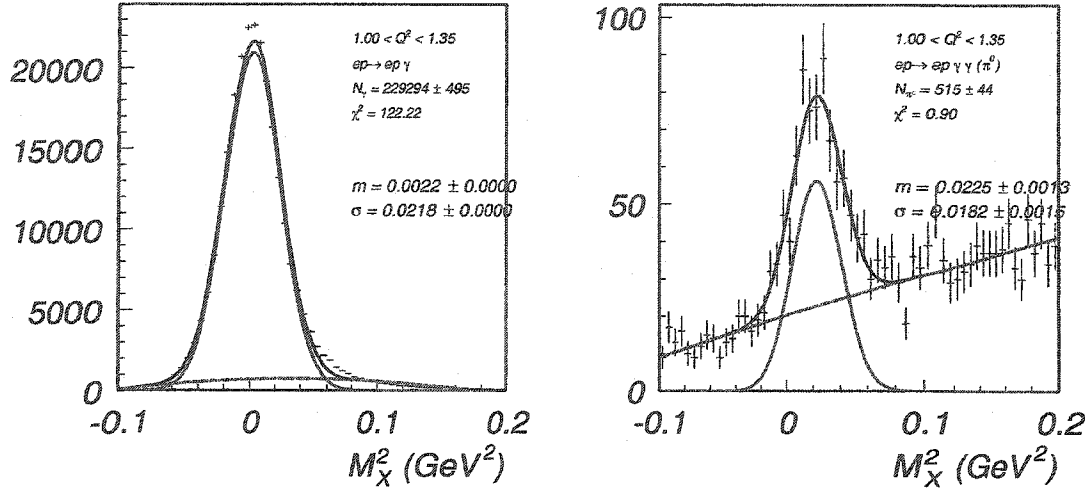


Figure 5-3: Extraction of  $G_\gamma$  (on the left) and  $G_{\pi^0}$  (on the right) Gaussian function parameters are done by fitting corresponding final states with Gaussian plus polynomial function.

mass squared distributions of radiative elastic and pion production events were fitted with a Gaussian function plus a polynomial function for background:

$$F(M_x^2) = A \cdot G_{\gamma(\pi^0)}(M, \sigma) + POL_3 \quad (5.2)$$

where fit parameter  $A$  is amplitude of the Gaussian function,  $M$  is the mean value, and  $\sigma$  is the standard deviation of the Gaussian,  $POL_3$  is a third degree polynomial to describe the background. The parameters for photon and pion Gaussian functions were determined for each  $Q^2$  and  $t$  bin separately, and then were used in the fit, with Eq.(5.1), to the missing mass squared distribution of  $ep$  in that particular kinematical bin.

Examples of these fits for one particular kinematical bin can be seen in Figure 5-3. In (a) the fit to the  $ep$  missing mass squared distribution for radiative elastic events is shown for one of the kinematical bins with determined mean and sigma values, and in (b) the fit

to the  $ep$  missing mass squared distribution is shown for identified pion production events.

### 5.2.1 Fit to the $M_x^2$ distributions

The individual distributions of missing mass square in each kinematical bin were fitted with function in Eq.(5.1) to obtain the number of photon and pion final states for each helicity state, and for the sum. The shape of background was fixed from the fit to the end point of the missing mass distribution for histograms containing both negative and positive helicity events. In Figure 5-4 an example of these fits is shown. In (a) the background shape

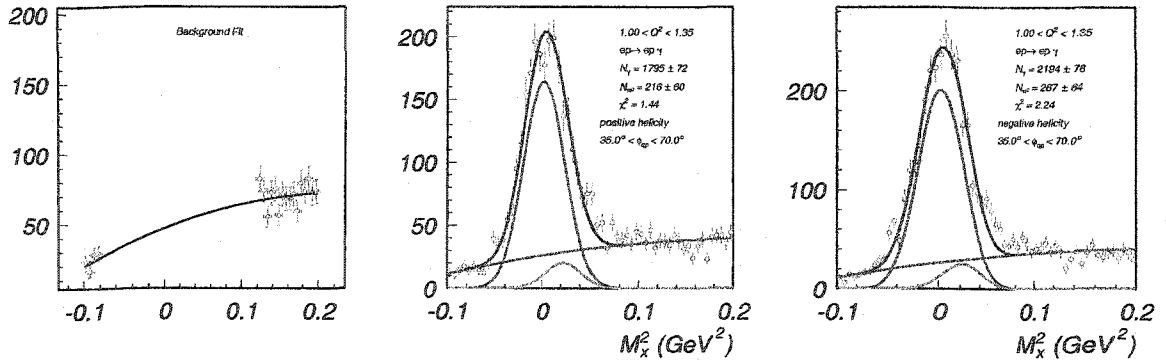


Figure 5-4: Example of fits for one  $\phi_{qp}$  bin. a) the background fitted to the distribution end points, b) fit to positive helicity events to extract number of  $\gamma$  and  $\pi^0$  under missing mass peak, c) fit to negative helicity.

is fitted with a polynomial function, in (b) the missing mass distribution for positive helicity events is fitted with function in Eq.(5.1) with fixed background shape and the Gaussian functions of photon ( $G_\gamma$ ) and pion ( $G_\pi$ ) missing mass distributions are obtained from the fit to the missing mass squared distributions of identified  $ep \rightarrow ep\gamma$  (Bethe-Heitler) and  $ep \rightarrow ep\gamma\gamma(\pi^0)$  final states (see Figure 5-3). For different  $Q^2$  bins the angular distributions of electron and proton angles vary, and the width of the photon and pion peak vary from one bin to another. The resolution shows sensitivity to the proton polar angle. Since

the magnitude of the magnetic field in CLAS changes with the polar angle, the resolution of reconstructed particle momentum slightly varies with polar angle. The electrons are registered in the forward direction with polar angles  $18^\circ - 55^\circ$ , while protons have wider range of angular distribution, hence the missing mass resolution becomes more sensitive to the proton polar angle. For a particular  $Q^2$  bin, the average (integrated over angular range) missing mass square peak parameters were used. For a particular  $Q^2$  bin, the extracted number of photon final states for negative ( $N_\gamma^-$ ) and positive ( $N_\gamma^+$ ) helicities in each  $\phi_{qp}$  bin where used to calculate the asymmetry as:

$$A_\phi = \frac{1}{P} \cdot \frac{N_\gamma^+ - N_\gamma^-}{N_\gamma^+ + N_\gamma^-} \quad (5.3)$$

where  $N_\gamma^+$  ( $N_\gamma^-$ ) is the number of photons reconstructed by fitting positive (negative) helicity missing mass squared distribution,  $P$  is the polarization measured during the run period ( $P = 67\% \pm 1.5\%$ ). The number of extracted photon final states for negative and positive

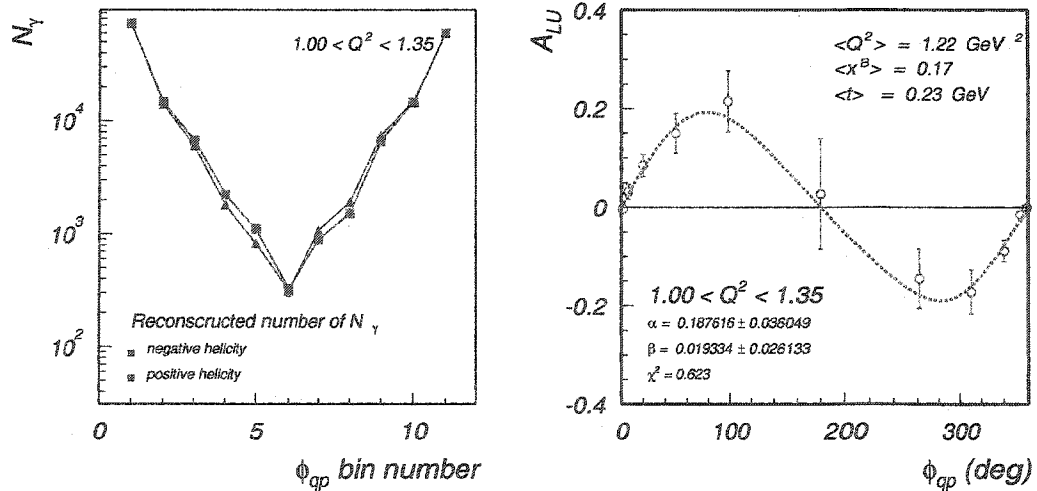


Figure 5-5: (a) number of reconstructed events in each  $\phi_{qp}$  bin for positive and negative helicity. (b) asymmetry for  $\langle Q^2 \rangle = 1.2944 \text{ GeV}^2$ ,  $\langle x_B \rangle = 0.176578$  and  $\langle -t \rangle = 0.240303 \text{ GeV}$  with Eq.(5.4), obtained  $A_{LU} = 0.188 \pm 0.036$ .

helicities for a particular  $Q^2$  bin can be seen in Figure 5-5, where these numbers are plotted for each  $\phi_{qp}$  bin. Then the asymmetry dependence on azimuthal angle was fitted with function:

$$A_{LU} = \alpha \sin(\phi) + \beta \sin(2\phi) \quad (5.4)$$

to extract the first and second moment of asymmetry. In Figure 5-5 (b) the fit to azimuthal dependence can be seen for one particular  $Q^2$  bin. The extracted amplitudes are:  $\alpha = 0.187 \pm 0.036$  and  $\beta = 0.019 \pm 0.026$ , with kinematical variables  $\langle Q^2 \rangle = 1.29 \text{ GeV}^2/c^2$ ,  $\langle x_B \rangle = 0.176$  and  $\langle -t \rangle = 0.24 \text{ GeV}$ .

This procedure was performed for three  $Q^2$  bins and three  $t$  bins to obtain the  $Q^2$  and  $t$  dependences of beam spin asymmetries.

## CHAPTER 6

# SYSTEMATIC STUDIES OF THE ANALYSIS METHOD

The difficulty in this separation method is not the fit itself, but the fact that peaks of the missing mass squared distributions for the missing photon and  $\pi^0$  events are separated by approximately one standard deviation, and therefore any small systematic uncertainties in the CLAS resolution will directly affect the fit results. (This implies, that good momentum corrections are essential for such analysis). Here in this chapter we present studies performed to investigate the validity of the fit method. These studies were performed using simulated and the real data, by mixing events from a single photon and  $\pi^0$  productions.

### 6.1 Studies With Experimental Data

Use of the experimental data has two advantages: i) the missing mass distributions have real physical backgrounds; ii) the kinematics of selected events is the same as in the real analysis. As was mentioned above, the goal is to mix identified single  $\pi^0$  and single photon

events, and then reconstruct the number of each final state in the mixed sample by a fit to the missing mass distribution. To select  $\pi^0$  events from the experimental data the final

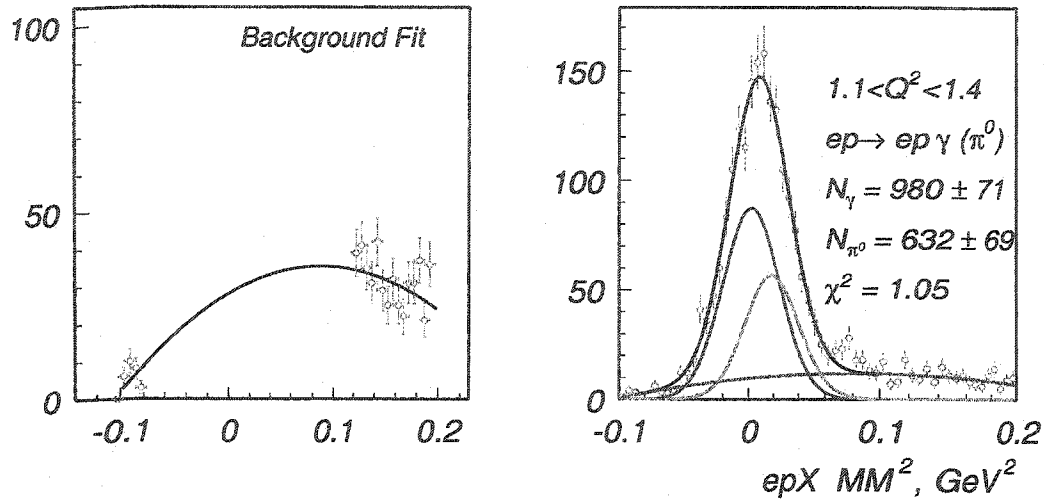


Figure 6-1: (a) fit to the end points of missing mass distribution for background extraction (b) Fit to missing mass with two Gaussian functions plus background to extract number of  $\gamma$ 's and  $\pi^0$  under missing mass peak.

state  $ep\gamma\gamma$  is studied. A cut on the invariant mass of  $2\gamma$ 's was used to select  $\pi^0$  events. In Figure 4-18 (a) the invariant mass of the two photons is plotted versus  $M_x^2$  of the  $(e'pX)$  in the reaction  $ep \rightarrow ep\gamma\gamma X$ . A large concentration of events around  $M_{\gamma\gamma} \simeq 0.135$  GeV and the  $M_x^2 \simeq 0.02$  GeV corresponds to  $\pi^0$ 's. A cut on the invariant mass of two  $\gamma$ 's was used to separate pion final states ( $0.08 < M_{\gamma\gamma} < 0.17$  GeV). For single photon final states, radiative elastic events are used in the reaction  $ep \rightarrow epX$ , when the incident electron radiates a photon before scattering. A cut on the missing momentum to be along the beam direction,  $(\Delta p_x^e/p)^2 + (\Delta p_y^e/p)^2 < 0.1$ , and a cut on the  $e'p$  scattering plane,  $178 < |\phi_e - \phi_p| < 182$ , are used to select events in this final state, see Figure 4-15. Figure 6-2 shows the missing mass squared distributions of  $(e'p)$  for each identified final state. Events are selected in the  $Q^2$  range from  $1.4$  GeV<sup>2</sup> to  $1.9$  GeV<sup>2</sup>. Fit to the spectra in Figure 6-2 are performed with

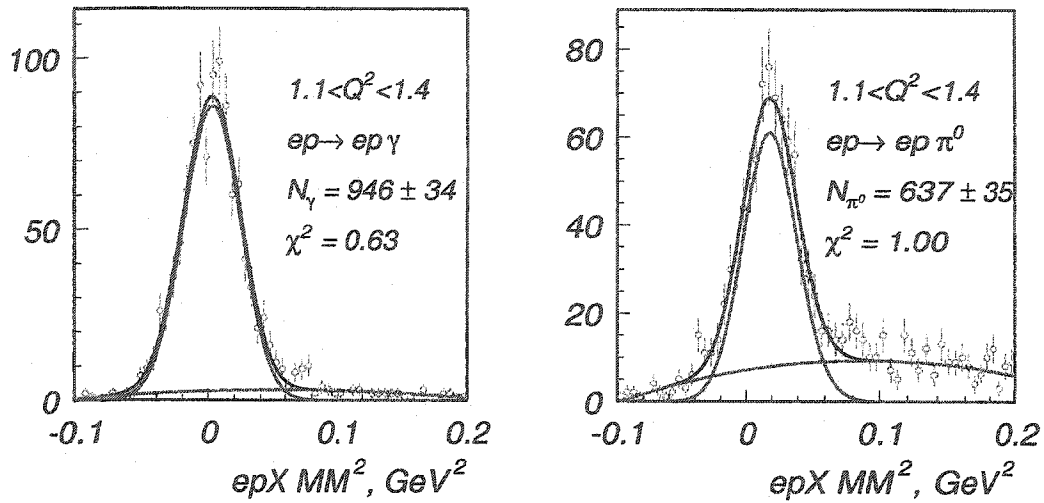


Figure 6-2: Fits to identified  $ep\gamma$  (a) and  $ep\pi^0$  (b) final states to determine the mean and sigmas for  $G_\gamma$  and  $G_{\pi^0}$ .

the function:

$$F = N_p G(m_p, \sigma_p) + Pol_3 \quad (6.1)$$

where  $N_p$  is the number of events and the  $G(m_p, \sigma_p)$  is a Gaussian function representing the  $M_x^2$  distribution of the given final state, with mean  $m_p$  and standard deviation  $\sigma_p$ . In these spectra the number of a single photon events is  $N_\gamma = 946$ , and the number of the  $\pi^0$ s is  $N_{\pi^0} = 637$ . The  $ep\gamma$  and  $ep\pi^0$  samples were mixed with different ratios. The resulting mixed distributions are fitted with a double Gaussian function to extract number of photon and pion final states under the missing mass squared distribution:

$$F = N_\gamma \cdot G_\gamma + N_{\pi^0} \cdot G_{\pi^0} + P_3 \cdot Pol_3 \quad (6.2)$$

The mean and the  $\sigma$  of  $G_\gamma$  and  $G_{\pi^0}$  were taken from fits to the distributions in Figure 6-2.

The shape of the background function,  $Pol_3$ , was determined by a fit to the end points of

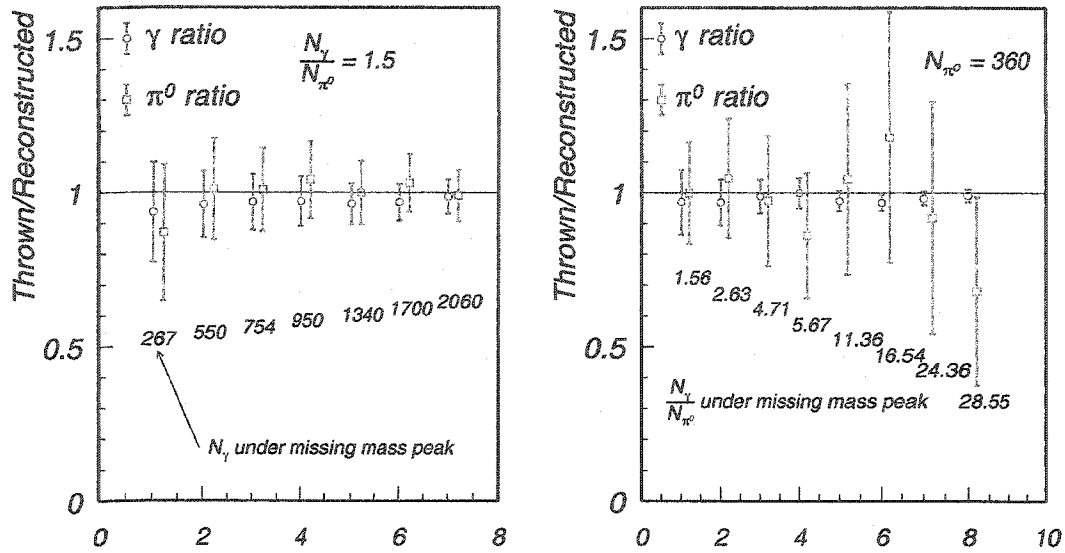


Figure 6-3: Ratios of reconstructed to thrown events for single photon and pion events, a) for constant  $N_\gamma/N_{\pi^0}$  ratio, b) for constant number of events in the mixed distribution.

the missing mass distribution of the mixed spectrum, Figure 6-1 (a). Figure 6-1 (b) shows the final fit to the missing mass distribution. The blue line on the graph corresponds to the background shape, the red line is the fitted Gaussian function for the photon events, and the green line is the Gaussian for the  $\pi^0$  events. In the final fit the fit parameters are the number of  $ep\gamma$  ( $N_\gamma$ ) and  $ep\pi^0$  ( $N_{\pi^0}$ ) events, and the magnitude of the background ( $P$ ).

Figure 6-1 shows a sample of one particular mixing ratio of the  $ep\gamma$  and the  $ep\pi^0$  events. Tests were performed to check how the fit method works for the different ratios of initial  $ep\gamma$  and  $ep\pi^0$  events, and for the different total statistics. Two cases were considered. In the first case, the mixing ratio of the  $ep\gamma$  and  $ep\pi^0$  events was kept constant, while the total number of events in the mixed distributions were changed. The ratio of the number of thrown events (number of events from the fit to the distributions of the identified final states) to the number of reconstructed events (from the fit to the mixed distributions) was

studied for different statistics. Figure 6-3 (a) shows this ratio for the different statistics (increasing from left to right). The ratio of two final states is  $\sim 1.5$ . The numbers each point in the plot correspond to is the number of  $ep\gamma$  events reconstructed from the fit to the radiative elastic events (the number of thrown  $ep\gamma$  events). In the second case the number of  $ep\pi^0$  events was kept constant in the mixed distribution, while the number of  $ep\gamma$  events was gradually increased. Figure 6-3 (b) shows the ratio of thrown and reconstructed events for increasing  $ep\gamma$  statistics. The number of  $ep\pi^0$  events during the mixing (reconstructed from the fit to the identified  $\pi^0$  final states) is 360. Numbers under each point show the ratios of the  $ep\gamma$  to  $ep\pi^0$  events. In the Tables 6.1 and 6.1 the results of fits to the different mixture of  $ep\gamma$  and  $ep\pi^0$  events, and the results of the fit to the data with constant ratio of  $N_\gamma/N_{\pi^0}$  are presented.

N	$N_\gamma/N_{\pi^0}$	$N_\gamma^{rec}/N_\gamma^{thr}$	ERR $N_\gamma^{rec}/N_\gamma^{thr}$	$N_{\pi^0}^{rec}/N_{\pi^0}^{thr}$	ERR $N_{\pi^0}^{rec}/N_{\pi^0}^{thr}$	$N_\gamma$
1	1.49162	0.936842	0.1627500	0.868932	0.2212930	267
2	1.48780	0.961471	0.1081510	1.010960	0.1650510	550
3	1.49901	0.969152	0.0908164	1.008020	0.1360180	754
4	1.49375	0.971545	0.0804433	1.040650	0.1248140	950
5	1.51755	0.963336	0.0667195	0.998869	0.1032390	1340
6	1.50750	0.968803	0.0599815	1.030000	0.0937543	1700
7	1.51248	0.986590	0.0554076	0.988389	0.0836257	2060

## 6.2 Tests With GSIM

Another set of tests were performed using GEANT [44] simulated data. Events were generated using a DVCS event generator [45] (available at CLASCVS *packages/generators/dvcs*).  $ep \rightarrow ep\gamma$  and  $ep \rightarrow ep\pi^0$  final states were generated in the kinematic region which is compatible with the one in the experiment (Figure 6-4). Then data were processed with the

Table 6.1: Results of the fit to the mixed distributions with constant mixing ratio.

N	$N_\gamma/N_{\pi^0}$	$N_\gamma^{rec}/N_\gamma^{thr}$	ERR $N_\gamma^{rec}/N_\gamma^{thr}$	$N_{\pi^0}^{rec}/N_{\pi^0}^{thr}$	ERR $N_{\pi^0}^{rec}/N_{\pi^0}^{thr}$	$N_{\pi^0}$
1	1.55647	0.969125	0.1057530	0.99725	0.165954	360
2	2.63361	0.968592	0.0748458	1.04611	0.193538	360
3	4.70523	0.988426	0.0542770	0.97319	0.211876	360
4	5.67493	0.999515	0.0491143	0.86019	0.203643	360
5	11.3609	0.974250	0.0331670	1.04310	0.307968	360
6	16.5372	0.968226	0.0271516	1.17857	0.406218	360
7	24.3636	0.981685	0.0224824	0.91666	0.376115	360
8	28.5455	0.991294	0.0207883	0.67977	0.305086	360

 Table 6.2: Results of the fit to the mixed distributions with constant number of  $\pi^0$ s.

GEANT simulator (GSIM) and reconstructed using RECSIS (CLAS event reconstruction program). The  $ep \rightarrow epX$  events from both samples were mixed together and then the fit procedure was performed (described in preceding section) to extract the number of  $ep \rightarrow ep\gamma$  and  $ep \rightarrow ep\pi^0$  events. The Gaussian parameters for the fits were derived from the fit to  $ep \rightarrow ep\pi^0$  and  $ep \rightarrow ep\gamma$  events. Examples of fits for one  $\phi_{qp}$  bin are shown on Figure 6-5. The red dots represent thrown distribution for single gamma events, and the red line is the result of the fit to the missing mass distribution. The green circles are the single pion distribution and the green line is the result of the fit. The black points represent mixed distributions. The fit to these points is performed with the function presented in Eq.(6.2). Final results of fits for all  $\phi_{qp}$  bins are presented in Figure 6-6. Figure 6-6 (a) shows the ratio of the number of  $ep \rightarrow ep\gamma$  events reconstructed before mixing to the number of  $ep \rightarrow ep\gamma$  events reconstructed by the fit to the mixed distribution. The crosses and circles represent the ratios for different helicities. The blue asterisks show the ratio of ratios for negative and positive helicities. As one can see from the plot the ratio of RECSIS reconstructed events to the number of events reconstructed by the fit is always less than one, this is due to the fact that some of the events get fitted as a part of the background. The important

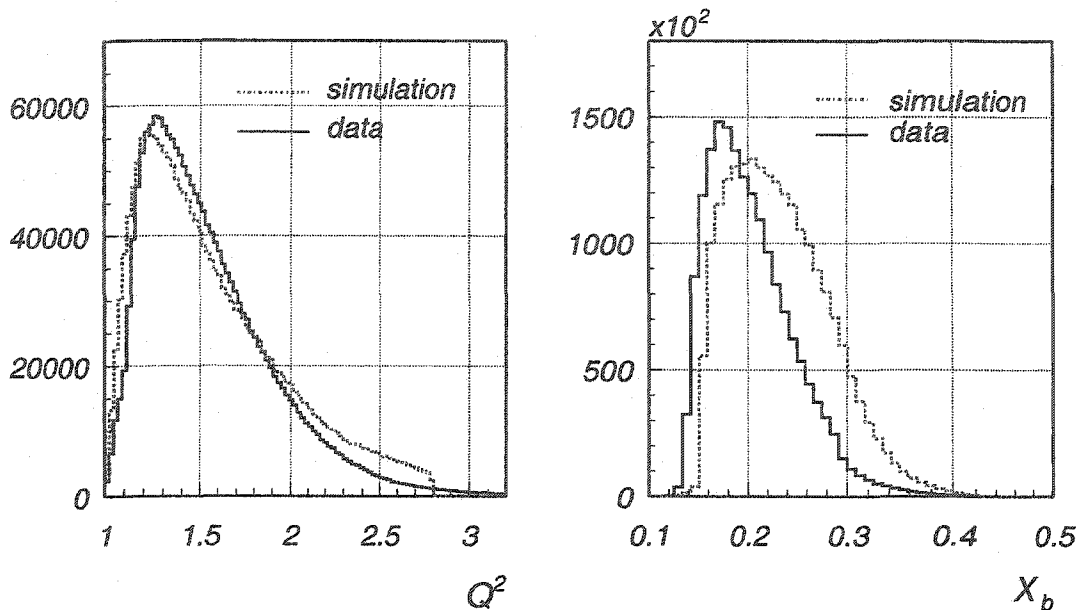


Figure 6-4: Simulated data kinematics compared with data.

information is contained in the points with an asterisks which show that for each  $\phi_{qp}$  bin the ratio of thrown to reconstructed events is the same for both helicities. Close to  $\phi_{qp} \sim 0^0$ , due to the statistics, fits do not perform as good as in other bins, but these bins do not play any significant role in the fitting. Figure 6-6 (b) shows the same results for  $ep \rightarrow ep\pi^0$  events. After determining the number of DVCS events for both helicities the asymmetry was calculated for each  $\phi_{qp}$  bin. Extracted asymmetry as a function of  $\phi_{qp}$  is shown in Figure 6-7. A fit to the points is performed using the function  $A = \alpha \sin\phi + \beta \sin 2\phi$ . Figure 6-7 represent the fit to the point from the simulated data. Solid curves are the fit to the points extracted by the fitting method described above.

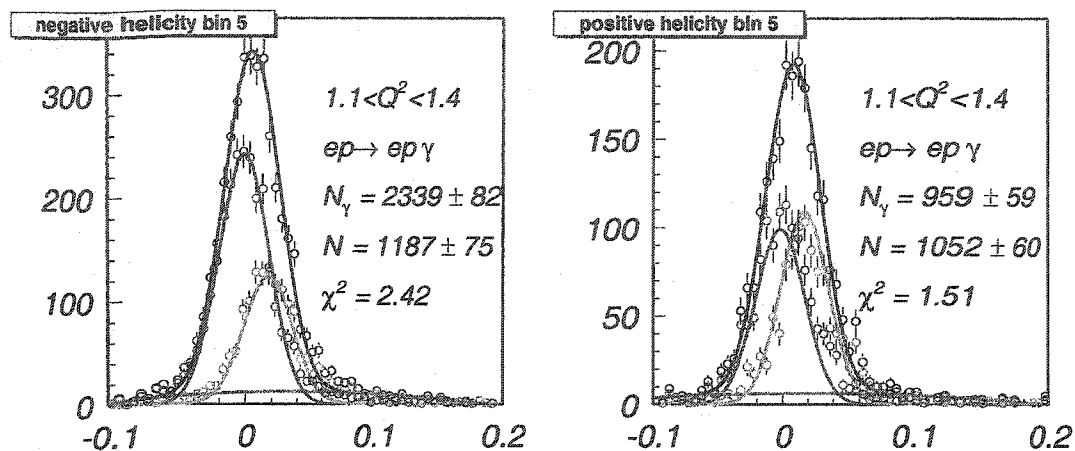


Figure 6-5: Missing mass squared distribution for negative (left) and positive (right) helicities fitted with two Gaussian plus background for on  $\phi_{qp}, Q^2$  bin. The black points represent mixed distribution and the fit to it.

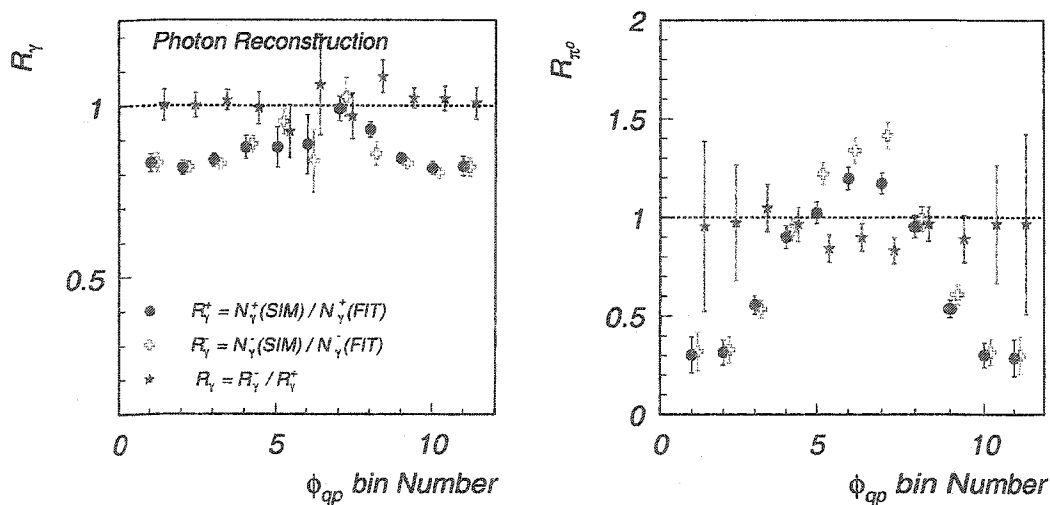


Figure 6-6: Reconstruction of single photon and single pion final states with double Gaussian fit. (a) the ratio of the reconstructed number of single photon events to the number of thrown events for positive (red circle) and negative (blue cross) helicities, and the ratio of negative to positive reconstruction efficiencies. (b) same ratios for number of reconstructed pions.

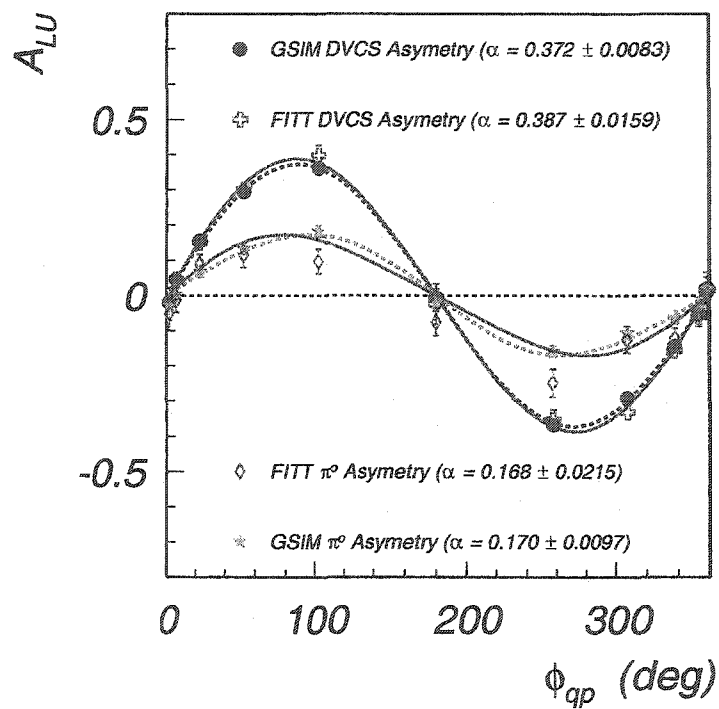


Figure 6-7: Extracted beam spin asymmetries for DVCS and  $\pi^0$  compared with asymmetry obtained by using missing mass fitting method. The obtained asymmetry is shifted from thrown for  $\sim 3\%$ .

### 6.3 Studies of asymmetries with missing mass cuts

Asymmetries can also be studied using cuts on the missing mass squared distributions around  $M_x^2 = 0$ . Although the main contribution to the event sample selected with such cuts will be the production of the a single photon, the contribution from  $\pi^0$  and radiative events will be difficult to estimate, and it will be kinematics dependent. (A typical width of the pion  $M_x^2$  distribution is  $\sim 0.02 \text{ GeV}^2$ , while the centroid is  $\sim 0.018 \text{ GeV}^2$ ). Tighter cuts will lower background contributions, but will impact the statistical accuracy. In this

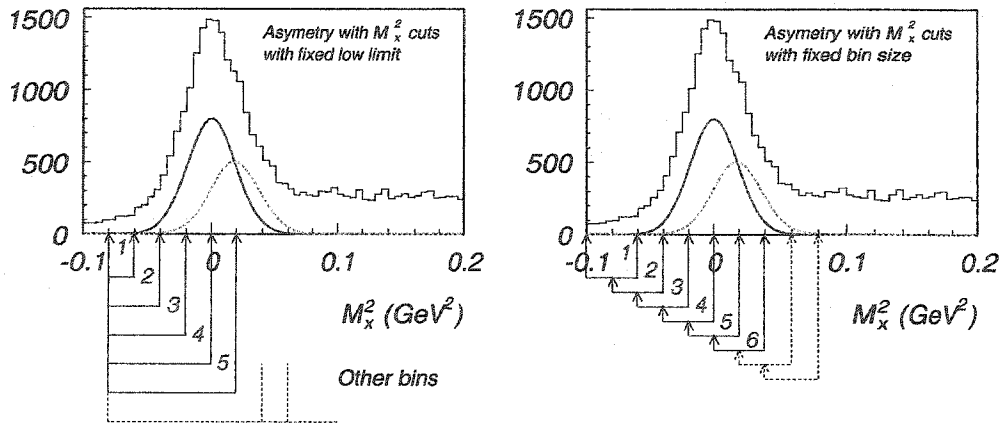


Figure 6-8: Diagram explaining cuts used on missing mass to calculate the asymmetry. The arrows show the cut on missing mass. The missing mass distribution is drawn, the *solid line* corresponds to the photon and *dashed line* to pion.

section we make a comparison of extracted asymmetries using the method of the fit to the line shape of the missing mass squared distributions with asymmetries calculated using cuts on the missing mass squared distributions. Two types of cuts for events selection were studied. In Figure 6-8 (a) bins of missing mass squared distribution in the case of cuts with fixed lower limit, at  $M_{x,Low}^2 = -0.08 \text{ GeV}^2$ , and variable upper limit ( $M_{x,High}^2$ ), with steps of  $\Delta M_x^2 = 0.04 \text{ GeV}^2$  are shown. The numbers on the graph corresponds to

the bin number, where asymmetry is calculated. The second type of cut is illustrated in

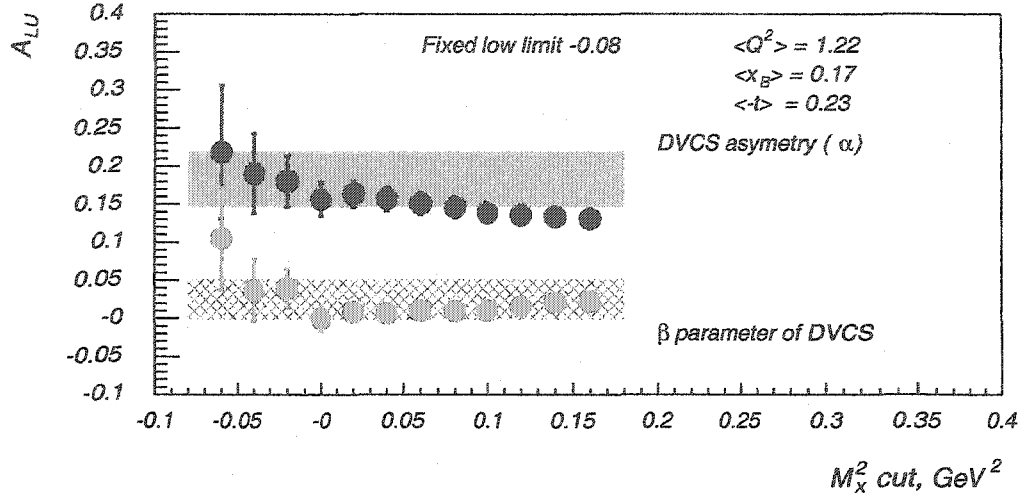


Figure 6-9: Asymmetry extracted using missing mass cut with fixed low limit. The points are placed at the high limit cut.

Figure 6-8 (b). In this case the bin size is fixed,  $M_{x,High}^2 - M_{x,Low}^2 = 0.04 \text{ GeV}^2$ , and the centroids of different bins are separated by  $0.02 \text{ GeV}^2$ . Again the numbers on the graph are the number of the bin where the asymmetry is extracted. Arrows pointing to the “X” axis on both graphs of Figure 6-8 show the range of missing mass squared were events are selected for that bin. In Figure 6-9 the extracted asymmetries for the case of selection of events in the bins of missing mass squared with fixed lower limit is presented ( $M_{x,Low}^2 = -0.08 \text{ GeV}^2$ ). Each point corresponds to one bin, and placed at the place of the  $M_{x,High}^2 \text{ GeV}^2$ . For example the second point on the graph at  $M_x^2 = -0.04 \text{ GeV}^2$ , is the asymmetry calculated using events in the missing mass squared range from  $-0.08$  to  $-0.04 \text{ GeV}^2$ . The fifth point placed at  $M_x^2 = 0$  is for the range  $-0.08$  to  $0 \text{ GeV}^2$ . Red points correspond to the  $\sin\phi$  moment of the asymmetry,  $\alpha$ , and the green points are the parameter  $\beta$  of the  $\sin 2\phi$  moment. The blue band is the asymmetry extracted using the fit method. As one expects the asymmetry calculated using missing mass cuts decreases

with an increase of the upper limit of the missing mass range, sine the contribution of  $\pi^0$  and the background increases. Figure 6-10 shows the results of extracted asymmetry

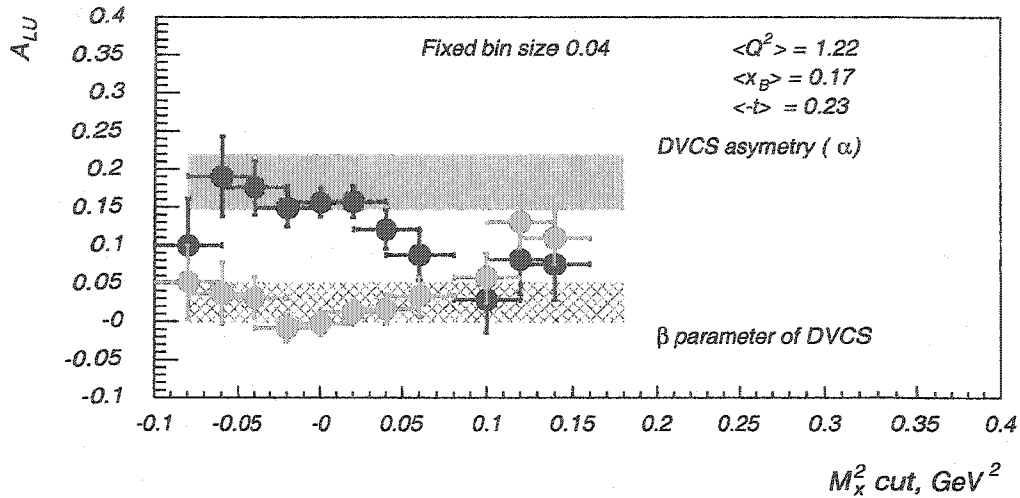


Figure 6-10: Asymmetry extracted using missing mass cut with fixed bin size in missing mass squared. The points are placed in the middle of the bin.

using the fixed bin width cut on the missing mass squared distribution (diagram shown on Figure 6-8 (b)). The asymmetry was extracted for several regions of the missing mass squared distribution with fixed bin size of  $0.04 \text{ GeV}^2$ . The points on the graph in Figure 6-10 are located in the middle of the bin, and the horizontal error bars indicate the cut region on the missing mass distribution. For example the third point on the graph, located at  $-0.04 \text{ GeV}^2$  is the asymmetry for events in the missing mass region from  $-0.06 \text{ GeV}^2$  to  $-0.02 \text{ GeV}^2$ , and the point located at  $0 \text{ GeV}^2$  (fifth point) is the asymmetry for region  $-0.02 \text{ GeV}^2$  to  $0.02 \text{ GeV}^2$ . One can see that for the lowest point on the missing mass axis (corresponding to the region  $-0.1$  to  $-0.06 \text{ GeV}^2$ ), that has very small contributions from photon and pion peaks, the asymmetry is non-zero. This indicates that the background has non-zero asymmetry, and if included in the photon peak, which happens when asymmetry is measured by a cut on the missing mass rather than by separating different contributions

(fit method), it may affect the extracted asymmetry for DVCS. This speaks in favor of using the fitting method developed in this work for extracting the DVCS asymmetries. One would expect the asymmetry to rise along the missing mass axis, since when moving toward the “0” the contribution from the photon peak becomes more significant. Toward the positive side of the missing mass the asymmetry rises and overlaps (within the error bars) with the value for the asymmetry extracted using the fit method, then slowly approaches to the pion asymmetry, as the pion peak contribution becomes more and more significant. These tests show a consistency between the asymmetry extracted using a fit and the asymmetry measured using a cut on the missing mass distributions. The method of fitting the line shape of the missing mass squared distribution is an effective way to get rid of contributions from background processes, and provides more clean method of asymmetry measurements.

## 6.4 Conclusions

Overall, the tests show consistency of the obtained results. Test performed with data show persistence of the reconstruction of the number of single photon production states from data mixed in different proportions, with a systematic shift below 5%. Tests with simulation show some systematic shifts of  $\sim 5\%$  in reconstructing the number of photons under the missing mass square peak. These systematic shifts appear to be the same for both negative and positive helicities and they do not affect the final measured asymmetry significantly. The asymmetry extracted from simulated data by using the fit method shows only  $\sim 3\%$  systematical shifts.

The extracted asymmetries were compared to asymmetries measured using cut on missing mass squared distribution around photon mass. The asymmetries extracted with both methods agree, but in the asymmetries measured using cuts on missing mass one has to be

sure eliminate  $\pi^0$  contribution by making very tight cuts, which increases statistical errors. The asymmetry measurement using fitting technique eliminate the contribution from  $\pi^0$  without affecting photon statistics, hence provide much cleaner measurements of beam spin asymmetries.

# CHAPTER 7

## RESULTS AND CONCLUSIONS

### 7.1 Results

The single spin asymmetry in the deeply virtual electro-production of a real photon on the proton is studied using a longitudinally polarized electron beam at  $E = 4.8$  GeV. The azimuthal angular dependence of the asymmetry is extracted in a wide range of kinematics. The asymmetry is calculated as:

$$A_{LU} = \frac{1}{P} \cdot \frac{N^+ - N^-}{N^+ + N^-} \quad (7.1)$$

where  $N^{+(-)}$  are the number of  $ep \rightarrow ep\gamma$  events for a positive (negative) helicity state. A  $\phi_{qp}$  dependence of the  $A_{LU}$  is used to extract the  $\sin\phi$  and  $\sin 2\phi$  moments for three  $Q^2$  and three  $t$  bins. In each  $Q^2$  and  $t$  bin eleven bins of  $\phi$  have been used. Due to the insufficient missing mass resolution of CLAS in the high transferred momentum range, it is impossible to separate events with a single photon final state from competing background processes on an event-by-event bases. The number of  $ep \rightarrow ep\gamma$  events were extracted using a fit to

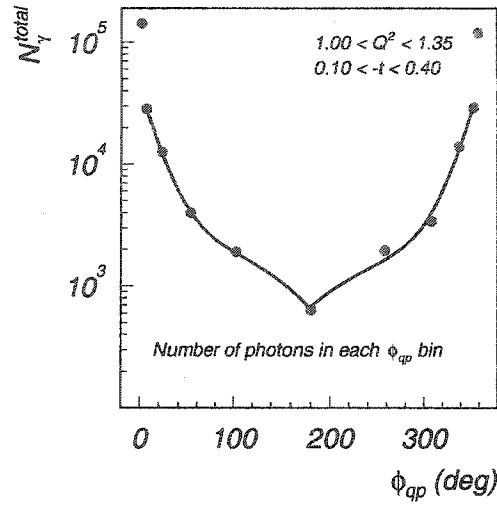


Figure 7-1: Fit to the number of photon final states in each  $\phi_{qp}$  bin for bin centering. The two halves of azimuthal distributions are fitted separately.

the line shape of the missing mass squared distributions (described in chapters 5 and 6) for both helicities, and for the helicity sum, at each kinematical bin.

The sum of the events with a photon final state ( $N_S$ ) was used to center the azimuthal angle bin. The  $N_S$  as a function of  $\phi_{qp}$  was fitted with a function:

$$f(N_S) = a_1 - a_2 \cdot e^{a_3 \cdot (a_4 - \phi_{qp})} - a_5 \cdot e^{a_6 \cdot (a_7 - \phi_{qp})} \quad (7.2)$$

where  $a_i$  are free parameters to the fit and  $\phi_{qp}$  is the azimuthal angle between electron and hadron scattering planes. A fit for one of the  $Q^2$  bins is shown in Figure 7-1. Then the mid point for each  $\phi_{qp}$  bin was calculated as:

$$\langle \phi_{qp} \rangle = \frac{\int_{\phi_{qp}^i}^{\phi_{qp}^{i+1}} \phi_{qp} d\phi_{qp} \cdot f(N_\gamma)}{\int_{\phi_{qp}^i}^{\phi_{qp}^{i+1}} d\phi_{qp} \cdot f(N_\gamma)} \quad (7.3)$$

The results of the fits and extracted number of photons in each  $\phi_{qp}$  in all  $Q^2$  and  $t$  bins can

be found in the Appendix. The azimuthal dependence of the asymmetry, calculated from the extracted number of photons under the missing mass square distribution, for each  $Q^2$  and  $t$  bin was fitted with the function:

$$A_{LU} = \alpha \sin(\phi) + \beta \sin(2\phi) \quad (7.4)$$

to extract the  $\sin(\phi)$  and  $\sin(2\phi)$  moments for each  $Q^2$  and  $t$  bins. The fits for three  $Q^2$  and  $t$  bins are shown in Figure 7-2 (for  $Q^2$  bins) and in Figure 7-3 (for  $t$  bins). In Figure 7-2

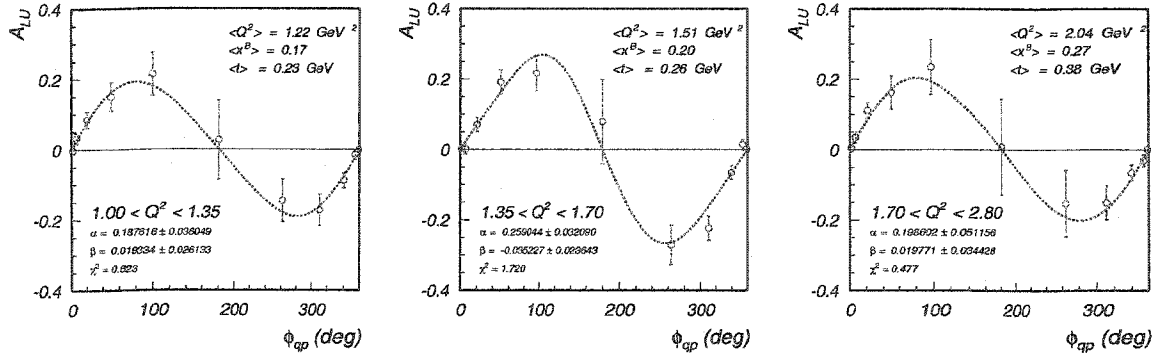


Figure 7-2: Asymmetry as a function of azimuthal angle fitted with Eq.(7.4) to extract  $\sin\phi$  moment for three  $Q^2$  bins.

and 7-3 the errors for the data points are calculated from the errors on the number of events with a photon final state obtained from the fit to the missing mass squared distribution.

The error is calculated as:

$$\Delta A_{LU} = A_{LU} \cdot \sqrt{\frac{(\Delta N^+)^2 + (\Delta N^-)^2}{(N^+ - N^-)^2} + \frac{(\Delta N^+)^2 + (\Delta N^-)^2}{(N^+ + N^-)^2}} \quad (7.5)$$

where  $\Delta N^+$  ( $\Delta N^-$ ) is the error of extracted number of photons of positive (negative) helicity. The numerical results of these analysis are presented in Tables 7.1 and 7.2,

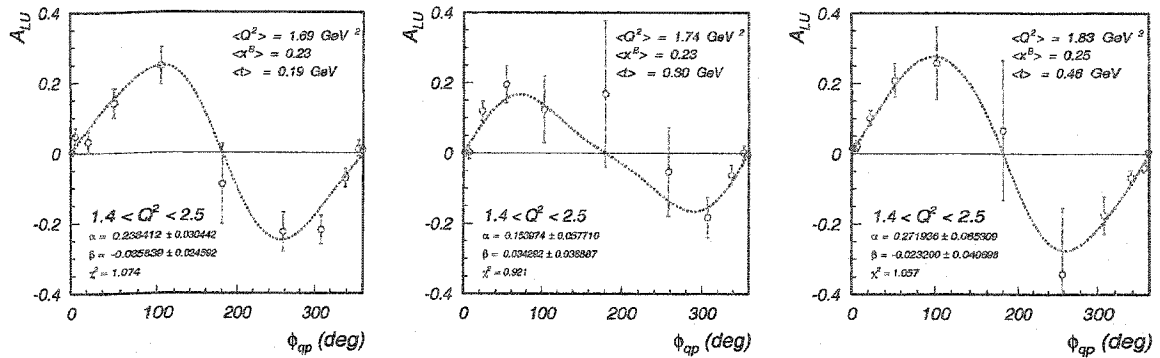


Figure 7-3: Asymmetry as a function of azimuthal angle fitted with Eq.(7.4) to extract  $\sin\phi$  moment for three  $t$  bins for integrated  $Q^2$  ( $1.4 < Q^2 < 2.5$  ( $\text{GeV}^2$ )).

$\langle Q^2 \rangle$	$\langle x_B \rangle$	$\langle -t \rangle$	$\alpha$	$\beta$
1.223	0.166	0.232	$0.188 \pm 0.036$ ( <i>stat</i> ) $\pm 0.0155$ ( <i>syst</i> )	$0.019 \pm 0.026$
1.509	0.203	0.263	$0.259 \pm 0.032$ ( <i>stat</i> ) $\pm 0.0166$ ( <i>syst</i> )	$-0.035 \pm 0.024$
2.041	0.275	0.381	$0.198 \pm 0.051$ ( <i>stat</i> ) $\pm 0.0140$ ( <i>syst</i> )	$0.020 \pm 0.034$

Table 7.1: Summary of obtained Beam Spin Asymmetries. Here  $\alpha$  and  $\beta$  are the first and second moment of the asymmetry amplitude fitted with function  $A_{LU} = \alpha \sin(\phi) + \beta \sin(2\phi)$ .

where the extracted asymmetries ( $\alpha$  and  $\beta$  parameters of the fit with Eq.(7.4)) for three  $Q^2$  and  $t$  bins are presented with the mean values of  $Q^2$ ,  $t$  and  $x_B$ . The  $Q^2$  and  $t$ -dependences of  $A_{LU}$  are presented in Figure 7-4. In Figure 7-4 the previous result of the DVCS beam spin asymmetry measured by CLAS [18] with 4.2 GeV initial electron beam is presented as well. The previously measured asymmetry is consistent with the measurements done within this analysis. As a result of this analysis a significant asymmetry was measured in deeply virtual Compton scattering. Within the error bars in  $Q^2$  and  $t$  dependence it is impossible to claim any  $Q^2$  or  $t$  dependences of the asymmetries. Further theoretical calculations are needed to compare with the measured dependences.

$\langle -t \rangle$	$\langle x_B \rangle$	$\langle Q^2 \rangle$	$\alpha$	$\beta$
0.192	0.226	1.690	$0.241 \pm 0.032$	$-0.027 \pm 0.026$
0.300	0.231	1.738	$0.144 \pm 0.064$	$0.047 \pm 0.043$
0.461	0.253	1.833	$0.276 \pm 0.072$	$-0.016 \pm 0.045$

Table 7.2: Summary of obtained Beam Spin Asymmetries. Here  $\alpha$  and  $\beta$  are the first and second moment of the asymmetry amplitude fitted with function  $A_{LU} = \alpha \sin(\phi) + \beta \sin(2\phi)$ .

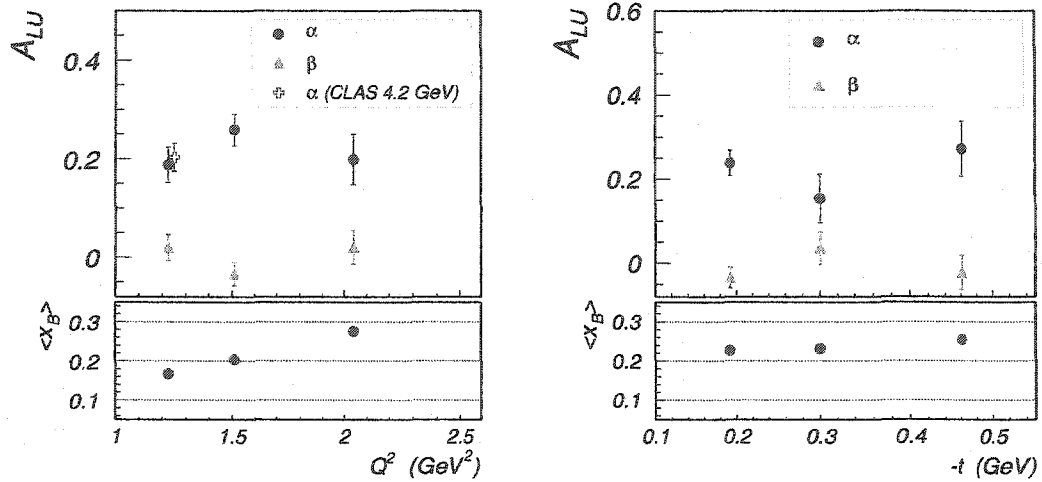


Figure 7-4: The  $Q^2$  (on the left) and  $t$  (on the right) dependence of DVCS asymmetries. The “cross” symbol is the asymmetry measured by CLAS with 4.2 GeV data.

## 7.2 Estimate of Systematic Error

For estimating the systematic error of measuring the asymmetry, three sources of systematic errors were considered. First, the systematic error due to the fitting procedure used in the analysis was estimated. The parameters to the final fit to the missing mass squared distribution are determined by fitting the missing mass squared distributions of identified single photon and pion final states. The average value of the peak mean and sigma are taken as fixed parameters in the fit procedure. The distribution of mean values and sigmas of photon and pion peaks are shown in Figure 7-5 for one kinematical bin. The

RMS of the distribution of each of these parameters was taken as error of their determination. The fitting procedure was performed using photon and pion peak parameters varied

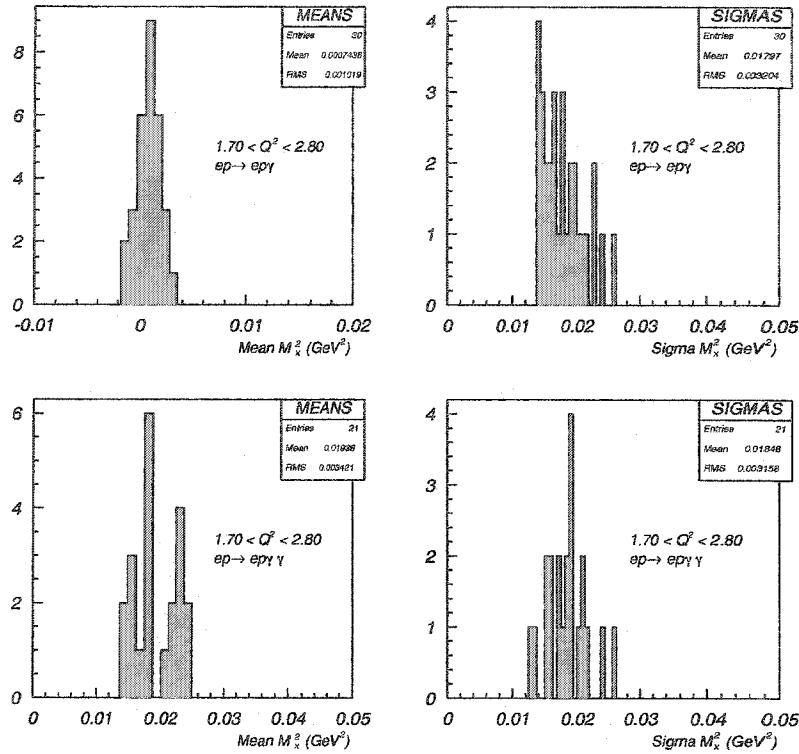


Figure 7-5: The mean and sigma value distribution for photon and pion peaks for one kinematical bin.

with all possible combinations within their determination error (one  $\sigma$ ). The resulting distributions of beam spin asymmetries for all possible variations of the parameters can be seen in Figure 7-6 for two  $Q^2$  bins. The RMS of these distributions were taken as the systematic error due the fitting procedure.

The second source of systematic errors is the error of determination for the beam polarization, which is calculated during the experiment with an accuracy of 1.5%. The error of determination of beam spin asymmetry from the simulated data was considered as the third

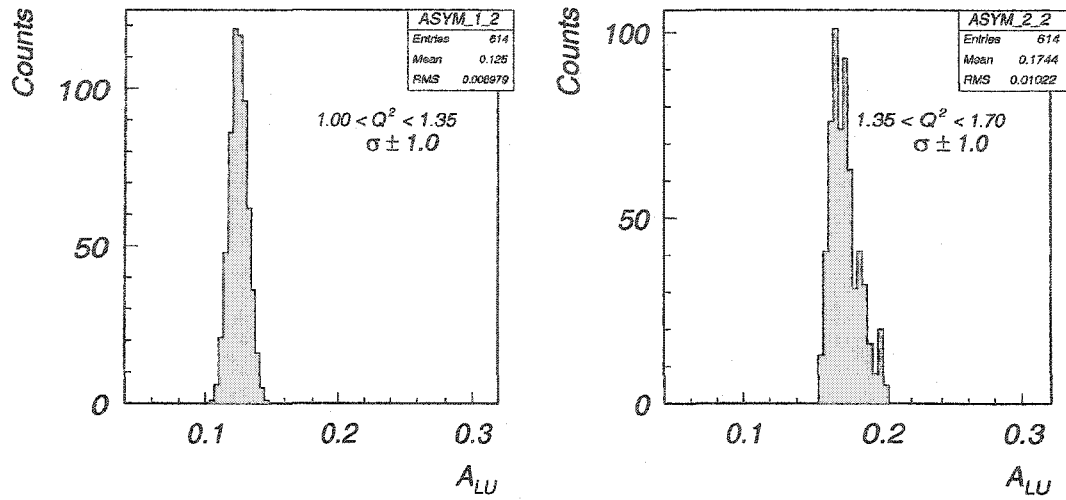


Figure 7-6: Systematic error estimation. The fits to the missing mass squared distributions were performed for using mean and sigma values for photon and pion peaks varied within the error of their determination.

source of systematic errors. The studies with simulated data showed that the asymmetry was extracted with an accuracy of about 5%. The total systematic error was calculated as:

$$\Delta A_{LU}^2 = (A_{+-} \cdot 0.05)^2 + (A_{+-} \cdot F_{fit})^2 + \Delta P^2 \quad (7.6)$$

where  $A_{+-}$  is the fit to the azimuthal dependence of the ratio  $(N^+ - N^-)/(N^+ + N^-)$ ,  $F_{fit}$  is the relative error of the asymmetry due to the fitting method, and  $\Delta P$  is the error of beam polarization ( $\Delta P \sim 1.5\%$ ). The total calculated systematic error is included in the Table 7.1.

### 7.3 SUMMARY

The analysis presented in this thesis are the first measurement of the beam spin asymmetry in deeply virtual Compton Scattering for several kinematical bins. In this analysis the

asymmetry was extracted for the first time for three  $Q^2$  bins for one integrated  $t$  bin ( $0.1 < -t < 0.4 \text{ GeV}$ ), and for three  $t$  bins for one integrated  $Q^2$  bin ( $1.4 < Q^2 < 2.5 \text{ GeV}/c^2$ ).

These are important results for checking theoretical models.

The experiment was carried out using the CLAS detector in Hall-B at Jefferson National Accelerator Facility. In the experiment a longitudinally polarized electron beam was scattered off a 5cm long liquid hydrogen target, with a total luminosity of  $1.28 \text{ fm}^{-1}$ . The experiment was carried out during 02/04/2000-03/05/2000 in Hall B at Jefferson Lab. The detected final state  $ep \rightarrow e'pX$  at  $W > 2.0 \text{ GeV}$  was studied for beam spin asymmetry extraction. The main processes that contribute to  $e'p$  missing mass square distribution are single photo-production ( $ep \rightarrow e'p\gamma$ ), single pion production ( $ep \rightarrow e'p\pi^0 \rightarrow e'p\gamma\gamma$ ) and radiative background. Since the CLAS resolution at high  $W$  is not sufficient to separate the single photo-production events from single pion production events on an event-by-event basis, a fit to the line shape of the missing mass squared distribution was used to extract the number of events with a single photon or a single pion final state from the  $e'p$  missing mass squared distribution. The line shape of the  $e'p$  missing mass square distribution was fitted with two Gaussian functions using fixed mean and sigma for the photon and pion peaks and a smooth 3-rd degree polynomial for a background. These parameters to the fit were fixed from identified single photon (radiative elastic events) and single pion (from final state  $ep \rightarrow e'p\gamma\gamma$ ) reactions for the same kinematics. Then the asymmetry was calculated as a function of azimuthal angle ( $\phi_{qp}$ , is the angle between electron and hadron scattering planes), and was fitted with the function:  $A_{LU} = \alpha \sin(\phi_{qp}) + \beta \sin(2\phi_{qp})$  to extract the first and second moment of the asymmetry. Since the extraction of the asymmetry relies on the fitting method, tests were performed to verify the validity of the fits and to estimate systematical shifts of the measured asymmetries. A set of test was performed with real

data by mixing identified  $e/p\gamma$  and  $e/p\pi^0$  events, and then reconstructing the number of each final state by fitting the  $e'p$  missing mass squared distribution. Another set of tests was performed using simulated data. Events were generated in the same kinematics as data for DVCS and single pion production events. Then these events were processed with GSIM (GEANT simulation program for the CLAS detector), and the reconstructed events with a  $ep \rightarrow epX$  final state were analyzed to extract the asymmetry and compared with the generated DVCS asymmetry. The tests showed reasonable consistency in the reconstruction of the number of events with a single photon production final states under the missing mass squared distribution. The systematic shift in reconstructing the number of photons is the same for both positive and negative helicities, hence leading  $\sim 3\%$  systematic shifts in asymmetry measurements. The extracted asymmetries were compared to asymmetries measured using cuts on the missing mass squared distribution around the photon mass. The asymmetries extracted with both methods agree, but in the asymmetries measured using cuts on the missing mass one has to be sure to eliminate the  $\pi^0$  contribution by making very tight cuts, which increases statistical errors. The asymmetry measurement using the fitting technique eliminates the contribution from  $\pi^0$  without affecting photon statistics, and thus provides a much cleaner measurements of beam spin asymmetries.

# CHAPTER 8

## APPENDIX

### 8.1 MOMENTUM CORRECTIONS

#### 8.1.1 Electron Momentum Correction Constants

The following tables are the results of electron momentum correction derived from radiative elastic events (described in Correction section). Each sector is corrected separately for different momentum bins.

Sector 1					
$P_e$ (GeV)	$p_0$	$p_1$	$p_2$	$p_3$	$p_4$
0.5 – 0.7	9.9628e-01	4.4388e-04	7.2135e-06	5.9042e-08	3.0460e-08
0.7 – 0.9	9.9761e-01	3.7360e-04	1.2679e-05	-2.6811e-07	1.5935e-08
0.9 – 1.2	9.9872e-01	3.2912e-04	1.1537e-05	-3.0425e-07	1.1913e-08
1.2 – 1.6	9.9975e-01	2.5648e-04	6.7299e-06	-1.9143e-07	9.0140e-09
1.6 – 2.7	1.0001e+00	1.8698e-04	5.3837e-06	2.8607e-07	9.8399e-09

Sector 2					
$P_e$ (GeV)	$p_0$	$p_1$	$p_2$	$p_3$	$p_4$
0.5 – 0.7	1.1540e+00	-1.0544e-02	2.5903e-04	-2.8401e-06	1.2140e-08
0.7 – 0.9	1.3188e+00	-2.0956e-02	5.0705e-04	-5.4391e-06	2.2206e-08
0.9 – 1.2	1.3793e+00	-2.5101e-02	6.1498e-04	-6.6624e-06	2.7262e-08
1.2 – 1.6	1.2885e+00	-1.9568e-02	4.9266e-04	-5.4768e-06	2.2952e-08
1.6 – 2.7	1.1913e+00	-1.4578e-02	4.0516e-04	-4.9108e-06	2.2227e-08

Sector 3					
$P_e$ (GeV)	$p_0$	$p_1$	$p_2$	$p_3$	$p_4$
0.5 – 0.7	3.2986e+00	-7.5137e-02	9.2033e-04	-5.0277e-06	1.0367e-08
0.7 – 0.9	4.4414e+00	-1.1215e-01	1.3717e-03	-7.4810e-06	1.5377e-08
0.9 – 1.2	4.8126e+00	-1.2798e-01	1.6138e-03	-9.0678e-06	1.9167e-08
1.2 – 1.6	4.7759e+00	-1.2527e-01	1.5598e-03	-8.6444e-06	1.7997e-08
1.6 – 2.7	1.1456e+01	-3.4490e-01	4.2619e-03	-2.3383e-05	4.8059e-08

Sector 4					
$P_e$ (GeV)	$p_0$	$p_1$	$p_2$	$p_3$	$p_4$
0.5 – 0.7	2.3813e+01	-5.0713e-01	4.2328e-03	-1.5726e-05	2.1948e-08
0.7 – 0.9	3.9829e+01	-8.6558e-01	7.2385e-03	-2.6919e-05	3.7571e-08
0.9 – 1.2	3.0490e+01	-6.5664e-01	5.4871e-03	-2.0399e-05	2.8471e-08
1.2 – 1.6	1.9024e+01	-3.9885e-01	3.3141e-03	-1.2259e-05	1.7041e-08
1.6 – 2.7	1.1782e+01	-2.1923e-01	1.6632e-03	-5.5830e-06	7.0039e-09

Sector 5					
$P_e$ (GeV)	$p_0$	$p_1$	$p_2$	$p_3$	$p_4$
0.5 – 0.7	6.2040e+00	1.7087e-01	2.1163e-03	1.1715e-05	2.4424e-08
0.7 – 0.9	6.6518e+00	1.8341e-01	2.2429e-03	1.2254e-05	2.5224e-08
0.9 – 1.2	5.7939e+00	1.5565e-01	1.9029e-03	1.0384e-05	2.1339e-08
1.2 – 1.6	1.9289e+00	2.6227e-02	2.8117e-04	1.3682e-06	2.5663e-09
1.6 – 2.7	4.4530e+00	1.1589e-01	1.4647e-03	8.2468e-06	1.7413e-08

Sector 6					
$P_e$ (GeV)	$p_0$	$p_1$	$p_2$	$p_3$	$p_4$
0.5 – 0.7	9.3902e-01	-7.0387e-03	-2.2479e-04	-2.7913e-06	-1.2288e-08
0.7 – 0.9	1.2110e+00	1.2362e-02	2.8540e-04	3.0972e-06	1.3004e-08
0.9 – 1.2	1.0798e+00	3.3668e-03	5.6039e-05	5.2567e-07	2.3536e-09
1.2 – 1.6	1.4075e+00	2.6190e-02	6.3976e-04	7.0306e-06	2.9057e-08
1.6 – 2.7	1.5847e+00	3.7822e-02	9.1716e-04	9.8803e-06	3.9702e-08

### 8.1.2 Proton Momentum Correction Constants

Proton momentum correction functions derived from  $ep \rightarrow e\pi^+n$ .

Sector 1					
$\theta_p$ (deg)	$p_0$	$p_1$	$p_2$	$p_3$	$p_4$
0° – 20°	1.0055e+00	7.2580e-04	7.4634e-05	7.4007e-07	-7.2619e-08
20° – 26°	1.0051e+00	-2.4234e-04	-4.3813e-06	3.0516e-06	1.1749e-07
26° – 36°	1.0079e+00	-4.0325e-04	-2.6212e-05	1.3539e-06	1.0632e-07
36° – 48°	1.0087e+00	-5.5171e-04	-1.0646e-05	6.5179e-07	3.4862e-08
48° – 60°	1.0100e+00	-4.5127e-04	-1.2739e-05	-8.3065e-08	-1.8492e-11
60° – 72°	1.0093e+00	-7.7648e-04	4.2156e-05	1.0139e-06	-1.1232e-07
72° – 130°	1.0040e+00	5.4104e-05	3.3539e-05	-1.1400e-06	-7.8374e-08

Sector 2					
$\theta_p$ (deg)	$p_0$	$p_1$	$p_2$	$p_3$	$p_4$
$0^\circ - 20^\circ$	4.7837e-01	3.4708e-02	-8.3804e-04	8.6184e-06	-3.1284e-08
$20^\circ - 26^\circ$	1.6221e+00	-4.5681e-02	1.2444e-03	-1.4862e-05	6.5711e-08
$26^\circ - 36^\circ$	1.2306e+00	-1.6058e-02	4.3024e-04	-5.0893e-06	2.2253e-08
$36^\circ - 48^\circ$	8.8877e-01	8.9015e-03	-2.3039e-04	2.5537e-06	-1.0580e-08
$48^\circ - 60^\circ$	-1.3705e-02	6.9915e-02	-1.7477e-03	1.9089e-05	-7.7454e-08
$60^\circ - 72^\circ$	-3.6786e+00	3.2601e-01	-8.2727e-03	9.0979e-05	-3.6719e-07
$72^\circ - 130^\circ$	1.1434e+01	-7.4944e-01	1.9746e-02	-2.2572e-04	9.4561e-07

Sector 3					
$\theta_p$ (deg)	$p_0$	$p_1$	$p_2$	$p_3$	$p_4$
$0^\circ - 20^\circ$	1.6878e+01	-5.1925e-01	6.3574e-03	-3.4515e-05	7.0048e-08
$20^\circ - 26^\circ$	1.9388e+00	-2.7542e-02	3.0858e-04	-1.5579e-06	2.9588e-09
$26^\circ - 36^\circ$	-1.0728e+00	6.9914e-02	-8.7088e-04	4.7761e-06	-9.7737e-09
$36^\circ - 48^\circ$	-1.3044e+00	8.2179e-02	-1.0857e-03	6.3405e-06	-1.3849e-08
$48^\circ - 60^\circ$	-1.3001e+00	8.1049e-02	-1.0678e-03	6.2738e-06	-1.3889e-08
$60^\circ - 72^\circ$	1.5170e+03	-5.0324e+01	6.2417e-01	-3.4280e-03	7.0339e-06
$72^\circ - 130^\circ$	4.4524e+02	-1.4905e+01	1.8665e-01	-1.0341e-03	2.1391e-06

Sector 4					
$\theta_p$ (deg)	$p_0$	$p_1$	$p_2$	$p_3$	$p_4$
$0^\circ - 20^\circ$	-3.9971e+03	8.9631e+01	-7.5147e-01	2.7929e-03	-3.8829e-06
$20^\circ - 26^\circ$	2.0022e+02	-4.3563e+00	3.5679e-02	-1.2970e-04	1.7657e-07
$26^\circ - 36^\circ$	1.1821e+02	-2.5579e+00	2.0903e-02	-7.5799e-05	1.0289e-07
$36^\circ - 48^\circ$	2.3392e+01	-4.8699e-01	3.9748e-03	-1.4415e-05	1.9583e-08
$48^\circ - 60^\circ$	8.1474e+00	-1.5968e-01	1.3377e-03	-4.9572e-06	6.8295e-09
$60^\circ - 72^\circ$	5.4596e+01	-1.1900e+00	9.8872e-03	-3.6404e-05	5.0087e-08
$72^\circ - 130^\circ$	3.1499e+03	-6.9860e+01	5.7996e-01	-2.1354e-03	2.9424e-06

Sector 5					
$\theta_p$ (deg)	$p_0$	$p_1$	$p_2$	$p_3$	$p_4$
$0^\circ - 20^\circ$	1.5412e+01	4.8924e-01	6.2188e-03	3.5089e-05	7.4184e-08
$20^\circ - 26^\circ$	3.1265e+01	1.0561e+00	1.3781e-02	7.9707e-05	1.7244e-07
$26^\circ - 36^\circ$	1.9415e+01	6.4086e-01	8.3311e-03	4.7952e-05	1.0312e-07
$36^\circ - 48^\circ$	1.4132e+00	1.0064e-02	7.3428e-05	1.1219e-07	-3.4289e-10
$48^\circ - 60^\circ$	-2.5878e+00	-1.2359e-01	-1.6029e-03	-9.2394e-06	-1.9912e-08
$60^\circ - 72^\circ$	-3.0714e+00	-1.2598e-01	-1.4479e-03	-7.2901e-06	-1.3469e-08
$72^\circ - 130^\circ$	2.9394e+00	7.9784e-02	1.1712e-03	7.3843e-06	1.7049e-08

Sector 6					
$\theta_p$ (deg)	$p_0$	$p_1$	$p_2$	$p_3$	$p_4$
$0^\circ - 20^\circ$	1.3291e+00	1.2874e-02	1.6815e-04	8.4145e-07	1.8255e-09
$20^\circ - 26^\circ$	3.8599e+00	1.9139e-01	4.7899e-03	5.3029e-05	2.1901e-07
$26^\circ - 36^\circ$	2.8926e+00	1.2485e-01	3.0596e-03	3.2976e-05	1.3191e-07
$36^\circ - 48^\circ$	1.3621e+00	2.4387e-02	6.2760e-04	7.1856e-06	3.0554e-08
$48^\circ - 60^\circ$	7.1520e-01	-1.9589e-02	-4.7993e-04	-5.0600e-06	-1.9623e-08
$60^\circ - 72^\circ$	6.2044e-01	-2.7613e-02	-7.1483e-04	-7.9524e-06	-3.2395e-08
$72^\circ - 130^\circ$	2.1867e+00	8.1487e-02	2.0738e-03	2.3198e-05	9.6335e-08

### 8.1.3 $\pi^+$ momentum calculation for $ep \rightarrow e\pi^+n$ final state

As was discribed in the Corrections section the momentum correction for protons wehe derived from  $ep \rightarrow e\pi^+n$  final state. Here below the calculations leading to  $\pi^+$  momentum corrections are presented.

The incoming electron with energy  $E_0$  scatters on proton producing  $\pi^+$  and  $n$  in final state. From conservation of energy we have

$$E_0 + M_p = E_e + E_n + E_{\pi^+} \quad (8.1)$$

where  $M_p$  is the mass of proton,  $E_n$  energy of neutron and  $E_{\pi^+}$  is the energy of pion. From conservation of momentum:

$$\vec{P}_0 = \vec{P}_e + \vec{P}_{\pi^+} + \vec{P}_n \quad (8.2)$$

$$\vec{P}_n = \vec{q} - \vec{P}_{\pi^+}, \quad (8.3)$$

where  $\vec{q} = \vec{P}_0 - \vec{P}_e$

$$E_n = E_0 + M_p - E_e - E_{\pi^+} = A - E_{\pi^+}, \quad (8.4)$$

where we noted  $A = E_0 - E_e + M_p$

$$E_n^2 - \vec{P}_n^2 = M_n^2 \quad (8.5)$$

$$E_n^2 = (A - E_{\pi^+})^2 = A^2 - 2AE_{\pi^+} + E_{\pi^+}^2 \quad (8.6)$$

$$\vec{P}_{\pi^+}^2 = (\vec{q} - \vec{P}_{\pi^+})(\vec{q} - \vec{P}_{\pi^+}) = q^2 - 2qP_{\pi^+}\cos\theta_{q\pi^+} + P_{\pi^+}^2 \quad (8.7)$$

where  $\theta_{q\pi^+}$  is the angle between virtual photon and scattered pion. Then we have:

$$\begin{aligned} M_n^2 &= E_n^2 - P_{\pi^+}^2 = \\ &= A^2 - 2AE_{\pi^+} + E_{\pi^+}^2 - (q^2 - 2qP_{\pi^+}\cos\theta_{q\pi^+} + P_{\pi^+}^2) = \\ &= A^2 - 2AE_{\pi^+} + M_{\pi^+}^2 - q^2 + 2qP_{\pi^+}\cos\theta_{q\pi^+}, \text{ since } M_{\pi^+}^2 = E_{\pi^+}^2 - P_{\pi^+}^2 \end{aligned} \quad (8.8)$$

Now let  $B = M_n^2 - A^2 - M_{\pi^+}^2 + q^2$  and  $C = 2q\cos\theta_{q\pi^+}$  Then we have

$$B - CP_{\pi^+} = 2AE_{\pi^+} \quad (8.9)$$

If we take square of both sides of the equation we get:

$$B^2 - 2BCP_{\pi^+} + C^2P_{\pi^+}^2 = 4A^2(P_{\pi^+}^2 + M_{\pi^+}^2), \text{ where } E_{\pi^+}^2 = (P_{\pi^+}^2 + M_{\pi^+}^2) \quad (8.10)$$

combining different powers of  $P_{\pi^+}$  we get.

$$(C^2 - 4A^2)P_{\pi^+}^2 - 2BCP_{\pi^+} + (B^2 - 4A^2M_{\pi^+}^2) = 0 \quad (8.11)$$

From this quadratic equation momentum of  $\pi^+$  can be calculated.

## 8.1.4 Momentum Correction Constants for II Method

The second method of momentum corrections was based on the CLAS Note [41]. The same parameters were used to correct the electron and the proton momentum depending on the angle and the momentum of detected particle according to Eq.(4.8)and Eq.(4.9). There are 16 parameters for each sector (96 parameters in total). In Table 8.1 the momentum correction parameters are presented starting from Sector 1.

n	$p(n * 4)$	$p(n * 4 + 1)$	$p(n * 4 + 2)$	$p(n * 4 + 3)$
0	0.000206224	-0.00314129	-0.000356946	0.000276714
1	0.000124656	0.000740808	-3.4351e - 05	7.19325e - 05
2	0.000142226	-6.28554e - 05	0.000200156	-0.000356438
3	-0.000144468	7.45012e - 05	1.99767e - 06	0.00010262
4	3.29911e - 05	-0.000967491	-0.00597786	0.00093268
5	-0.000259782	0.00157144	-0.000198555	0.00131451
6	-0.000599667	-0.000106984	-0.000623001	-0.000299595
7	-0.000402391	0.00112838	-7.60136e - 05	-0.00330236
8	-0.00016482	0.00151583	-0.0040338	0.000182937
9	-0.00325323	-0.00148356	-0.00366388	0.0101046
10	-0.000277672	-0.00212975	0.000315966	-0.000969332
11	0.000395951	-0.00130818	-0.00463028	0.000729905
12	0.000378814	-0.000899985	-0.000402462	-0.000509156
13	-0.000613316	-0.00055973	-0.00019093	7.94119e - 05
14	-0.000610637	-0.000162078	0.00059594	-0.000745723
15	-0.000799857	-0.000254783	-0.000179239	-0.000190504
16	-9.03286e - 06	-0.000814072	-0.00443854	-0.000446658
17	-0.000602203	-0.000844449	0.000298725	0.00250694
18	-0.000314465	-0.00102092	-3.96193e - 05	-0.000302633
19	0.000522575	-0.00155581	7.22068e - 06	-5.5378e - 06
20	-3.01462e - 05	-0.000754801	-0.00230075	0.000107089
21	2.84447e - 05	0.00247647	-0.00653832	0.0112804
22	-0.0072137	0.0141478	0.00329304	-0.00554353
23	0.000327351	0.00155364	-0.0044896	-5.20087e - 05

Table 8.1: The momentum correction parameters derived using the second method of corrections described in the text. There are 16 parameters per sector (96 in total).

## 8.2 FIT RESULTS

### 8.2.1 Extracted number of photons

The following tables present extracted number of photon final states using double Gaussian fit for each  $\phi_{qp}$  bin for all three  $Q^2$  bins. Here  $N_\gamma^+$  ( $N_\gamma^-$ ) represents the number of photon final states under missing mass peak for positive (negative) helicity and  $\Delta N_\gamma^+$  ( $\Delta N_\gamma^-$ ) error returned by the fit. The  $N_\gamma^{tot}$  and  $\Delta N_\gamma^{tot}$  are the number of photon final states under missing mass square distribution fo helicity sum and the fit error, respectively. Each of the tables represent one  $Q^2$  bin for one intergated  $t$  (shown on the top of the table).

$1.0 < Q^2 < 1.35 \text{ GeV}^2 \text{ (} 0.1 < -t < 0.4 \text{ GeV)}$							
Bin	$\phi_{qp}$	$N_\gamma^+$	$\Delta N_\gamma^+$	$N_\gamma^-$	$\Delta N_\gamma^-$	$N_\gamma^{tot}$	$\Delta N_\gamma^{tot}$
0	1.5	72032	397	71544	397	143604	561
1	6.5	13924	194	14502	196	28431	276
2	22.5	5943	135	6650	140	12598	195
3	52.5	1795	72	2194	78	4003	107
4	102.5	820	52	1094	58	1921	78
5	180	310	33	321	34	627	47
6	257.5	1070	58	879	53	1959	79
7	307.5	1892	75	1498	68	3407	102
8	337.5	7346	142	6515	136	13857	197
9	353.5	14654	193	14349	192	29020	273
10	358.5	59677	368	59435	368	119124	521

$1.35 < Q^2 < 1.7 \text{ GeV}^2 \text{ (} 0.1 < -t < 0.4 \text{ GeV)}$							
Bin	$\phi_{qp}$	$N_\gamma^+$	$\Delta N_\gamma^+$	$N_\gamma^-$	$\Delta N_\gamma^-$	$N_\gamma^{tot}$	$\Delta N_\gamma^{tot}$
0	1.5	73399	399	73456	399	146857	564
1	6.5	14706	194	14702	196	29400	276
2	22.5	7404	146	8124	154	15529	213
3	52.5	2417	83	3124	92	5548	124
4	102.5	1256	65	1679	72	2946	97
5	180	318	38	353	38	664	54
6	257.5	1501	71	1038	62	2534	95
7	307.5	2991	90	2209	81	5209	122
8	337.5	8784	157	8034	151	16815	218
9	353.5	15338	197	15614	197	30959	278
10	358.5	66235	382	66251	383	132493	541

1.7 < $Q^2$ < 2.8 GeV <sup>2</sup> (0.1 < $-t$ < 0.5 GeV)							
Bin	$\phi_{qp}$	$N_\gamma^+$	$\Delta N_\gamma^+$	$N_\gamma^-$	$\Delta N_\gamma^-$	$N_\gamma^{tot}$	$\Delta N_\gamma^{tot}$
0	1.5	83818	501	84060	501	167899	709
1	6.5	15774	244	16486	247	32260	347
2	22.5	8596	193	9965	204	18557	281
3	52.5	2570	123	3193	134	5771	182
4	102.5	1169	96	1603	107	2772	144
5	180	500	65	505	65	1004	92
6	257.5	1269	107	1032	98	2301	145
7	307.5	3058	133	2494	120	5543	180
8	337.5	9839	209	8992	201	18835	290
9	353.5	15903	245	15232	242	31154	345
10	358.5	76578	481	76646	482	153240	681

Following tables are the results of the double Gaussian fits to missing mass square distribution for three  $t$  bins for one integrated  $Q^2$  (shown on the top of the table).

0.1 < $-t$ < 0.25 GeV (1.4 < $Q^2$ < 2.5 GeV/c <sup>2</sup> )							
Bin	$\phi_{qp}$	$N_\gamma^+$	$\Delta N_\gamma^+$	$N_\gamma^-$	$\Delta N_\gamma^-$	$N_\gamma^{tot}$	$\Delta N_\gamma^{tot}$
0	1.5	29686	301	29743	301	59427	426
1	6.5	7748	171	8251	175	16012	245
2	22.5	6196	160	6460	166	12662	231
3	52.5	2598	109	3142	118	5753	161
4	102.5	1609	89	2246	100	3888	135
5	180	565	58	501	57	1075	81
6	257.5	2098	100	1546	90	3629	135
7	307.5	3395	118	2523	107	5942	160
8	337.5	6918	168	6280	162	13198	234
9	353.5	7925	172	8049	172	15971	244
10	358.5	26287	287	26566	289	52839	407

0.25 < $-t$ < 0.35 GeV (1.4 < $Q^2$ < 2.5 GeV/c <sup>2</sup> )							
Bin	$\phi_{qp}$	$N_\gamma^+$	$\Delta N_\gamma^+$	$N_\gamma^-$	$\Delta N_\gamma^-$	$N_\gamma^{tot}$	$\Delta N_\gamma^{tot}$
0	1.5	51529	364	51518	364	103050	515
1	6.5	9391	171	9423	173	18837	244
2	22.5	4437	122	5209	131	9643	180
3	52.5	1261	68	1641	75	2903	101
4	102.5	544	51	643	55	1183	75
5	180	138	30	173	31	308	44
6	257.5	433	52	403	48	838	72
7	307.5	1462	74	1142	66	2611	99
8	337.5	5396	136	4965	130	10359	188
9	353.5	9739	173	9753	172	19489	245
10	358.5	46702	349	46475	348	93185	494

0.35 < -t < 0.6 GeV (1.4 < Q <sup>2</sup> < 2.5 GeV/c <sup>2</sup> )							
Bin	$\phi_{qp}$	$N_{\gamma}^{+}$	$\Delta N_{\gamma}^{+}$	$N_{\gamma}^{-}$	$\Delta N_{\gamma}^{-}$	$N_{\gamma}^{tot}$	$\Delta N_{\gamma}^{tot}$
0	1.5	79596	392	81178	394	160803	556
1	6.5	13401	175	13798	177	27200	249
2	22.5	5850	123	6701	130	12555	179
3	52.5	1298	63	1720	70	3032	95
4	102.5	406	44	575	50	977	67
5	180	152	30	166	30	338	43
6	257.5	316	47	198	42	531	64
7	307.5	1426	68	1126	61	2557	91
8	337.5	7135	134	6511	128	13646	186
9	353.5	14165	178	13437	174	27609	249
10	358.5	71109	373	71559	374	142678	529

### 8.2.2 Fit Figures

The following figures are the results of the fits to missing mass square distributions in each  $\phi_{qp}$  bin for three  $Q^2$  for both positive and negative helicities. In each plot the individual number of photon and pion events under missing mass square peak reconstructed by the fit is shown, also fits to the identified radiative elastic and pion production events are presented with the fits and the Gaussian parameters that were used in the final double Gaussian fit.

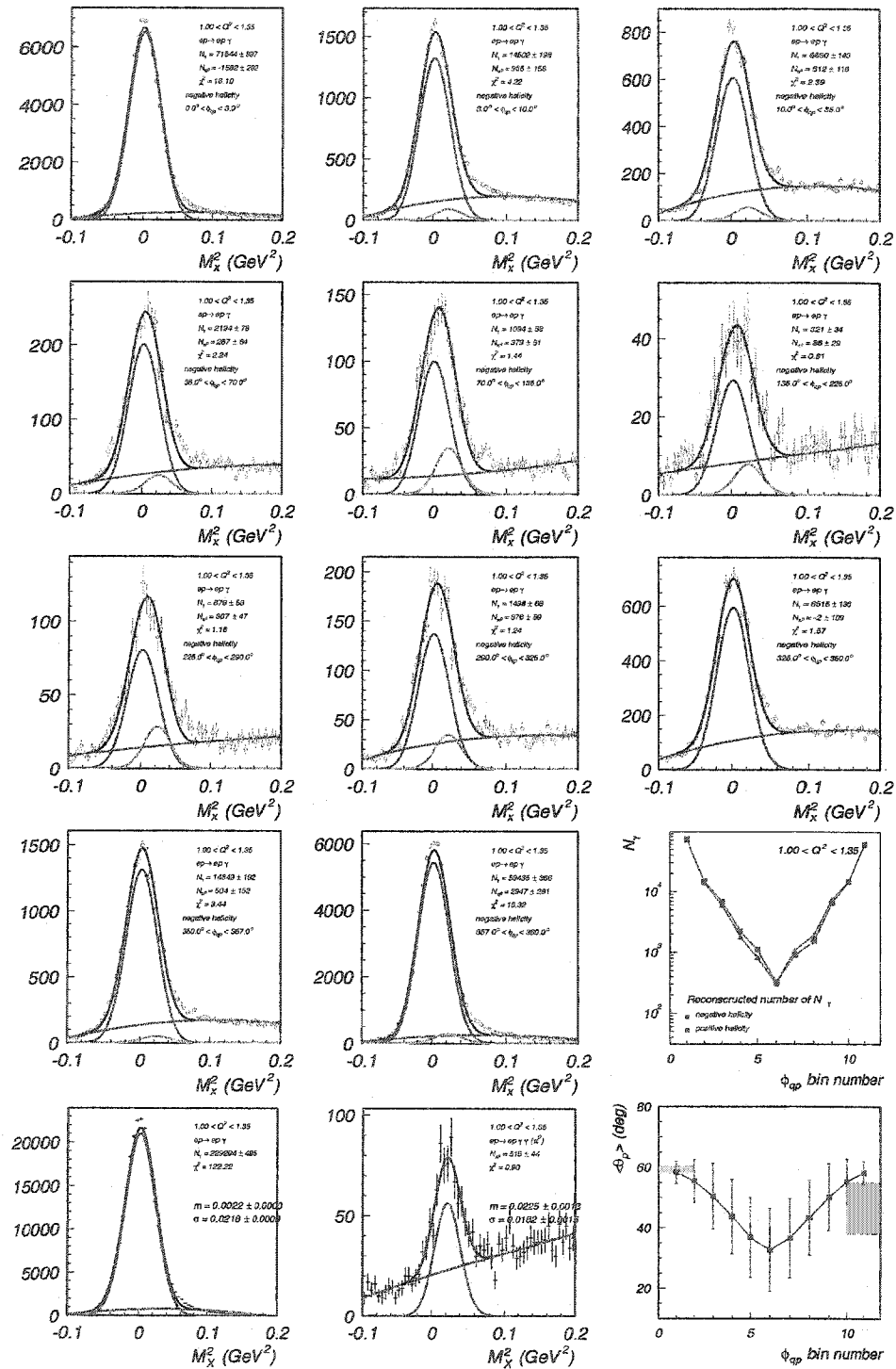


Figure 8-1: The fits to  $M_x^2$  for  $1.0 < Q^2 < 1.4$  (negative helicity).

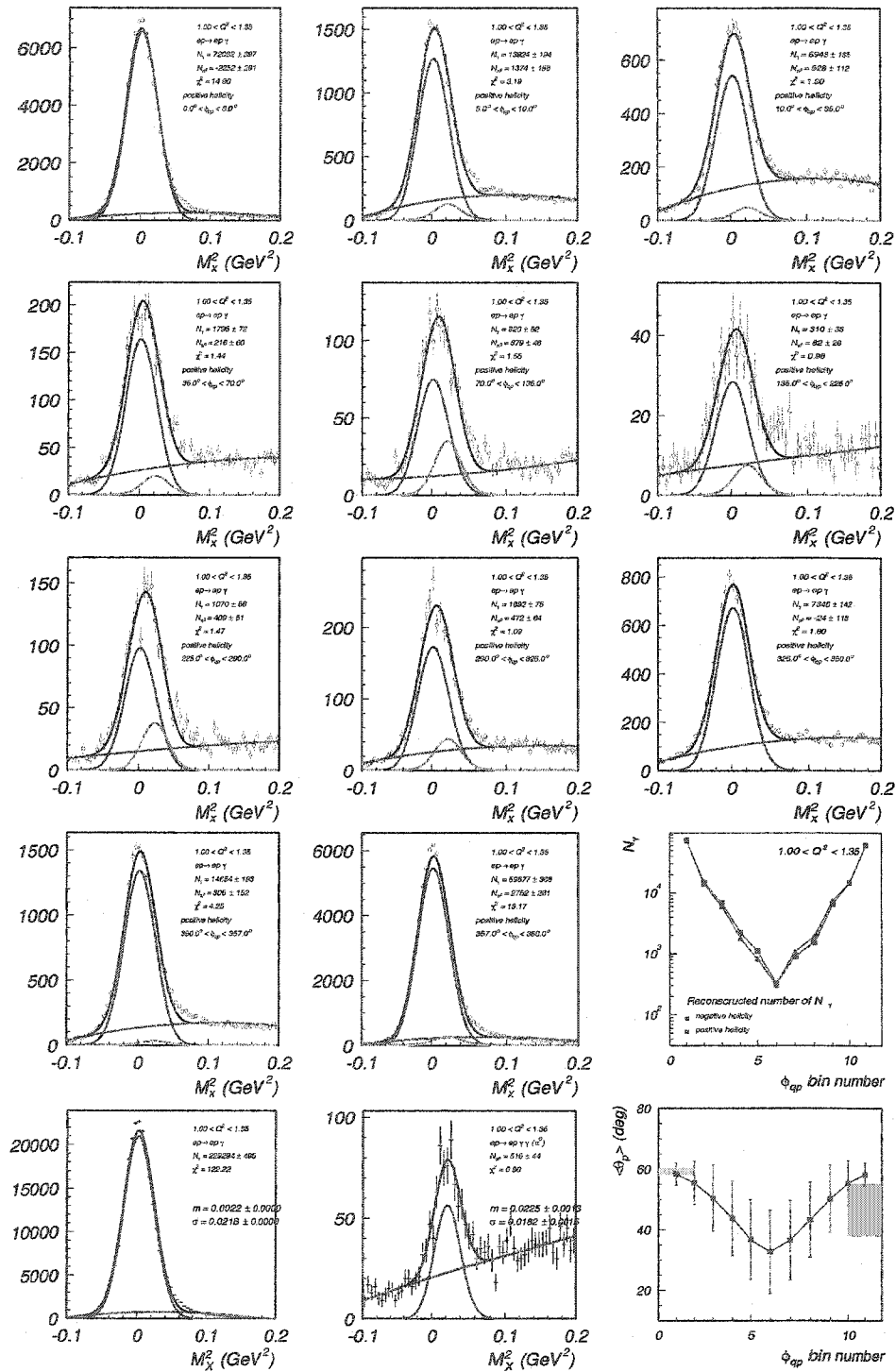


Figure 8-2: The fits to  $M_x^2$  for  $1.0 < Q^2 < 1.4$  (positive helicity).

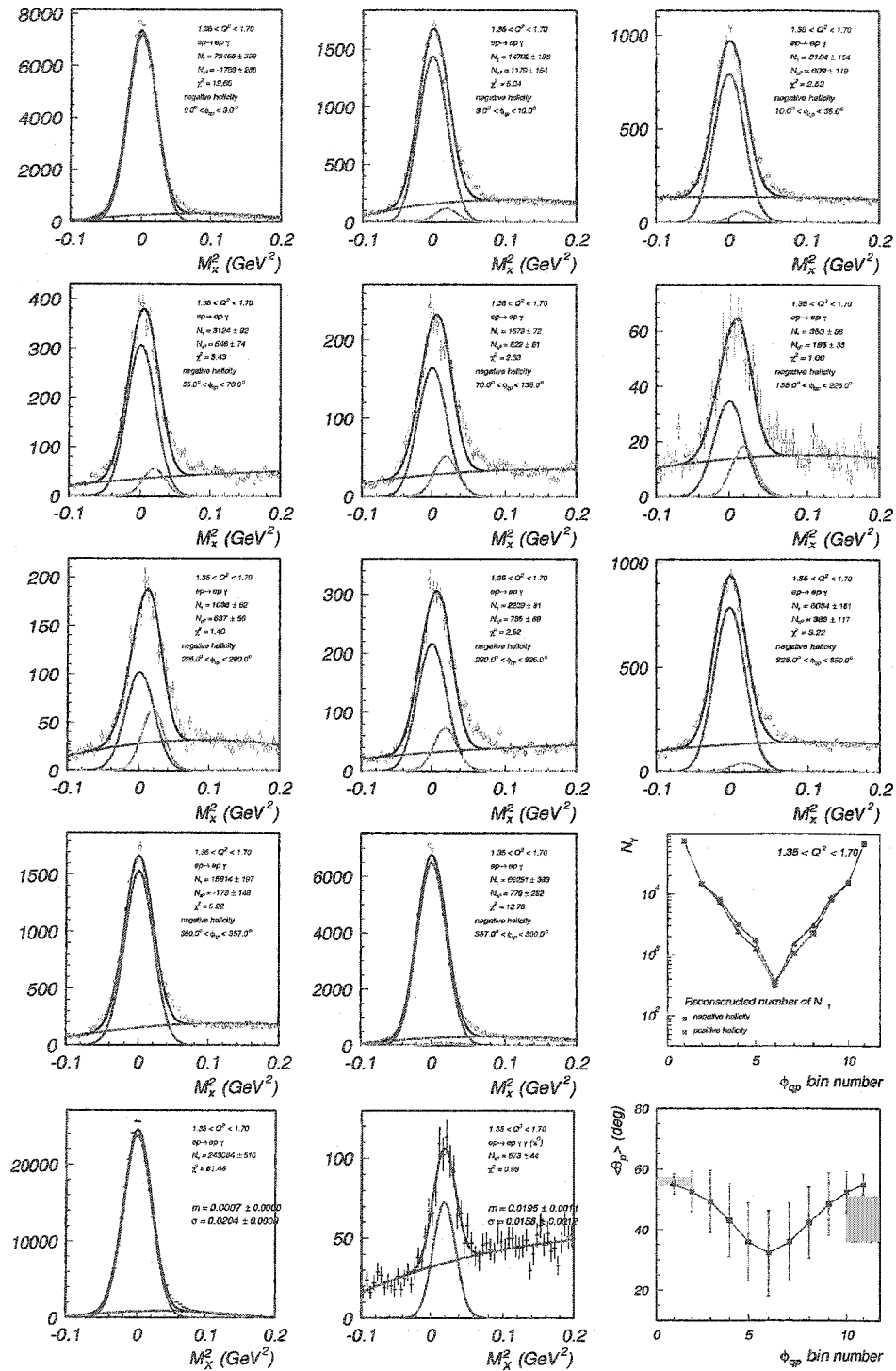


Figure 8-3: The fits to  $M_x^2$  for  $1.4 < Q^2 < 1.9$  (negative helicity).

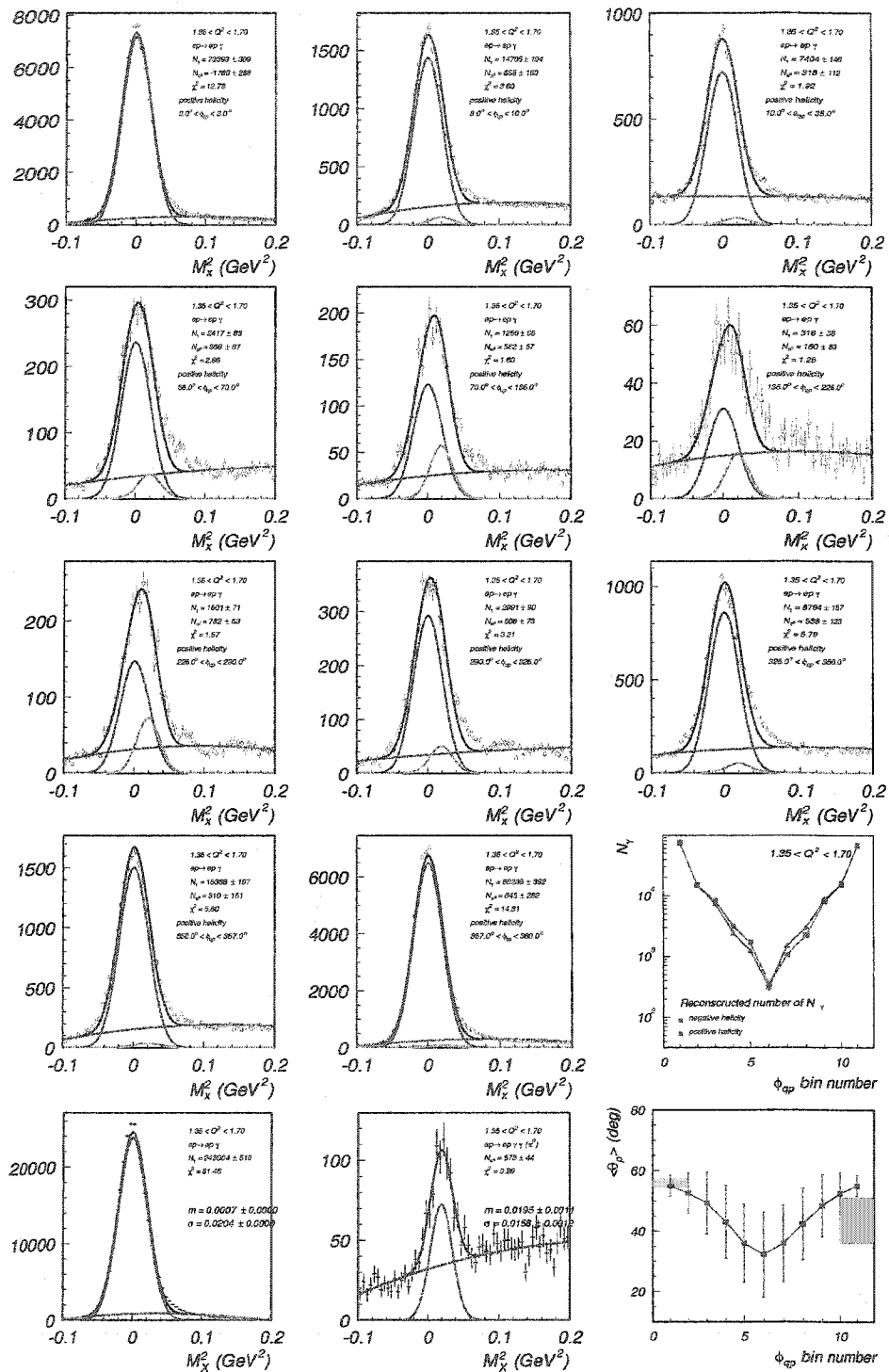


Figure 8-4: The fits to  $M_x^2$  for  $1.0 < Q^2 < 1.4$  (positive helicity).

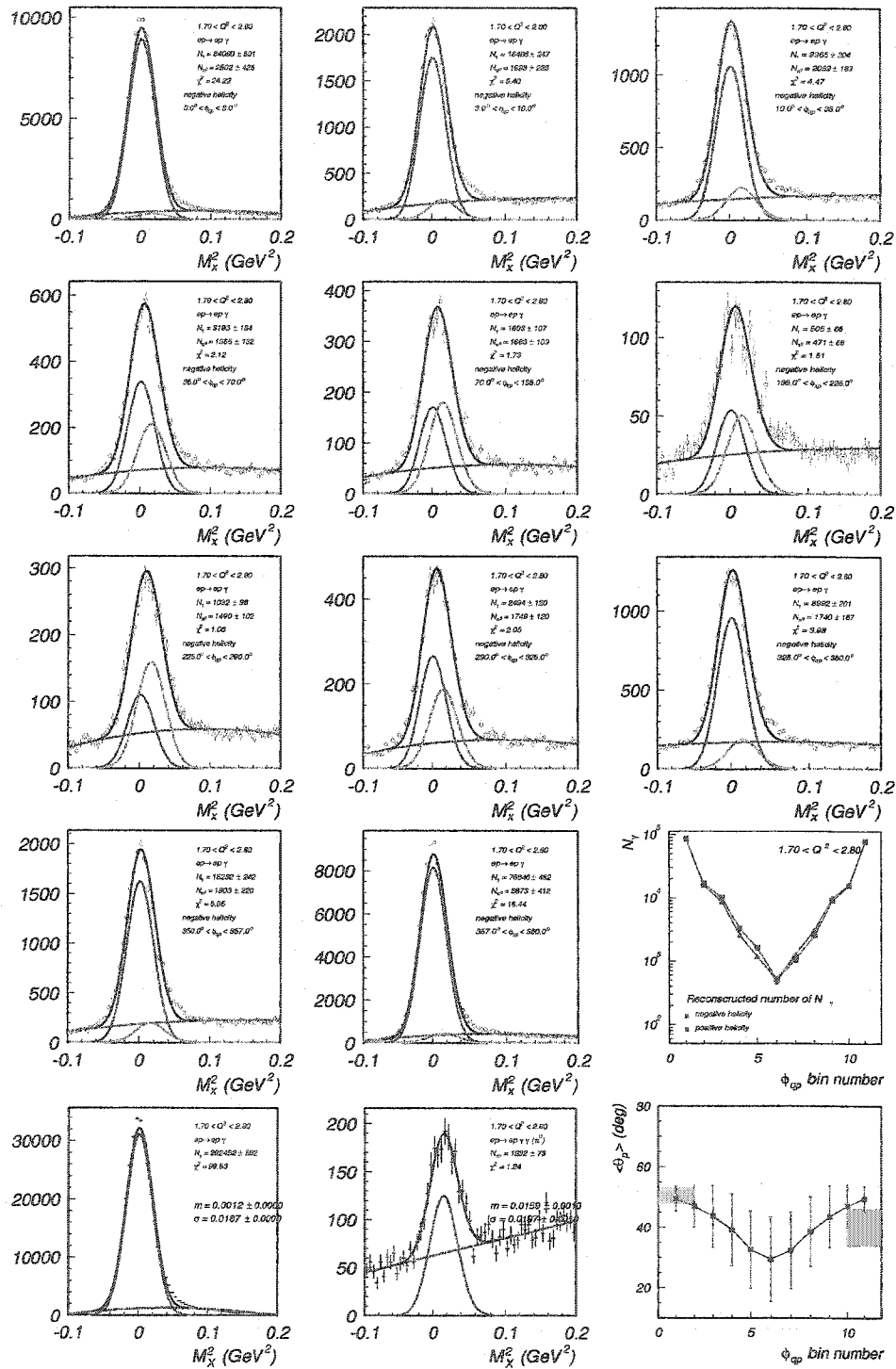


Figure 8-5: The fits to  $M_x^2$  for  $1.9 < Q^2 < 2.8$  (negative helicity).

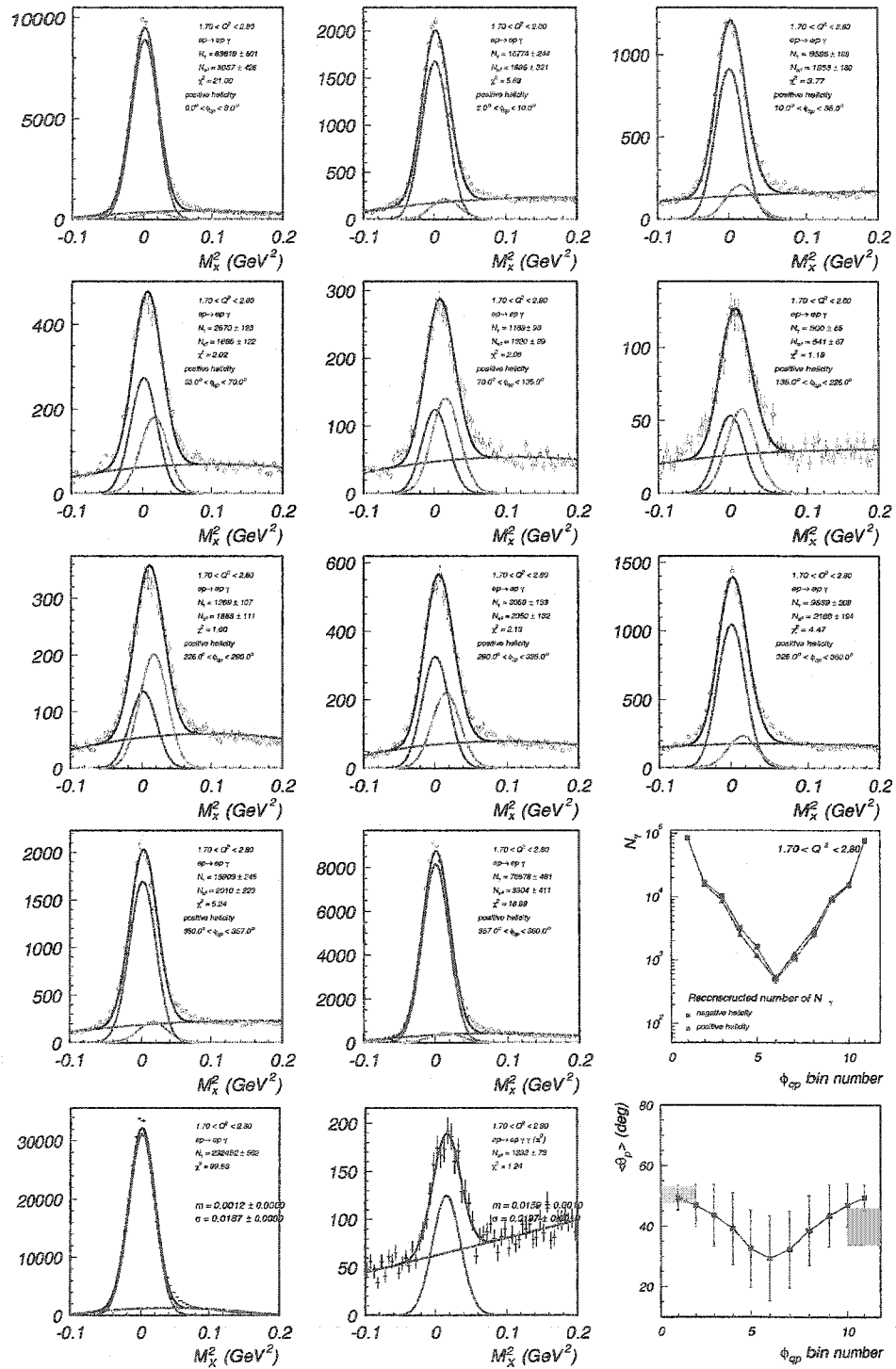


Figure 8-6: The fits to  $M_x^2$  for  $1.9 < Q^2 < 2.8$  (positive helicity).

### 8.2.3 Obtained asymmetries

The asymmetry calculated for each  $\phi_{qp}$  bin was fitted with function  $\alpha \sin(\phi) + \beta \sin(2\phi)$ . The result are shown for 3  $Q^2$  bins.

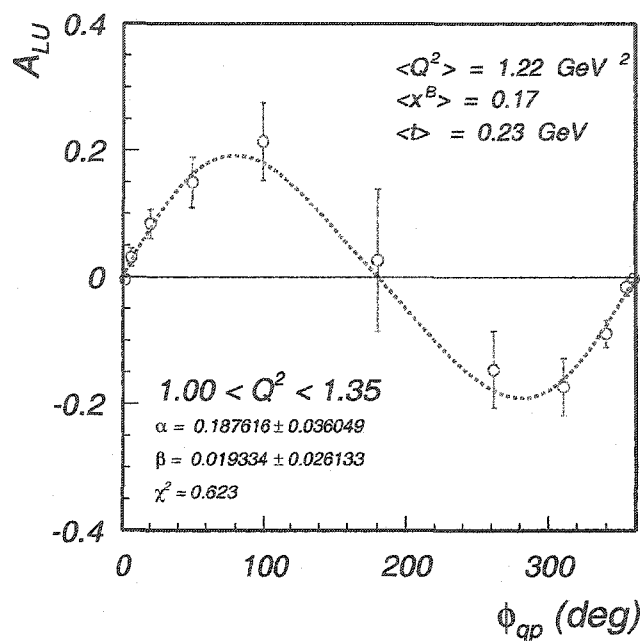


Figure 8-7: Fit to the azimuthal asymmetry for  $1.0 < Q^2 < 1.35$  GeV<sup>2</sup> for integrated  $0.1 < t < 0.4$  GeV.

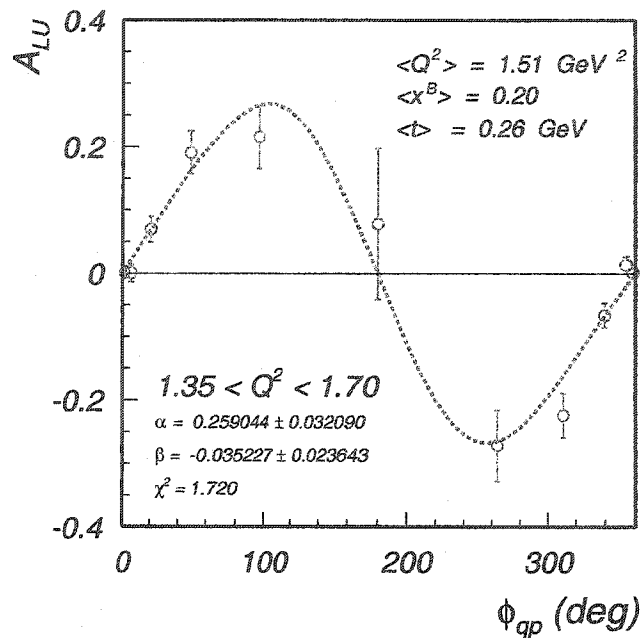


Figure 8-8: Fit to the azimuthal asymmetry for  $1.35 < Q^2 < 1.7 \text{ GeV}^2$  for integrated  $0.1 < t < 0.4 \text{ GeV}$ .

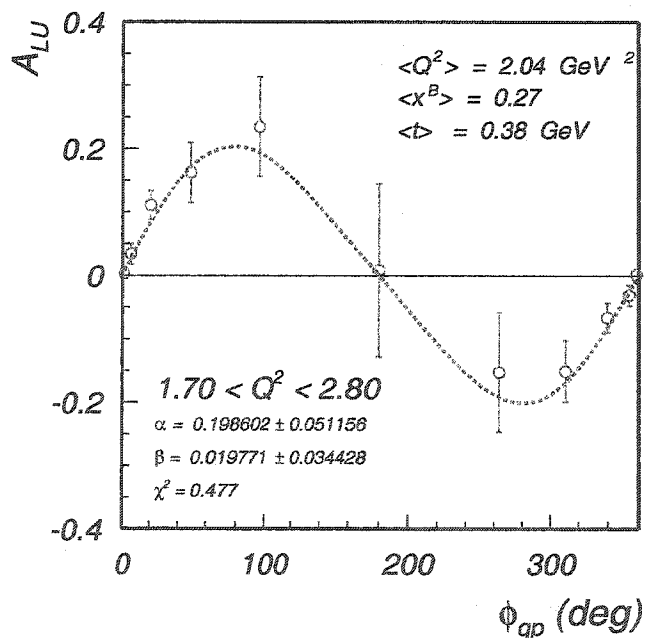


Figure 8-9: Fit to the azimuthal asymmetry for  $1.7 < Q^2 < 2.8 \text{ GeV}^2$  for integrated  $0.1 < t < 0.4 \text{ GeV}$ .

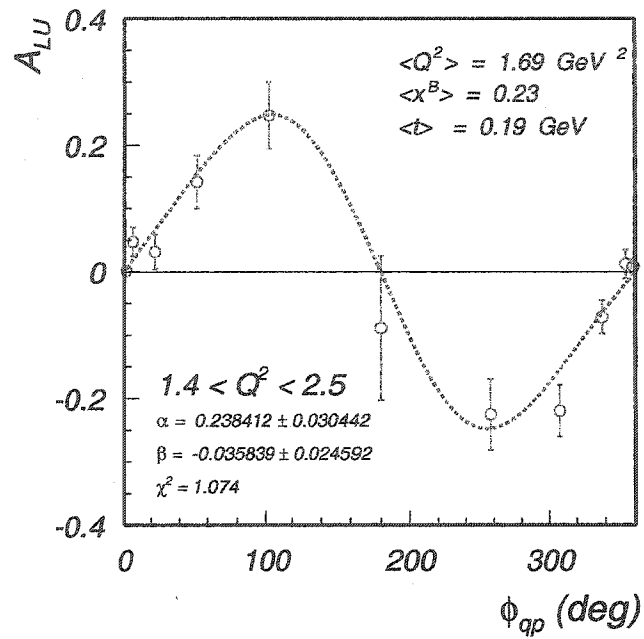


Figure 8-10: Fit to the azimuthal asymmetry for  $0.1 < -t < 0.25 \text{ GeV}$  for integrated  $1.4 < Q^2 < 2.5 \text{ GeV}^2$ .

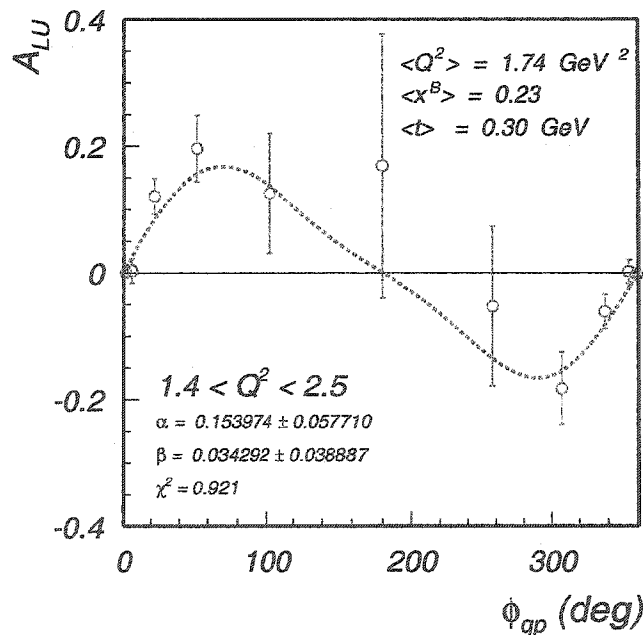


Figure 8-11: Fit to the azimuthal asymmetry for  $0.25 < -t < 0.35 \text{ GeV}$  for integrated  $1.4 < Q^2 < 2.5 \text{ GeV}^2$ .

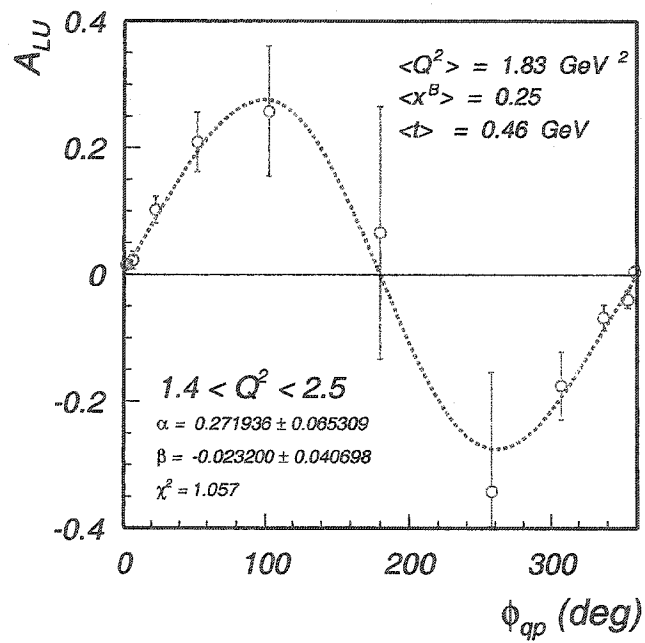


Figure 8-12: Fit to the azimuthal asymmetry for  $0.35 < -t < 0.6 \text{ GeV}$  for integrated  $1.4 < Q^2 < 2.5 \text{ GeV}^2$ .

# LIST OF REFERENCES

- [1] X. Ji. Gauge-invariant decomposition of nucleon spin. *Phys. Rev. Lett.* 78, 610, (1997).
- [2] A.V. Radushkin. *Phys. Lett B* 380, 417, (1997).
- [3] D. Muller et al. *Fortschr. Phys.* 42, 101, (1994).
- [4] N.F. Mott. *Proc. Roy. Soc. A* 135, (1932) 429.
- [5] M.N. Rosenbluth. *Phys. Rev.* 79, (1950) 615.
- [6] M. Yearian and R. Hofstadter. *Phys. Rev.* 110, (1958) 552.
- [7] *An introduction to Gauge Theories and The New Physics*. Cambridge University Press, (1982).
- [8] *Modern Elementary Particle Physics*. Addison-Wesley Publishing Company, (1987).
- [9] M.Diehl. Generalized parton distributions. *hep-ph/0307382*, (2003).
- [10] A.V. Radushkin. Double distributions and evolution equations. *Phys. Rev. D* 59, (1998) 014030.
- [11] M.Venderhaeghen K.Goeke, M.V. Polyakov. Hard exclusive reactions and the structure of hadrons. *Prog. Part Nucl. Phys.* 47, (2001).
- [12] V. Burkert. Study of generalized parton distributions with clas at jefferson lab. *hep-ph/0303006*, (2003).
- [13] M. Burkardt. *hep-ph/0207047*, (2002).
- [14] X. Ji A.V. Belitsky. Quark imaging in the proton via quantum phase-space distributions. *hep-ph/0307383*, (2003).
- [15] M.V. Polyakov and C. Weiss. Skewed and double distributions in the pion and the nucleon. *Phys. Rev. D* 60, (1999) 114017.
- [16] A.V. Belitsky et al. Theory of deeply virtual compton scattering on the nucleon. *hep-ph/0112108*, (2002).
- [17] A.V. Radushkin et al. Dvcs amplitude with kinematical twist-3 terms. *Phys. Lett B* 332, 340, (2000).

- [18] S.Stepanyan et al. (CLAS Coll.). *Phys. Rev. Lett.* 87, (2001).
- [19] A.Airapetian et al. (HERMES Coll.). *Phys. Rev. Lett.* 87, (2001).
- [20] A. Kirchner and D. Muller. Deeply virtual compton scattering off nuclei. *hep-ph/0302007*, (2003).
- [21] D. Muller and A. Belitsky. Overview of deeply virtual compton scattering. *hep-ph/0111037*, (2003).
- [22] M.D. Mestayer et al. The clas drift chamber system. *Nucl. Inst. and Meth.* A449, 81, (2000).
- [23] J.R. Comfort and B.C. Karp. *Phys. Rev. C* 21, 2162, (1980).
- [24] CLAS Collaboration. The cebaf large acceptance spectrometer (clas). *NIM.*, (2003).
- [25] G. Adams et al. The clas cherenkov detector. *Nucl. Inst. and Meth.* A465, 414, (2001).
- [26] E.S. Smith et al. The time-of-flight system for clas. *Nucl.Inst. and Meth.* A432, 265, (1999).
- [27] M. Amarian et al. The clas electromagnetic forward calorimeter. *Nucl. Inst. and Meth.* A460, 239, (2001).
- [28] Yuri Sharabian. Private Comuncations.
- [29] V. Gurjyan. Clas daq system. Private Comuncations.
- [30] Arne Freyberger. Clas reconstruction and analysis framework. [http : //www.jlab.org/ freyberg/recsis.html](http://www.jlab.org/freyberg/recsis.html).
- [31] V. Bobel and CLAS software group. The bos system for clas software. November 25 1995.
- [32] S. Stepanyan. Simple event builder (seb) in the framework of recsis. CLAS Internal Document, Private Comuncations.
- [33] Dan Protopopescu. PhD thesis, University of New Hampshire, (2002).
- [34] S. Tylor. PhD thesis, Rice University, 2000.
- [35] L.Elouadrhiri V.Burkert S.Stepanyan H.Egiyan. Charged particle identification in clas. *CLAS-NOTE 004, JLAB*, (1998).
- [36] E.S.Smith et al. Calibration of the clas tof system. *CLAS-NOTE 011, JLAB*, (1999).
- [37] Hovanes Egiyan. PhD thesis, College of William and Mary, 2001.
- [38] R. Niyazov. *DC Calibration*. PhD thesis, ODU, (2002).
- [39] Alexander V. Vlassov et al. Clas cerenkov detector calibrations. *CLAS-NOTE-005*, (1999).

- [40] G.Gavalian. Csql monitoring database. *CLAS-NOTE*, (2002).
- [41] S. Kuhn A. Klimenko. Momentum corrections for e6. *CLAS-NOTE 005*, (2003).
- [42] Rene Brun et al. Root data analysis framework. December 2003.
- [43] F. James. Minuit : Function minimization and error analysis. *CERN Program Library, D506*, (1994).
- [44] CLAS GSIM Simulation. [http://improv.unh.edu/maurik/gsim\\_info.shtml](http://improv.unh.edu/maurik/gsim_info.shtml).
- [45] H. Avakian. Dvcs event generator. Private Communications.

## VITA

Gagik Gavalian

Gagik Gavalian was born in Yerevan, Armenia on 30 January 1974. In June of 1991 graduated from #118 High School. In June 1996 received a Bachelor of Science degree in physics from Yerevan State University, Armenia. From 1996 to 1999 studied at the graduate school in Yerevan Physics Institute, then entered the physics graduate program at University of New Hampshire, where in January 2001 received a Master of Science degree. This dissertation was defended at the University of New Hampshire on 30 January 2004.